

**Clouds and the Earth's Radiant Energy System (CERES)**

**Algorithm Theoretical Basis Document**

*Cloud Optical Property Retrieval*

*(Subsystem 4.3)*

Patrick Minnis<sup>1</sup>  
David F. Young<sup>1</sup>  
David P. Kratz<sup>1</sup>  
James A. Coakley, Jr.<sup>3</sup>  
Michael D. King<sup>4</sup>  
Donald P. Garber<sup>2</sup>  
Patrick W. Heck<sup>2</sup>  
Shalini Mayor<sup>2</sup>  
Robert F. Arduini<sup>5</sup>

<sup>1</sup>Atmospheric Sciences Division, NASA Langley Research Center, Hampton, Virginia 23681-0001

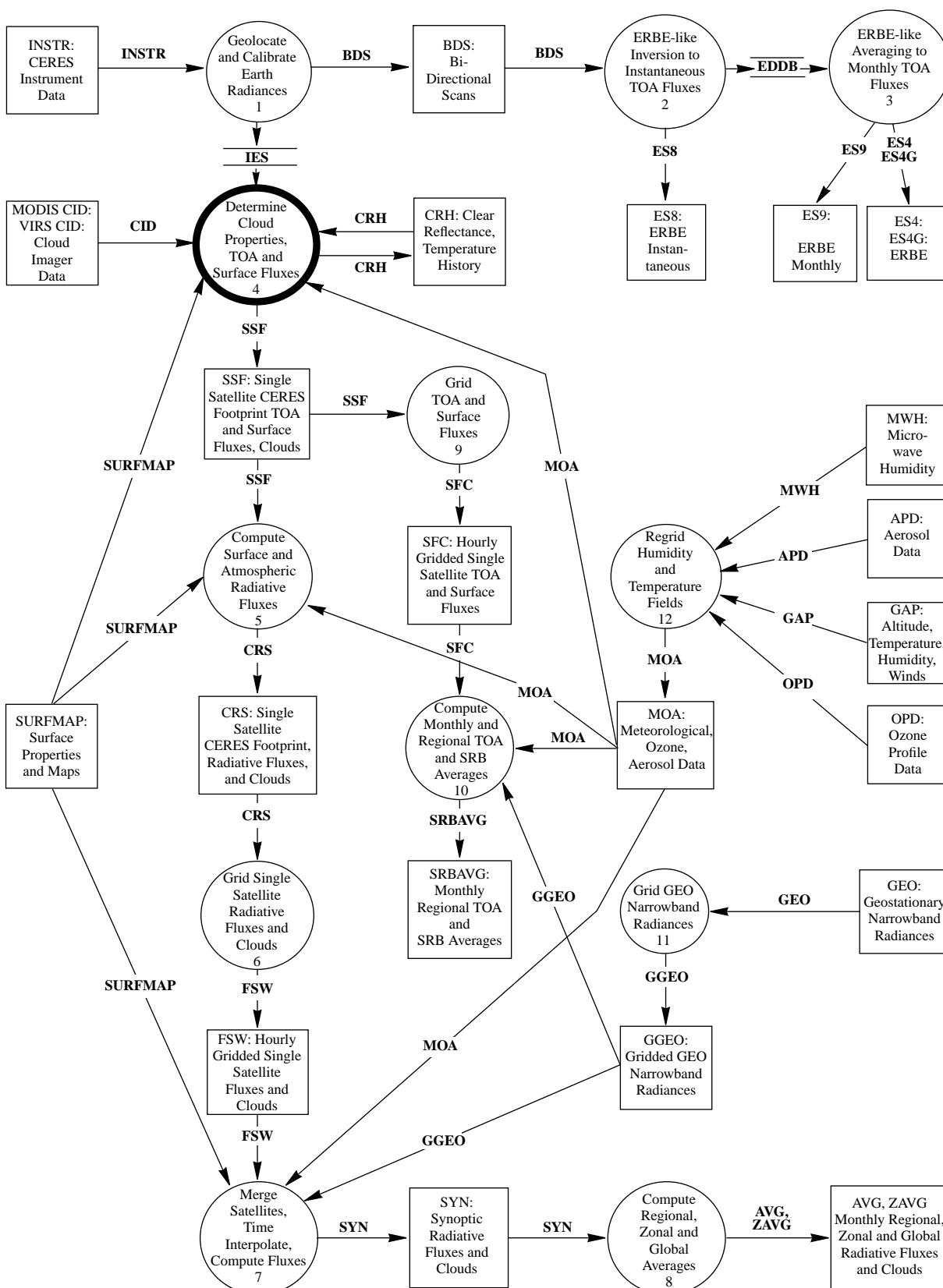
<sup>2</sup>Analytical Services & Materials, Inc., Hampton, Virginia 23666

<sup>3</sup>Oregon State University, Corvallis, Oregon 97331-2209

<sup>4</sup>Goddard Space Flight Center, Greenbelt, Maryland 20771

<sup>5</sup>Science Applications International Corporation (SAIC), Hampton, Virginia 23666

### CERES Top Level Data Flow Diagram



## Abstract

*Cloud physical and optical properties determine how clouds affect the radiance and flux fields at the surface, within the atmosphere, and at the top of the atmosphere. In this subsystem, CERES analyzes individual pixel radiances to derive the cloud properties that influence the radiation fields. For each pixel, state-of-the-art methods are used to ascertain the temperatures and pressures corresponding to the cloud top, base, and effective radiating center; the phase and effective size of the cloud particles; the cloud optical depth at a wavelength of 0.65  $\mu\text{m}$ ; the cloud emittance at 10.8  $\mu\text{m}$ ; and the cloud liquid or ice water path. During daytime, three different techniques will be used to account for deficiencies in any one of the individual methods. The first method uses 0.65-, 3.75-, and 10.8- $\mu\text{m}$  data from VIRS, AVHRR, or MODIS data. It iteratively solves for phase, particle size, optical depth, and effective cloud temperature. Emittance is computed from the optical depth. Cloud top and base temperatures and pressures are estimated using empirical formulae based on field experiment data. The water path is computed from the particle size. The second technique uses the similarity principle with a combination of 0.65-, 1.60-, and 2.12- $\mu\text{m}$  reflectance data to derive phase, particle size, and optical depth. Cloud temperature is determined by correcting the observed 10.8- $\mu\text{m}$  brightness temperature for semitransparency using the retrieved optical depth. The other parameters are computed in the same manner used for the first method. This approach will be partially implemented for VIRS and AVHRR and will be fully operational for MODIS. VIRS and AVHRR lack the 2.12- $\mu\text{m}$  channel that is available on MODIS. The third technique uses 3.75-, 10.8-, and 12.0- $\mu\text{m}$  data to determine cloud temperature, optical depth, phase, and particle size for optically thin clouds. This last daytime method will be used mainly for shadowed clouds and thin clouds over highly reflective backgrounds. It also forms the primary method for nighttime analyses. A second nighttime analysis is used for estimating an effective size and temperature for pixel clusters. Optical depth and cloud fraction are computed for individual pixels. All of the methods currently in development will become operational for application to CERES/TRMM. Results of this subsystem will be validated using coincident datasets from field programs. The required correlative data for validation include surface and aircraft measurements of the subsystem parameters using lidars, radars, in-situ microphysical probes, microwave radiometers, and sun photometers.*

### 4.3. Cloud Optical Property Retrieval

#### 4.3.1. Introduction

Cloud microphysics, phase and particle shape and size distribution determine the cloud optical depth and ice or liquid water path when integrated over the cloud thickness. These properties affect the emittance and bidirectional reflectance of the cloud. Cloud microphysics and macrophysics (areal extent, thickness, and altitude) determine the amount of radiation transmitted to the surface or to a lower

atmospheric layer and the amount of absorption within the cloud layer. Therefore, the conversion of the CERES radiances to flux, especially for the solar channel, depends on the cloud microphysics. Computation of the transmitted fluxes for the CERES estimation of atmospheric radiative divergence or surface heating also requires a quantification of the microphysical parameters.

From a climate perspective, it is important to know the global and climatological variability of cloud microphysical properties and to be able to relate them to radiative fluxes and cloud macrophysical properties. As an example, there is considerable interest in determining whether anthropogenic sources of cloud condensation nuclei significantly change the Earth's radiation balance by altering the microphysical characteristics of clouds (e.g., Twomey 1977; Charlson et al. 1987; Wigley 1989). Such issues and how they may affect future climates can only be addressed through modeling studies. In climate models, such as GCM's, water vapor is condensed or frozen in a given time step. This mass of water releases latent heat and alters the radiative flux fields. The cloud particle size distribution, phase, and shapes determine how the cloud affects the flow of radiation. The particle size distribution, which can be expressed in terms of an effective radius or diameter, primarily affects the scattering and absorption efficiencies of the cloud particles (van de Hulst 1957) and defines the cross section normal to the incident flux. Particle shape primarily affects the scattering phase function which ultimately determines how radiation is reflected from the cloud. Water phase governs the basic absorption properties and affects the scattering phase function through its relation to particle shape and through the index of refraction. To produce realistic clouds and radiation fields, a GCM must condense or freeze water in the proper locations and then must distribute the mass into the correct particle sizes and shapes. Some current GCM's employ parameterizations of radiation dependence on cloud particle size (e.g., Slingo 1989). The CERES measurements, the most complete simultaneous global observations of cloud microphysics and radiative fluxes yet proposed, will serve as an essential ground truth set to ensure that climate models accurately perform this critical function.

The CERES Cloud Optical Property Retrieval Subsystem (COPRS) will employ state-of-the-art methods to analyze the relevant spectral radiances available from the VIRS, MODIS, and AVHRR instruments operating during the CERES era. The primary goal of COPRS is to determine the phase, effective particle size, optical depth, liquid or ice water path, radiating temperature, pressure, and thickness of the cloud within a given CERES pixel. Although there are a wide variety of methods available, there is no single technique for deriving the COPRS products that applies in all cases. This subsystem uses state-of-the-art procedures to arrive at the most accurate values for each product. Thus, it will combine several algorithms to cover as many cases as possible. The composite algorithm described herein is a fluid entity subject to change as new research and/or limiting factors warrant.

#### 4.3.2. Background

There are numerous approaches to the satellite remote sensing of cloud phase, optical depth, and particle size. All of the methods are based on the assumption of radiative transfer in a plane-parallel cloud. These techniques exploit the spectral dependence of water and ice extinction, using wavelengths at which absorption by water vapor and other gases is minimal. The parameters used to characterize these variations include the wavelength  $\lambda$ , the spectral single-scattering albedo  $\tilde{\omega}_o = Q_s/Q_e$ , the asymmetry parameter  $g$ , the spectral optical depth  $\tau_\lambda$ , and the particle radius  $r$ . The extinction efficiency is  $Q_e = Q_s + Q_a$ . The scattering efficiency  $Q_s$  depends on the imaginary refractive index  $m_i$  and the size parameter  $x = 2\pi r/\lambda$ . For spherical particles and a given  $\lambda$ ,  $Q_s$  increases monotonically with  $x$  from zero to a maximum value near  $x = 6$ , then oscillates asymptotically to a smaller constant value. The oscillations are smoothed out when  $Q_s$  is integrated over a typical cloud droplet size distribution  $n(r)$ , in which  $r$  may vary from 2 to 100  $\mu\text{m}$ . The absorption efficiency  $Q_a$  and  $\tilde{\omega}_o$  follow a similar variation without the oscillations for values of  $m_i < 0.25$  (Hansen and Travis 1974). These values occur for  $\lambda < 12.5 \mu\text{m}$  (Hale and Query 1973). The variation with  $x$  becomes more monotonic for larger values of  $m_i$ . The asymptotic values of  $Q_e$  and  $\tilde{\omega}_o$  for large particles are 2.0 and 0.53, respectively. The single-scattering

albedo is essentially 1.0 and  $Q_s$  varies by less than 20% for typical cloud particle sizes at the nearly conservative-scattering wavelengths spanning the visible spectrum ( $\lambda < 1.0 \mu\text{m}$ ). For near-infrared wavelengths ( $\lambda \sim 3 \mu\text{m}$ ) ice and liquid water become moderately absorbing and  $x$  ranges from about 3 to 150. Thus, there are significant changes in both  $Q_e$  (~50%) and  $\tilde{\omega}_o$  (~26%) with changing particle size. At longer wavelengths, absorption is stronger, though still variable with particle size and wavelength.

The asymmetry parameter, which summarizes the scattering phase function, ranges from  $-1$  to  $1$ . Zero indicates isotropy,  $g = -1$  corresponds to backscattering, and  $g = 1$  denotes complete forward scattering. For any given particle shape,  $g$  generally increases with increasing particle size because of the narrowing diffraction peak. Smaller particles tend to scatter a greater portion of the incident radiation back into the source direction. The asymmetry parameter, which depends on both the real and imaginary refractive indices, varies nonmonotonically in a fashion similar to  $Q_s$ . There is a relative minimum in  $g$  for  $10 < x < 20$  and a relative maximum for  $4 < x < 10$ . Hansen and Travis (1974) may be consulted for additional details of the radiative properties of water droplets.

The spectral optical depth for a given size distribution over some distance is

$$\tau_\lambda = \pi Q_e \int_{z_1}^{z_2} N r_e^2 dz \quad (4.3-1)$$

where the effective radius is

$$r_e = \frac{\int_{r_1}^{r_2} r \pi r^2 n(r) dr}{\int_{r_1}^{r_2} \pi r^2 n(r) dr} \quad (4.3-2a)$$

$n(r)$  is the number density of droplets with radius  $r$ , and  $N$  is the total particle number density. To distinguish between water and ice clouds,  $r_e$  will be used for water clouds and the equivalent diameter

$$D_e = \frac{\int_{L_1}^{L_2} D(L) \pi A_e(L) n(L) dL}{\int_{L_1}^{L_2} \pi A_e(L) n(L) dL} \quad (4.3-2b)$$

will be used for ice clouds. The variable  $D(L)$  is the volume equivalent diameter of the hexagonal ice crystal of length  $L$  and width  $d$ . It is assumed that there is a monotonic relationship between  $L$  and  $d$  for the hexagonal ice columns defined by Takano and Liou (1989). This yields a unique relationship between the cross-sectional area  $A_e$  of these randomly oriented columns (Takano and Liou 1989) and  $L$ . The parameters,  $\tau_\lambda$ ,  $r_e$  or  $D_e$ ,  $\tilde{\omega}_o$ , and  $g$  affect the radiation absorbed, reflected, transmitted, and emitted by a given cloud. The dependence of the radiation field on these variables can be simulated using radiative transfer calculations. Cloud effective particle size, optical depth, phase, and cloud temperature can be determined from satellite-measured multispectral radiances by matching the radiances to the computed radiative transfer results.

The basic techniques for determining cloud phase, optical depth, and effective particle size can be divided into two groups that overlap: reflection and emission techniques. The former applies during daytime and only employs solar wavelengths. Emission techniques generally are applicable during any time of day because they rely primarily on radiation emitted at infrared and near-infrared wavelengths.

#### 4.3.2.1. Solar Reflectance Methods

The spectral bidirectional reflectance or, simply, reflectance is

$$\rho_{\lambda}(\tau_{\lambda}; \mu_o, \mu, \phi) = \frac{I_{\lambda}(\mu_o, \mu, \phi)}{\mu_o \pi E_{o\lambda}} \quad (4.3-3)$$

where  $E_{o\lambda}$  is the spectral solar irradiance and  $\mu_o$ ,  $\mu$ , and  $\phi$  are the solar zenith and viewing zenith angle cosines and the relative azimuth angles, respectively. Optical depth can be determined directly from the reflectance data in the absence of particle size information, if a particle size is specified. Rossow et al. (1985) assumed that all clouds can be interpreted as having  $r_e = 10 \mu\text{m}$ , an approach later used in the ISCCP analyses (Rossow et al. 1992) and in pre-ISCCP analyses of NOAA-5 SR data (Rossow and Lacis 1990). In those analyses, a value of  $\tau_{0.65}$  is determined by matching the 0.65- $\mu\text{m}$  (visible) reflectance to a set of model-generated reflectance tables developed for different cloud heights, surface albedos, and optical depths. Later analyses using FIRE data (Baum et al. 1992; Minnis et al. 1993a) indicated that significant improvement is obtained in the accuracy of the derived optical depths by using the hexagonal ice crystal phase functions of Takano and Liou (1989) for cirrus clouds. Minnis et al. (1993b) developed a parameterization that incorporated surface albedo and cloud height so that reflectance tables were only needed to account for optical depth. The gained computer storage space could be used to accommodate models with variable particle size.

A more accurate estimate of  $\tau_{\lambda}$  can be made if the particle size, shape, and phase are known. One of the earliest applications of a reflection method for this purpose was performed by Hansen and Pollack (1970) who attempted to explain the spectral variation in aircraft reflectivity measurements (Blau et al. 1966) in terms of phase and particle size using theoretical computations. Twomey and Seton (1980) showed theoretically that mean radius and optical depth could be determined for optically thick clouds using the scaled optical depth  $\tau_{\lambda}' = (1 - \tilde{\omega}_o' g) \tau_{\lambda}$  and the scaled single-scatter albedo  $\tilde{\omega}_o' = \tilde{\omega}_o (1 - g) / (1 - \tilde{\omega}_o g)$ . A measurement of reflectance at a conservative-scattering wavelength could be used to determine  $\tau_{\lambda}'$ , while  $r_e$  could be estimated using simultaneous measurements of reflectance at  $\lambda = 1.6$  or  $2.2 \mu\text{m}$ . Later comparisons of aircraft reflectance measurements and calculations at  $\lambda = 0.75, 1.0, 1.2,$  and  $2.25 \mu\text{m}$  were relatively unsuccessful in matching the data with theory at all four wavelengths simultaneously (Twomey and Cocks 1982). Twomey and Cocks (1989) utilized an improved instrument and a multispectral minimum difference method to match theory and measurements much more closely for the same wavelengths plus  $\lambda = 1.66 \mu\text{m}$ .

Coakley et al. (1987) and Radke et al. (1989) showed that reflectance measurements at  $3.7 \mu\text{m}$  could be used to detect ship tracks in marine stratus clouds because the droplet radii decreased in the portion of the cloud affected by the ship's exhaust. They also showed that an increase in the reflectance ratio,  $\rho_{0.74}/\rho_{2.2}$ , accompanied the decrease in radius measured with in-situ probes. Using theoretical calculations at  $0.75, 1.65, 2.16,$  and  $3.70 \mu\text{m}$  and a minimum difference method employing the scaled optical depth  $\tau' = (1 - g)\tau$  and the similarity parameter  $s = [(1 - \tilde{\omega}_o)/(1 - \tilde{\omega}_o g)]^{1/2}$ , Nakajima and King (1990) showed that measurements of reflectance at  $0.75 \mu\text{m}$  and at either of the other wavelengths could be used to solve for  $r_e$  and  $\tau_{\lambda}$ . However, a third channel was found to be desirable for removing ambiguities arising from the nonmonotonic variation of  $\tilde{\omega}_o$  with  $r_e$ . They also found that the retrieved value of  $r_e$  corresponds to the effective radius for some upper portion of the cloud that depends on the cloud thickness. Thus,  $r_e$  requires some adjustment to estimate the effective radius for the entire cloud. Later analyses of aircraft observations at  $0.75, 1.65,$  and  $2.16 \mu\text{m}$  (Nakajima et al. 1991) over stratocumulus clouds produced excellent correlation between the remotely sensed, center-adjusted effective radii and the in-situ particle sizes (Fig. 4.3-1). Although the remote sensing analysis apparently overestimated  $r_e$ , the results clearly demonstrated the potential of this method. Further examination of the results indicated that the water vapor absorption at  $1.65$  and  $2.16 \mu\text{m}$  needed additional study and that there are some significant disagreements between the aircraft probes used to measure particle sizes in the clouds. Wielicki et al. (1990) estimated particle sizes for water and ice clouds from Landsat observations at

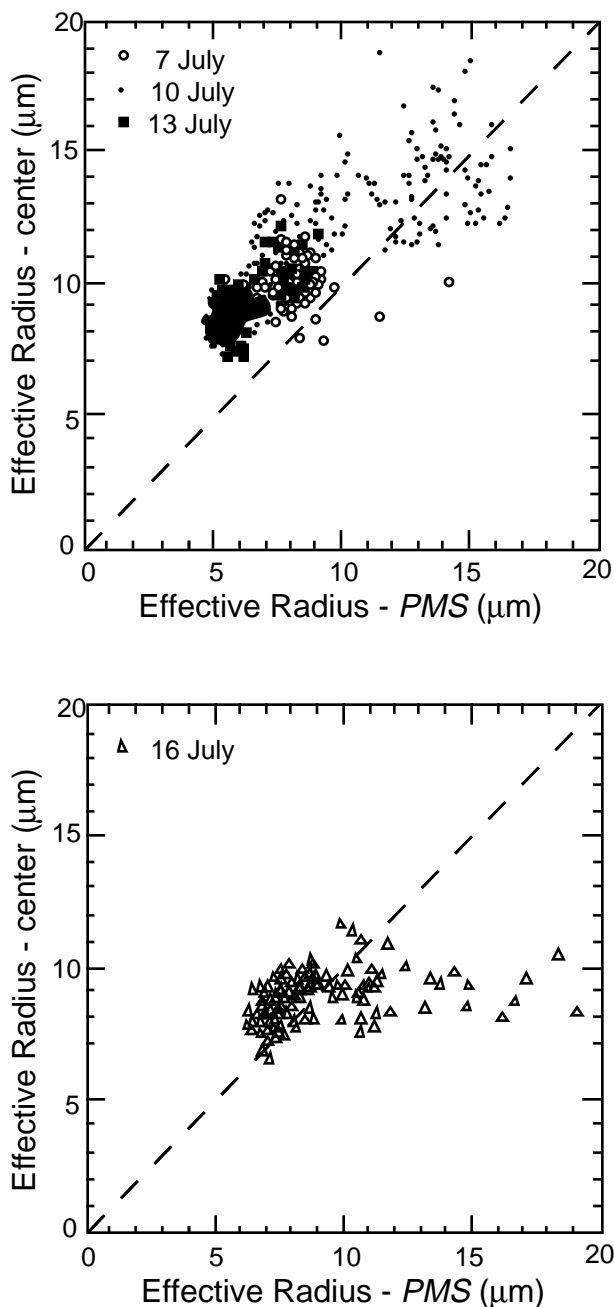


Figure 4.3-1. Effective radius derived from remote sensing and adjusted to center of cloud compared with values obtained from in-situ measurements obtained using all three PMS probes. The top panel is based on ER-2 MCR measurements, while the bottom panel is from Landsat-5 TM data. All measurements were taken during 1987 off the coast of California during the FIRE Marine Stratocumulus Intensive Observing Period (adapted from Nakajima et al. 1991).

$\lambda = 0.83, 1.65, \text{ and } 2.21 \mu\text{m}$  by matching ratios of the reflectances to theoretical calculations. For water clouds, they found good agreement between the values of  $r_e$  derived from in-situ data and the  $0.83\text{-}\mu\text{m}/2.21\text{-}\mu\text{m}$  reflectance ratios. Rawlins and Foot (1990) used reflectances from aircraft measurements at  $\lambda = 1.04, 1.24, 1.55, \text{ and } 2.01 \mu\text{m}$  to derive values of  $r_e$  that were 20% to 50% greater than their in-situ counterparts. Differences between the in-situ and remotely sensed data have not yet been entirely resolved as there are uncertainties in the instrumental results related to detection capabilities and in the remotely sensed data because of the effects of the vertical variation of  $r_e$  within the cloud.

Cloud phase can be determined by comparing the ratios of reflectances at two wavelengths: one that is a conservative scatterer for both ice and water and one that has strong absorption for ice and weak absorption for water. This type of approach was suggested by the theoretical calculations of Hansen and Pollack (1970) and other researchers. Curran and Wu (1982) used this approach to determine the presence of supercooled water clouds from Skylab measurements of reflectance at 1.61  $\mu\text{m}$ . Masuda and Takashima (1990) demonstrated theoretically that a combination of measurements at 0.63 or 0.86 and 1.61  $\mu\text{m}$  would be best for determining phase. Wielicki et al. (1990) found that the 2.21- $\mu\text{m}$ /0.83- $\mu\text{m}$  and the 1.65- $\mu\text{m}$ /0.83- $\mu\text{m}$  Landsat reflectance ratios could effectively distinguish between ice and water clouds when used together. King et al. (1992) showed that distinctly different 1.63- $\mu\text{m}$ /0.75- $\mu\text{m}$  reflectance ratios are measured over water and ice clouds. The water cloud reflectance ratio is about half that of the ice cloud. The ratio techniques are continually being improved and developed. They will be useful for the TRMM/VIRS and MODIS instruments but not for AVHRR.

#### 4.3.2.2. Thermal Infrared Emittance Techniques

The simple model of brightness temperature usually employed in satellite remote sensing of clouds is that the observed radiance is

$$B_{\lambda}(T_{\lambda}) = [1 - \varepsilon_{\lambda}(\mu, \tau_{\lambda})][(1 - \varepsilon_{s\lambda})B_{\lambda}(T_{D_s}) + \varepsilon_{s\lambda}B_{\lambda}(T_s)] + \varepsilon_{\lambda}(\mu, \tau_{\lambda})B_{\lambda}(T_{cld}) \quad (4.3-4)$$

where  $T_{\lambda}$  is the equivalent blackbody temperature,  $T_s$  is the surface temperature,  $T_{cld}$  is the cloud temperature,  $T_{D_s}$  is the equivalent blackbody temperature of the downwelling radiance at the surface,  $B$  is the Planck function,  $\varepsilon_{s\lambda}$  is the surface emittance, and the effective cloud emittance  $\varepsilon_{\lambda}$  approaches unity as the cloud becomes optically thick. If scattering is neglected,

$$\varepsilon_{\lambda} = 1 - \exp(-\tau_{a\lambda}/\mu) \quad (4.3-5)$$

where the absorption optical depth  $\tau_{a\lambda} = (1 - \tilde{\omega}_o)\tau_{\lambda}$ . The quantity  $\varepsilon_{s\lambda}B_{\lambda}(T_s)$  can be replaced in many instances with  $B_{\lambda}(T_{cs\lambda})$ , where  $T_{cs\lambda}$  is the clear-sky temperature. It includes the attenuation of the atmosphere which is not explicitly included in (4.3-4). For semitransparent clouds, it is possible to estimate  $\varepsilon_{\lambda}$  and  $T_{cld}$  from simultaneous measurements at two different wavelengths  $\lambda_1$  and  $\lambda_2$ , if  $T_{cs\lambda}$  and the relationship between  $\varepsilon_{\lambda_1}$  and  $\varepsilon_{\lambda_2}$  is known and  $\varepsilon_{\lambda_1} \neq \varepsilon_{\lambda_2}$ . The surface emittance is generally assumed to be unity for longer wavelengths. It may be as low as 0.9 for some surfaces at the near-infrared wavelengths. If  $\varepsilon_{\lambda}$  is known, then  $\tau_{\lambda}$  can be determined from either (4.3-5) or some other function that relates the two quantities. If  $T_{cld}$  is known—from some other source or a third wavelength—it is theoretically possible to determine  $r_e$  and  $\tau_{\lambda}$ . As in the case for reflectance methods, the optical properties of clouds need to be different at each of the involved wavelengths. Hunt (1973) showed that the cloud emittance at 3.7  $\mu\text{m}$  is more sensitive to changes in optical depth and particle size than at longer wavelengths such as 11 or 12  $\mu\text{m}$ . Liou (1974) demonstrated that the optical properties of cirrus varied between 11 and 12  $\mu\text{m}$ . These three spectral channels have been used on meteorological satellites and, therefore, have received much of the attention for deriving cloud properties. Some techniques make use of the brightness temperature difference  $BTD_{i-j}$  between  $T_i$  and  $T_j$  to provide some information about the particle size and optical depth. The subscripts  $i$  and  $j$  can refer to sensor channel numbers or their nominal wavelengths. The AVHRR channels 3, 4, and 5 have nominal wavelengths of 3.75, 10.8, and 12.0  $\mu\text{m}$ .

Inoue (1985) developed a method using  $BTD_{4-5}$  and an implicit mean particle size to determine  $\varepsilon_4$  and, therefore,  $\tau_4$  from AVHRR channels 4 and 5 taken over semitransparent cirrus clouds. Wu (1987) developed an algorithm to derive cirrus effective cloud fraction  $\varepsilon_{11}C$  and  $T_{cld}$  using the HIRS2 3.7-, 4.0-, and 11- $\mu\text{m}$  data. d'Entremont (1986) exploited the variation of AVHRR  $BTD_{3-4}$  with particle size to determine the presence of low clouds and fog at night. Ackerman and Stephens (1987) further explained the phenomena that permit the estimation of particle size from measurements of radiation simultaneously at two wavelengths: one strongly absorbing and one weakly absorbing. Prabhakara et al. (1988) used  $BTD_{10.8-12.6}$  from the 10.8- and 12.6- $\mu\text{m}$  IRIS data taken by the Nimbus-4 satellite as

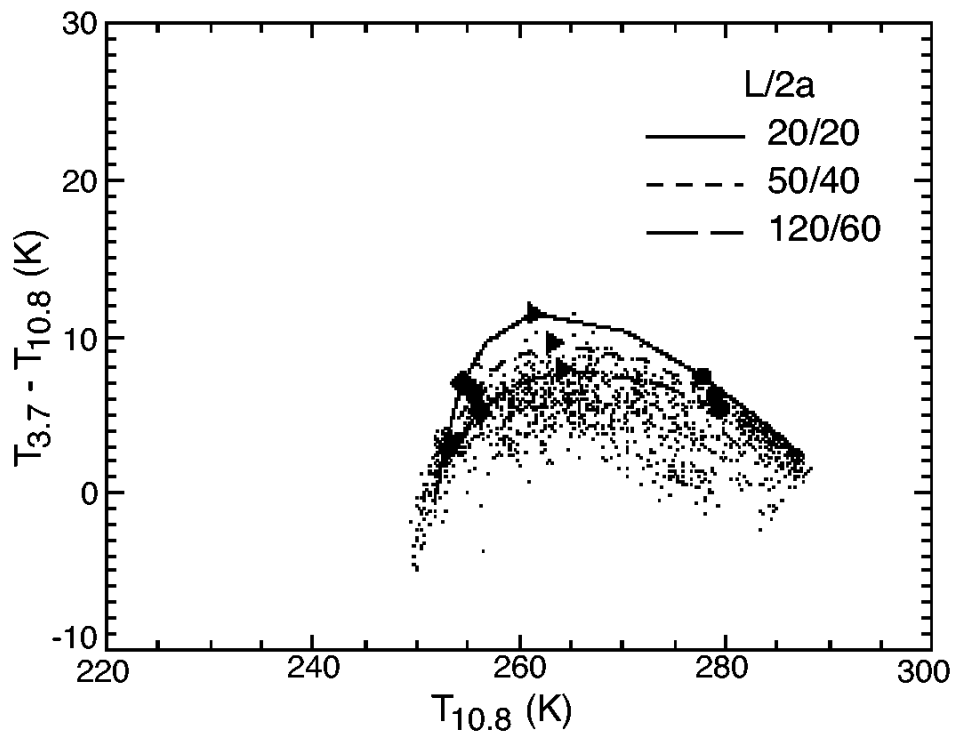
indices for the distribution of optically thin cirrus clouds. Ackerman et al. (1990) used ratios of the mass absorption coefficients derived from 10.1- and 12.0- $\mu\text{m}$  HIS measurements to estimate cirrus cloud particle sizes in terms of ice-sphere effective radius. Liou et al. (1990a) used an iterative technique to estimate cloud temperature and optical depth from 6.5- and 11- $\mu\text{m}$  radiances taken over high-altitude cirrus clouds. From theoretical calculations using spheres and cylinders to represent cirrus particles, Parol et al. (1991) concluded that the AVHRR  $BTD_{4-5}$  depends significantly on particle shape but not so much on phase. They found that scattering should be taken into account in the interpretation of the  $BTD$ 's. Takano et al. (1992) developed a parameterization to compute the optical properties of cirrus clouds at any infrared wavelength using a combination of hexagonal ice crystals and spheroids to represent the cirrus cloud particles. The latter are used for large size parameters  $x$ , while the former are invoked for small  $x$ . The Takano et al. (1992) model matched observations of  $BTD_{11-12}$  much more closely than the spherical representations. Lin and Coakley (1993) advanced a method to derive a particle size index for single-layer cloud decks using radiative transfer model fits to clusters of collocated AVHRR channel 4 and 5 pixels. Their method simultaneously solved for the emittance and cloud fraction by computing an envelope of solutions based on a single effective radius and cloud temperature for the pixel cluster. Ou et al. (1993) developed a method to derive  $\tau_{0.67}$ ,  $T_{cld}$ , and  $D_e$  from nighttime AVHRR measurements of  $T_{3.7}$  and  $T_{10.9}$ . They assumed that particle size depended on cloud temperature according to the parameterization of Heymsfield and Platt (1984) and developed a parameterization of  $B_{11}(T)$  in terms of  $B_{3.7}(T)$ . Baum et al. (1994) successfully modeled  $BTD_{3.7-11}$  and  $BTD_{11-12}$  values from AVHRR observations taken over oceanic cirrus, stratocumulus, and a cirrus-stratocumulus mix. Their models are based on the results of Takano et al. (1992), Liou et al. (1990b), Minnis et al. (1993b), and Mie scattering calculations. They found that a combination of all three channels may be used to determine  $T_{cld}$ ,  $\tau_\lambda$ , and  $r_e$  or  $D_e$  simultaneously.

Infrared spectra may be used to determine cloud phase, though not as easily as solar spectra. Ackerman et al. (1990) demonstrated that  $BTD_{11-12}$  and  $BTD_{8-11}$  may be used to determine the cloud phase for optically thin clouds, at least. The analyses of Baum et al. (1994) showed that a combination of  $BTD_{3.7-11}$  and  $BTD_{11-12}$  has the potential for separating ice and water clouds for many particle sizes for  $\tau_{0.65} < 6$ . Figures 4.3-2 and 4.3-3 adapted from Baum et al. (1994) show the  $BTD$ 's from AVHRR observations for a cloud deck with  $T_{cld} = 250$  K. The theoretical values of  $BTD_{3.7-11}$  for ice clouds, shown as the curves in Figure 4.3-2(a), are generally less than those for water clouds (Fig. 4.3-3(a)) while the opposite is true for  $BTD_{11-12}$  (Figs. 4.3-2(b) and 4.3-3(b)). This potential for phase determination is currently under study.

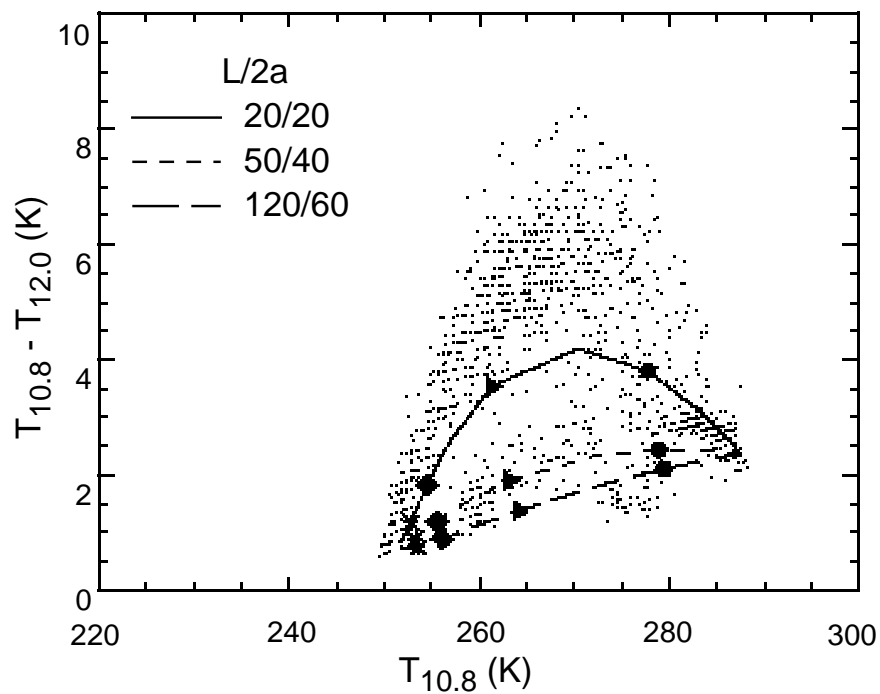
#### 4.3.2.3. Combined Thermal Emittance-Solar Reflectance Methods

There are mixed methods that use both thermal and solar channels and, sometimes, an overlapped solar-thermal channel. The simplest of the mixed techniques, a bispectral visible-infrared analysis, is the form most widely used. In this approach, optical depth is derived from the visible reflectances using an implicit or explicit model of the cloud radiative properties. The infrared (11  $\mu\text{m}$ ) emittance, derived from the visible optical depth, is used to correct the observed  $T_{11}$  using (4.3-4) to obtain  $T_{cld}$ . Reynolds and Vonder Haar (1977) used an empirical model that represents an implicit cloud model to relate cloud albedo to  $\epsilon_{11}$ . Rossow and Lacis (1990) used a theoretical-empirical approach and a single cloud microphysical model, a method also used by the ISCCP (Rossow et al. 1992). Minnis et al. (1993b) employed a purely theoretical method using various cloud microphysical models. Those bispectral methods are relatively effective and applicable to most operational satellite datasets. They do not, however, yield any information about particle size or phase other than what is assumed. To obtain particle size, a third channel or some other type of information is needed.

Arking and Childs (1985) pioneered the use of visible, infrared, and the 3.7- $\mu\text{m}$  data to retrieve cloud fraction  $C$ ,  $\tau_{0.65}$ ,  $r_e$ , and  $T_{cld}$  for each pixel. Their method uses a pixel clustering technique to determine  $T_{cld}$  for a scene. All pixels outside the cluster are assumed to have a cloud temperature equal



(a)  $BTD_{3.7-11}$ .



(b)  $BTD_{11-12}$ .

Figure 4.3-2. Comparison of theoretical results assuming cloud composed entirely of hexagonal ice crystals with AVHRR data taken over the northwest Atlantic at 0606 UTC, April 16, 1989. The ice crystal length-to-width ratios  $L/2a$  are given in  $\mu\text{m}/\mu\text{m}$ . The circles, triangles, diamonds, and asterisks refer to the 10.8- $\mu\text{m}$  optical depths of 0.5, 2, 4, and 6, respectively (adapted from Baum et al. 1994).

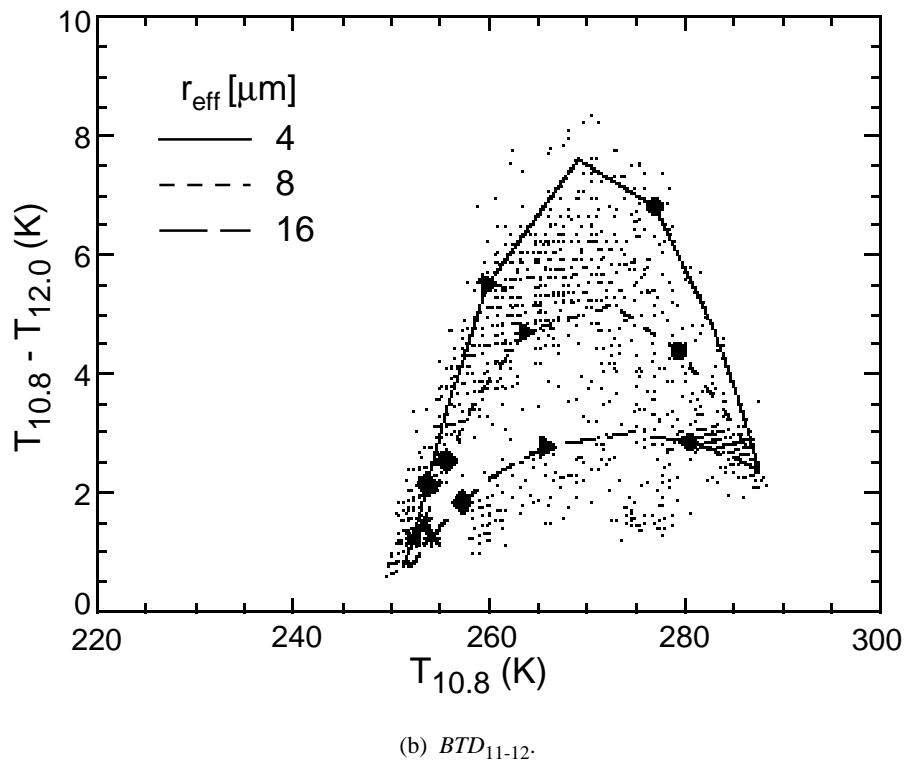
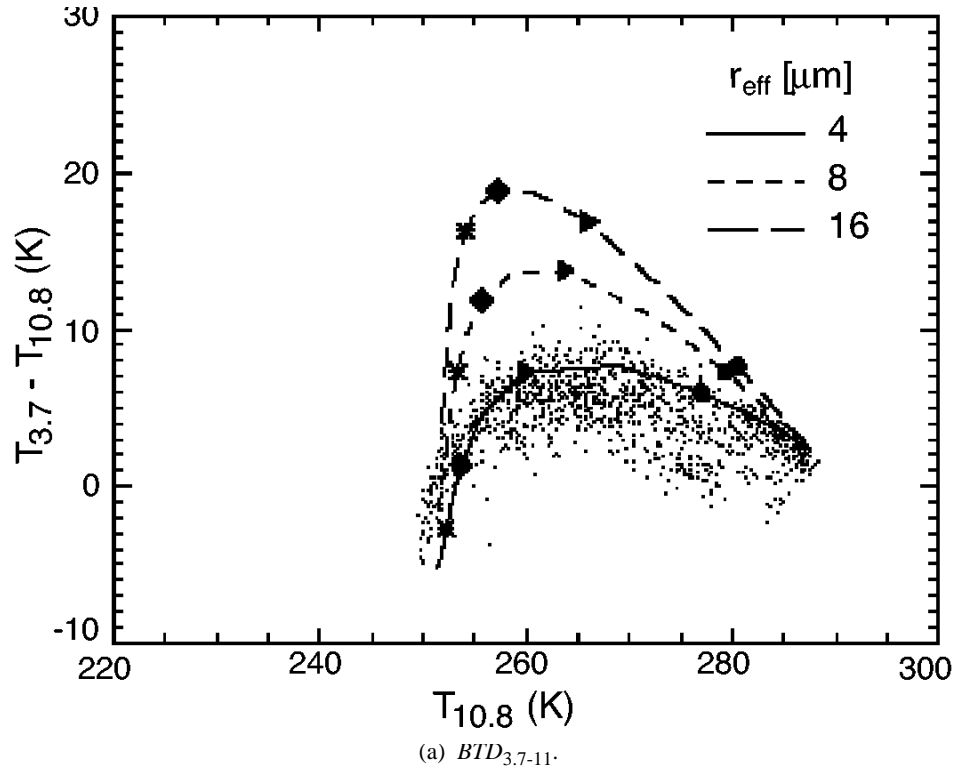


Figure 4.3-3. Same as Figure 4.3-2, except assuming cloud composed entirely of supercooled water droplets in the model calculations (adapted from Baum et al. 1994).

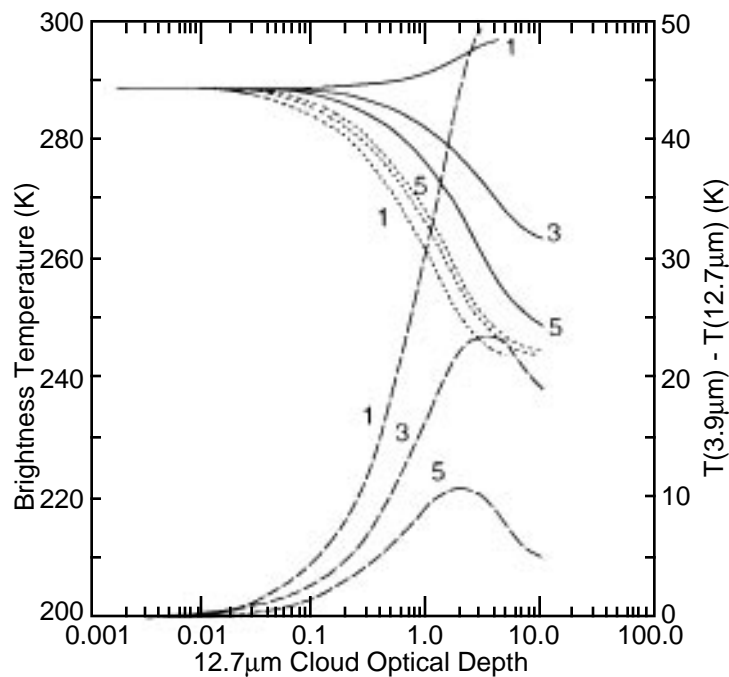
to the scene value of  $T_{cld}$ . The difference between the observed  $T$  and  $T_{cld}$  for each pixel outside the cluster is interpreted as a cloud fraction  $C < 1$ , so  $C$  is computed for each pixel. The optical depth and spherical particle size category are determined for each pixel using the visible and 3.7- $\mu\text{m}$  radiances with  $T_{cld}$  and  $C$ . The use of the 3.7- $\mu\text{m}$  data during the day complicates (4.3-4) because there is some solar reflectance at that wavelength. The observed radiance has an additional term

$$B(T) = \varepsilon(\tau, r_e; \mu)B(T_{cld}) + [1 - \varepsilon(\tau, r_e; \mu)]\varepsilon_s B(T_{cs}) + \frac{\mu_o E_o}{\pi} \left\{ \rho(\tau, r_e; \mu_o, \mu, \phi) + \frac{[1 - \alpha_c(\tau, r_e; \mu_o) - \varepsilon(\tau, r_e; \mu_o)][1 - \alpha_c(\tau, r_e; \mu)]\rho_s(\mu_o, \mu, \phi)}{1 - \alpha_{sd}\alpha_{cd}(\tau, r_e)} \right\} \quad (4.3-6)$$

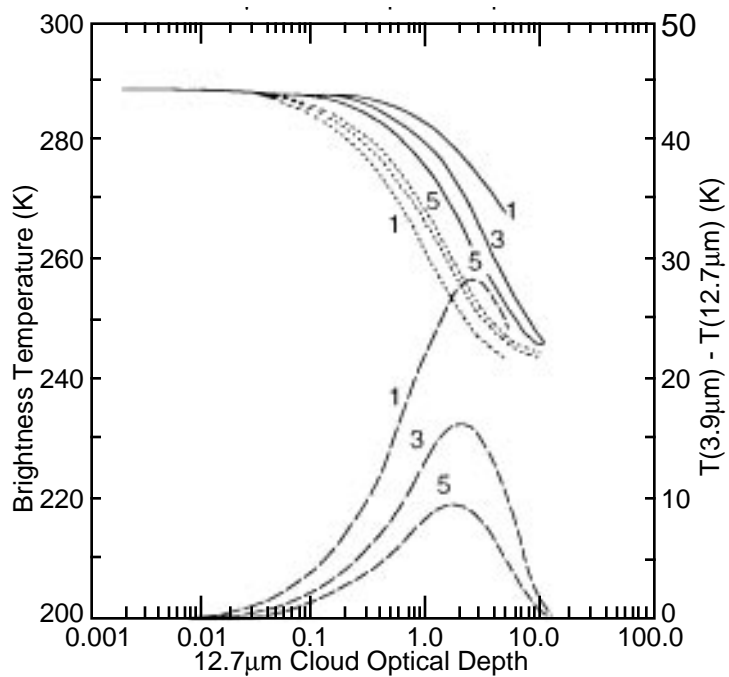
where the subscript  $\lambda$  has been dropped for simplicity. The effective emittance includes both the absorption and scattering effects of the cloud. The first term in (4.3-6) represents the radiance emitted by the cloud, while the second gives the radiance emitted by the underlying surface and atmosphere that is transmitted through the cloud. The third term represents the solar radiation that is reflected back to space. Within the large brackets, the first term is the cloud bidirectional reflectance and the remainder approximates the fraction of solar radiation transmitted to the surface by the cloud and reflected back to space after passing again through the cloud. If the first square-bracketed quantity in this term is less than zero, it is set equal to zero indicating that none of the solar radiation reaches the surface. The surface bidirectional reflectance and diffuse albedo are  $\rho_s$  and  $\alpha_{sd}$ , respectively. The cloud directional and diffuse albedos are  $\alpha_c$  and  $\alpha_{cd}$ , respectively. These terms are formally defined by Minnis et al. (1993b). Atmospheric absorption and scattering effects are neglected in (4.3-6), which can be used for any wavelength since  $E_o$  and  $\varepsilon$  approach zero for infrared and visible wavelengths, respectively.

Stone et al. (1990) continued the development of the technique using *BTD*'s between infrared window (10–12.7  $\mu\text{m}$ ) and near-infrared (3.5–4.0  $\mu\text{m}$ ) radiances by comparing model calculations of daytime *BTD*'s for various sizes of ice spheres to GOES and AVHRR data. Figure 4.3-4 shows the Stone et al. (1990) model calculations of  $T_{3.9}$ ,  $T_{12.7}$ , and  $BTD_{3.9-12.7}$  for three different effective ice sphere sizes (as defined by Stone et al. 1990, model 1:  $D_e = 8 \mu\text{m}$ ; model 3:  $D_e = 32 \mu\text{m}$ ; model 5:  $D_e = 128 \mu\text{m}$ ). The daytime  $BTD_{3.9-12.7}$  values (Fig. 4.3-4(a)) are more sensitive to changes in  $D_e$  than their nocturnal counterparts (Fig. 4.3-4(b)) because of the reflected component in the 3.9- $\mu\text{m}$  radiances. This increased sensitivity is also found for liquid water clouds. Han (1992) exploited the daytime sensitivity of  $T_3$  to particle size to construct the first semiglobal survey of  $r_e$  for water clouds using ISCCP AVHRR data. His method explicitly solves (4.3-6) through an iterative technique for  $\tau_{0.67}$ ,  $T_{cld}$ , and  $r_e$  using  $\rho_{0.67}$ ,  $T_{3.73}$ , and  $T_{10.8}$  and a set of lookup tables derived from radiative transfer calculations. The lookup tables are limited to  $\mu > 0.9$ ,  $\mu_o > 0.2$ , and liquid water droplets. The method is applied only to pixels having  $T_{cld} > 273 \text{ K}$ . This technique has produced reasonable results over the middle and low latitudes where it was applied to a set of AVHRR data. Platnick and Twomey (1994) used a similar method to study the susceptibility of cloud albedo to cloud droplet size changes. In a limited comparison using ASTEX data, Platnick and Valero (1995) found good agreement between in situ and satellite retrieved droplet sizes. The results provide additional confidence for using this multispectral approach.

Young et al. (1993) and Young et al. (1994) expanded on the approach of Han (1992) by using models of reflectance and emittance developed by Minnis et al. (1994) for all angles, cloud and surface temperatures, cloud phase, optical depths, and particle sizes. Their iterative scheme is similar to that of Han (1992) but it contains some additional features. The Young et al. (1994) method selects an ice or water model automatically using the initial comparison of the computed  $T_{3.73}$  with the observed value. Mie scattering calculations are used for the water droplets. The ice cloud models are based on the hexagonal crystal and spheroid parameterizations of Takano and Liou (1989), Minnis et al. (1993b), and Takano et al. (1992). The initial applications of this methodology compare well with in-situ and ground-based radar measurements of particle size taken during FIRE II and ASTEX.



(a) Daytime.



(b) Nighttime.

Figure 4.3-4. Composite plots of 3.9- $\mu\text{m}$  and 12.7- $\mu\text{m}$  brightness temperature and their differences as functions of the 12.7- $\mu\text{m}$  optical depths for model cirrus clouds during (a) daytime and (b) nighttime situations. The numbers next to each curve relate to model values of effective particle size. Models 1, 3, and 5 refer to effective ice-sphere radii of 4, 16, and 64  $\mu\text{m}$ , respectively. The solid and short-dashed curves are for the 3.9- $\mu\text{m}$  and 12.7- $\mu\text{m}$  temperatures, respectively. The long-dashed curves relate to the temperature differences (adapted from Stone et al. 1990).

Another mixed technique, applicable only to water clouds over ocean in daylight, involves the simultaneous use of microwave radiances to infer liquid water path  $W_{liq}$  and visible radiances to derive optical depth. Minnis et al. (1992) used radiative transfer models of visible reflectance in terms of  $\tau_{0.65}$  and  $r_e$  and

$$r_e = \frac{3Q_e W_{liq}}{4\delta_{liq}\tau_{0.65}(\rho, r_e)} \quad (4.3-7)$$

to obtain  $r_e$  from surface-based microwave measurements of  $W_{liq}$  and GOES visible data. The density of liquid water is  $\delta_{liq}$ . This equation is a generalized version of an approximation by Stephens (1978) in which  $Q_e$  is assumed to have a value of 2 for visible wavelengths. The extinction efficiency actually varies from 2.3 to 2 for  $r_e$  ranging from 2 to 32  $\mu\text{m}$ . Minnis et al. (1992) found excellent agreement between their derived effective radii assuming  $Q_e = 2$  and the available in-situ data taken off the coast of California during the July 1987 FIRE stratocumulus experiment. Young et al. (1992) applied this visible-microwave approach to derive  $r_e$  from nearly coincident DMSP SSM/I microwave data and GOES visible radiances. The resulting mean value of  $r_e$  was 9.2  $\mu\text{m}$ , identical to that derived using the technique of Young et al. (1994) applied to nearly coincident AVHRR data. The values from the visible-microwave method, however, ranged from 6 to 14  $\mu\text{m}$  compared to 7 to 11  $\mu\text{m}$  from the AVHRR data. The most likely cause of the range differences may be the sensitivity of the reflectance techniques to the droplets in the top of the cloud (cf. Nakajima and King 1990). Further, the visible-microwave method must simultaneously account for the reflectance and liquid water path of the entire cloud. In nonprecipitating conditions, stratiform clouds tend to have smaller droplets at the bottom. The opposite situation is likely to occur for precipitating clouds. Additional research is required to reconcile the discrepancies between the two methods.

#### 4.3.3. Data and Model Database

The primary input data to COPRS include the following elements from a CERES cloud-algorithm unit data block ( $16 \times 16$  imager pixels): mean  $T_{cs\lambda}(L)$ ,  $\rho_{cs\lambda}(L)$ ,  $\alpha_{sd\lambda}(L)$ ,  $T_{cs\lambda}(S)$ ,  $\alpha_{sd\lambda}(S)$ , and  $\rho_{cs\lambda}(S)$ ,  $T(p)$ ,  $\tau_{H_2O\lambda}(p)$ ,  $\tau_{aer}$ ,  $\tau_{O_3}$ ,  $E_{o\lambda}$  and  $\mu_o$ ,  $\mu$ , and  $\phi$  for the center of the block. The parenthetical  $L$  and  $S$  refer to land and sea, respectively. The clear-sky albedo is  $\alpha_s(\mu_o)$  and the clear-sky diffuse albedo is  $\alpha_{sd}$ . The spectral water vapor optical depth is  $\tau_{H_2O\lambda}(p)$ , and the visible aerosol and ozone optical depths are  $\tau_{aer}$  and  $\tau_{O_3}$ , respectively. The spectral radiances and geoclassification for each pixel in the data block are also included. These input elements have been described in detail in section 4.1. Other inputs derived in the section 4.2. subsystem are the clear, single-layer, or multiple-layer indices for each pixel and the values for the cloud layer temperatures for all layers detected for the eight surrounding data blocks.

To maintain a standard reference, optical depth is reported in terms of the visible channel optical depth,  $\tau_{0.65}$ . The optical depth at a given wavelength  $\lambda_1$  for any effective particle size can be related to the optical depth at any other wavelength  $\lambda_2$  by

$$\tau_{\lambda_1} = \tau_{\lambda_2} \frac{Q_{e\lambda_1}}{Q_{e\lambda_2}} \quad (4.3-8)$$

For simplicity, the wavelength subscript is dropped for the visible optical depth. It will continue to be used for other wavelengths. The AVHRR channel numbers 3, 4, and 5 will hereafter replace the wavelength designations for  $\lambda = 3.7, 10.9,$  and  $11.9 \mu\text{m}$ , respectively.

The cloud solar radiance model database consists of lookup tables giving the spectral cloud reflectance  $\rho_\lambda(r_e \text{ or } D_e; \tau; \mu_o, \mu, \phi)$ , cloud albedo  $\alpha_c(r_e \text{ or } D_e; \tau; \mu_o)$ , and diffuse cloud albedo  $\alpha_{cd}(r_e \text{ or } D_e; \tau)$  for the relevant channels: 0.65, 1.60, and 3.75  $\mu\text{m}$  for VIRS and AVHRR (Minnis et al. 1993b; Minnis et al. 1994) plus 2.12  $\mu\text{m}$  for MODIS. The lookup tables were constructed for  $r_e = 2, 4, 6, 8, 12, 16,$  and

32  $\mu\text{m}$  and  $D_e = 6, 18, 24, 30, 45, 75, 105, 123,$  and  $135 \mu\text{m}$  with  $\tau = 0.25, 0.5, 1, 2, 3, 4, 8, 16, 32, 64, 96,$  and  $128$ ;  $\mu_o = 1, 0.95, 0.85, \dots, 0.05$ ;  $\mu = 1, 0.9, 0.8, \dots, 0.1$ ; and  $\phi = 0, 7.5, 15, 30, 45, \dots, 165, 172.5, 180^\circ$ . The optical depth range for  $3.75 \mu\text{m}$  ends at  $\tau = 32$  because the reflectance is essentially constant for greater optical depths. For bright backgrounds, a set of lookup tables giving the  $0.65\text{-}\mu\text{m}$  reflectance at the top of the atmosphere has been developed for the same sets of angles. These lookup tables were computed for all of the water and ice clouds using surface albedos ranging from 0.20 to 0.80 in increments of 0.15 for  $\tau = 0.25, 0.5, 1, 2, 3, 4,$  and  $8$  and  $p = 1000, 700, 400,$  and  $100$ . No water vapor or ozone absorption was included in these calculations.

Figure 4.3-5 shows examples of the cloud reflectance lookup tables normalized to the cloud albedo [i.e., the ratio  $\rho_\lambda(\mu_o, \mu, \phi)/\alpha_c(\mu_o)$ ] for  $r_e = 16 \mu\text{m}$  (Fig. 4.3-5(a)) and  $D_e = 37 \mu\text{m}$  (Fig. 4.3-5(b)) for channel 3 with  $\tau = 4$  and  $\mu_o = 0.55$ . The effective volumes of these two particle distributions are close, but the diffuse albedos are 0.13 and 0.06, respectively. Although the reflectance patterns (Fig. 4.3-5) are somewhat similar, they show some distinct features typical of the differences between scattering from spheres and hexagonal crystals (Minnis et al., 1993b). The relative reflectance patterns for the visible channel (Fig. 4.3-6) are different than those in Fig. 4.3-5, but the discrepancies between the ice and water reflectances are quite noticeable. In contrast to the  $3.75\text{-}\mu\text{m}$  results, the visible-channel liquid-cloud diffuse albedo of 0.31 is less than the value of 0.42 for ice-cloud model. Cloud albedo  $\alpha_c$  increases with decreasing particle size for both channel 3 and the visible channel as demonstrated in the reflectance plots of the models for  $r_e = 4$  and  $16 \mu\text{m}$  in Figs. 4.3-7 and for  $D_e = 23$  and  $108 \mu\text{m}$  in Figs. 4.3-8. The ice models used here are based on randomly oriented hexagonal ice columns and were selected because the phase functions and optical properties are available for the range of ice crystal sizes and wavelengths needed for the retrievals. The hexagonal ice crystal is commonly found in cirrus clouds and provides the basic building block in some more complex crystals found in ice clouds. Optical properties have been derived for other shapes (e.g., Macke et al., 1996) that would produce different values for optical depth and, perhaps, particle size for a given set of conditions. The optimal model for representing cirrus cloud microphysics has not yet been determined. Although it is clear that retrieved properties will be sensitive to shape, much additional research is required to understand the errors introduced by using a particular model in the retrieval methodology.

For each discrete particle size, the cloud emittance models comprise eight sets of 32 coefficients corresponding to  $\tau = 0.25, 0.5, 1, 2, 4, 8, 16,$  and  $32$  for channels 3, 4, or 5 for the VIRS and AVHRR plus the  $8.55\text{-}\mu\text{m}$  channel of MODIS. The following regression formula was fitted to effective emittances computed using (4.3-4) and radiances calculated with the adding-doubling radiative transfer model of Minnis et al. (1993b)

$$\varepsilon(\zeta, \mu, \xi) = \sum_{i=0}^2 \sum_{j=0}^4 \sum_{k=0}^1 d_{ijk} \zeta^i \mu^j \xi^k \quad (4.3-9)$$

where  $\zeta = 1/(\ln(\Delta T))$  and  $\xi = 1/\ln(T_{cs})$  and  $\Delta T = T_{cs} - T_{cld}$ . Interpolation is used to determine  $\varepsilon$  for optical depths between the model values. Details of the reflectance and emittance models can be found in Minnis et al. (1997). For channel 3, the standard error of this parameterization is  $< 0.015$  and  $0.005$  for the water droplet and ice crystal distributions, respectively, when  $\varepsilon < 1$ . Slightly larger errors are encountered in the fits for  $\varepsilon > 1$  for the smaller water droplets. Standard errors for channels 4 and 5 are less than 0.003 and generally close to 0.001 for water droplets and less than 0.001 for ice crystals. Figure 4.3-9 shows the  $BTD_{3-4}$  and  $BTD_{4-5}$  computed using the effective emittances from (4.3-9) for hypothetical nocturnal clouds viewed from  $\theta = 45^\circ$  at a temperature  $T_{cld} = 255 \text{ K}$  over a clear scene having a brightness temperature of  $T_{cs} = 300 \text{ K}$ . Four clouds are represented, two comprising water droplets with effective radii  $r_e = 6$  and  $16 \mu\text{m}$  and the other two consisting of randomly oriented hexagonal ice crystals having effective diameters  $D_e = 31$  and  $105 \mu\text{m}$ . As  $\tau$  increases, the  $10.8\text{-}\mu\text{m}$  temperature approaches  $T_{cld}$ . It is clear that, for both the water droplet and

ice crystal models,  $BTD_{3-4} > BTD_{4-5}$ . This greater difference is typical for most cold clouds, and the ice models are obviously distinguishable from the water droplet models. Differences between  $BTD_{3-4}$  for  $D_e = 31$  and  $105 \mu\text{m}$  are smaller than those between  $BTD_{4-5}$  at the smaller optical depths (warmer brightness temperatures), while the reverse is true for larger optical depths. During the daytime, the  $BTD_{3-4}$  for  $D_e = 31$  and  $105 \mu\text{m}$  are always greater than  $BTD_{4-5}$  because of the solar contribution to the channel-3 radiance.

Atmospheric corrections for the solar channel are performed using the models and methods of Minnis et al. (1993b). Corrections for atmospheric water vapor are applied to the infrared and near-infrared channels using correlated-k fits (Kratz 1995; see also Appendix). When the models are applied, reflectances are computed for each appropriate channel at  $\mu_o$ ,  $\mu$ , and  $\phi$  for the center latitude and longitude of the data block over a range of particle sizes and optical depths for both land and ocean. Emittances are computed for the same particle sizes and optical depths at  $\mu$  using the initial guess of  $T_{cld}$ . The model results are then corrected for atmospheric attenuation. A clear-sky bidirectional reflectance model and spectral surface emittance are required in the analysis.

#### 4.3.4. Methodologies

The multispectral reflectance techniques are sensitive to a wide range of particle sizes but are limited to daytime. Emittance methods are applicable at all times, but they are sensitive to a smaller range of  $r_e$  and can be used only when the cloud is semitransparent. The 3-channel mixed methods are the only techniques available using current global satellite data and are applicable to a wide range of optical depths. They cannot be used at night, however, and are sensitive to a smaller range of particle sizes than the solar methods. There are also many other situations in which one or all of the techniques will fail to retrieve the desired parameters (see section 4.3.5.2.). To overcome these deficiencies, the COPRS will utilize all three approaches to arrive at the most reliable estimates of the cloud properties in as many situations as possible. For application to CERES/VIRS, the 3-channel reflectance-emittance techniques will serve as the primary methods for simultaneous retrieval of optical depth, effective particle size, and phase. The reflectance methods generally rely on a  $2.13\text{-}\mu\text{m}$  channel to determine particle size. This channel will be unavailable on VIRS. There is some skill in the reflectance methods, however, to determine particle size and phase using only the visible and  $1.60\text{-}\mu\text{m}$  channels. Therefore, the reflectance method will be applied during the daytime to verify phase and whenever a solution is unavailable from the 3-channel method. When the MODIS is operating, it will be possible to apply a full-scale reflectance technique because of the wide choice of channels. Whenever the primary and secondary methods fail, a 3-channel infrared method is applied during the daytime. The same 3-channel infrared method is applied at night in most cases. For this Release-2 algorithm using VIRS, the three channels are  $3.75$ ,  $10.8$ , and  $12 \mu\text{m}$ . For MODIS, a 4-channel method will be possible because of the additional  $8.55\text{-}\mu\text{m}$  sensor. In all cases, both day and night, the results derived from each method will be compared for consistency and to arrive at a single result. The decision-tree selecting the final values will incorporate information regarding the reliability of each technique for the given conditions.

##### 4.3.4.1. Daytime Cloud Optical Depth, Particle Size, and Cloud Temperature

**4.3.4.1.1. 0.65-3.75-10.8-11.9 $\mu\text{m}$  method.** This four-channel method is essentially an expansion of the three-channel method described by Minnis et al. (1995). The procedure follows the three-channel approach to reach an initial solution. The results are then retained or revised based on several criteria. This approach is detailed below.

Given  $\rho_{cs}$  (0.65),  $\rho_{cs}$  (3.75),  $T_{cs4}$ , and  $T_{cs3}$ , the phase, particle size, optical depth, and cloud temperature are evaluated for each pixel by iteratively solving first for  $\tau$  using the observed visible reflectance  $\rho_{0.65}$ , second for  $T_{cld}$  using  $T_4$  in (4.3-4), and finally using  $T_3$  in (4.3-6) to obtain  $r_e$ . The optical depth is

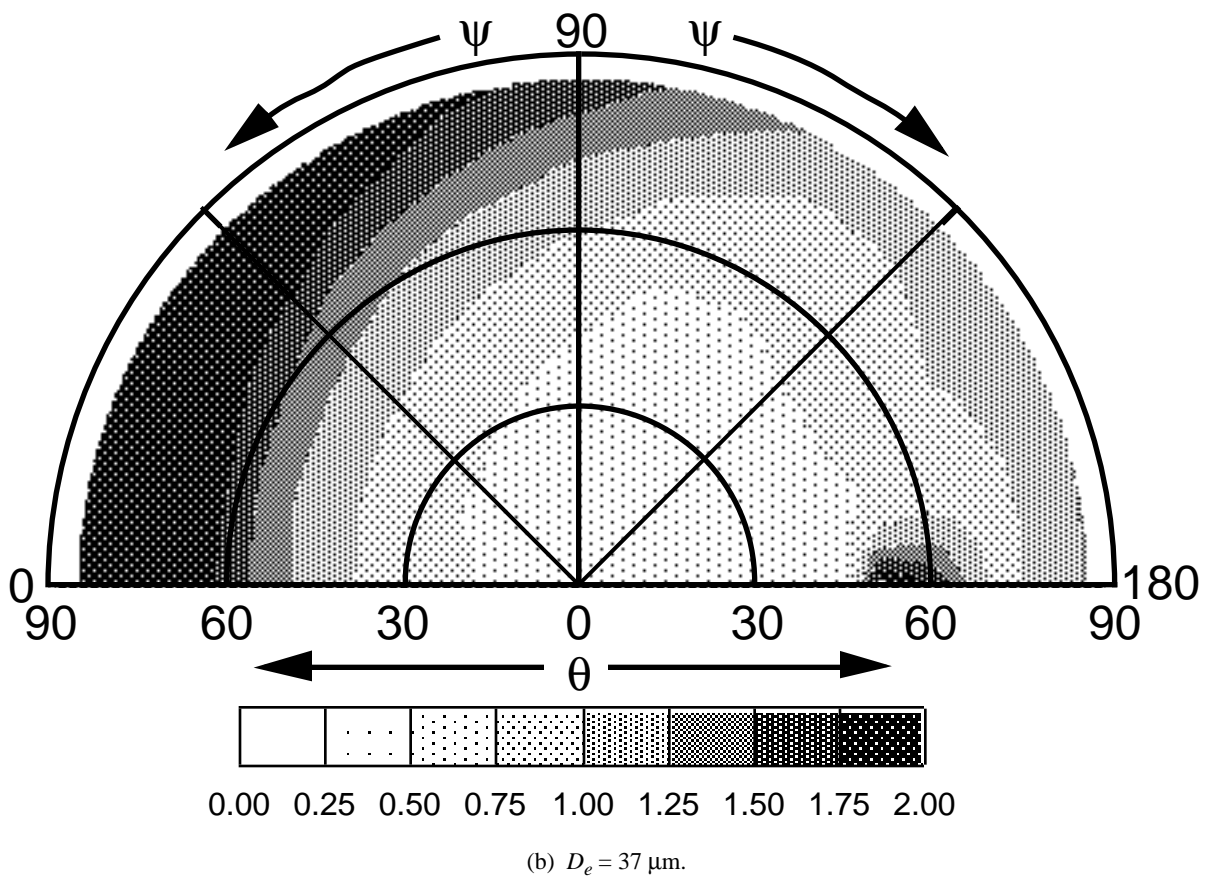
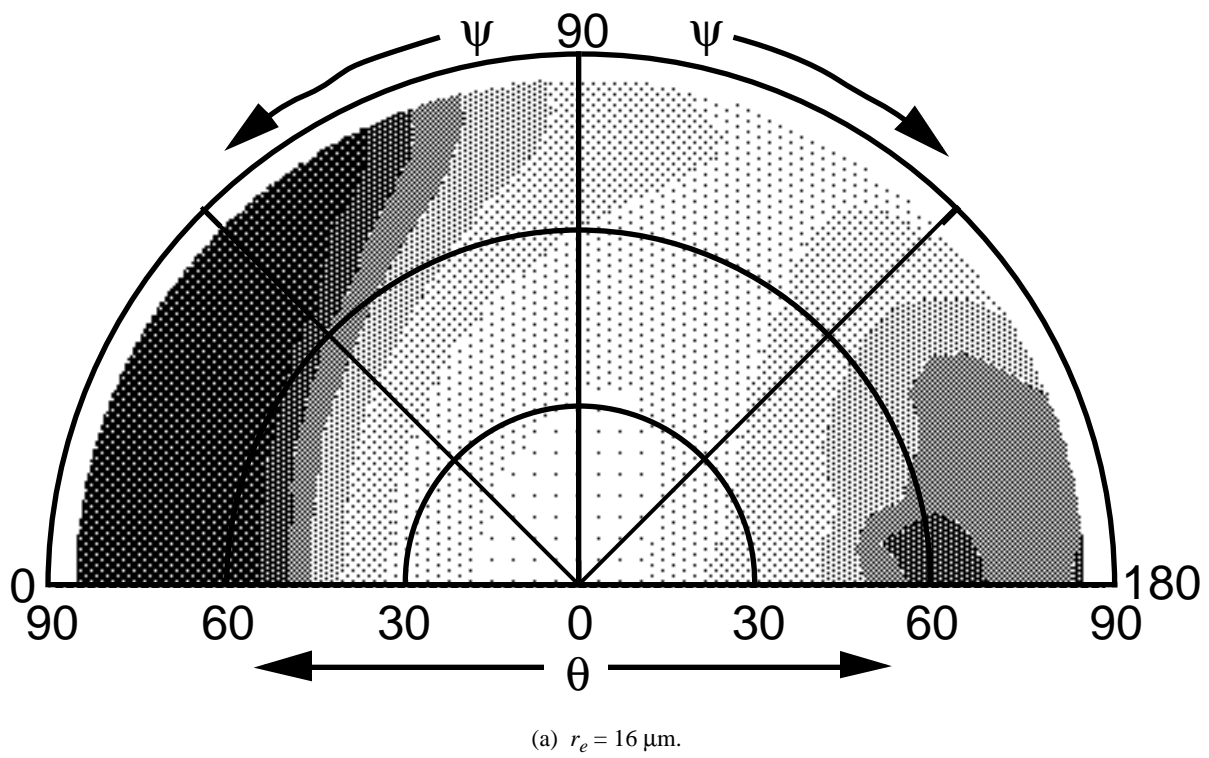


Figure 4.3-5. Normalized theoretical anisotropic reflectance values for  $\tau = 4$ ,  $\mu_o = 0.55$ , and  $\lambda = 3.75 \mu\text{m}$ .

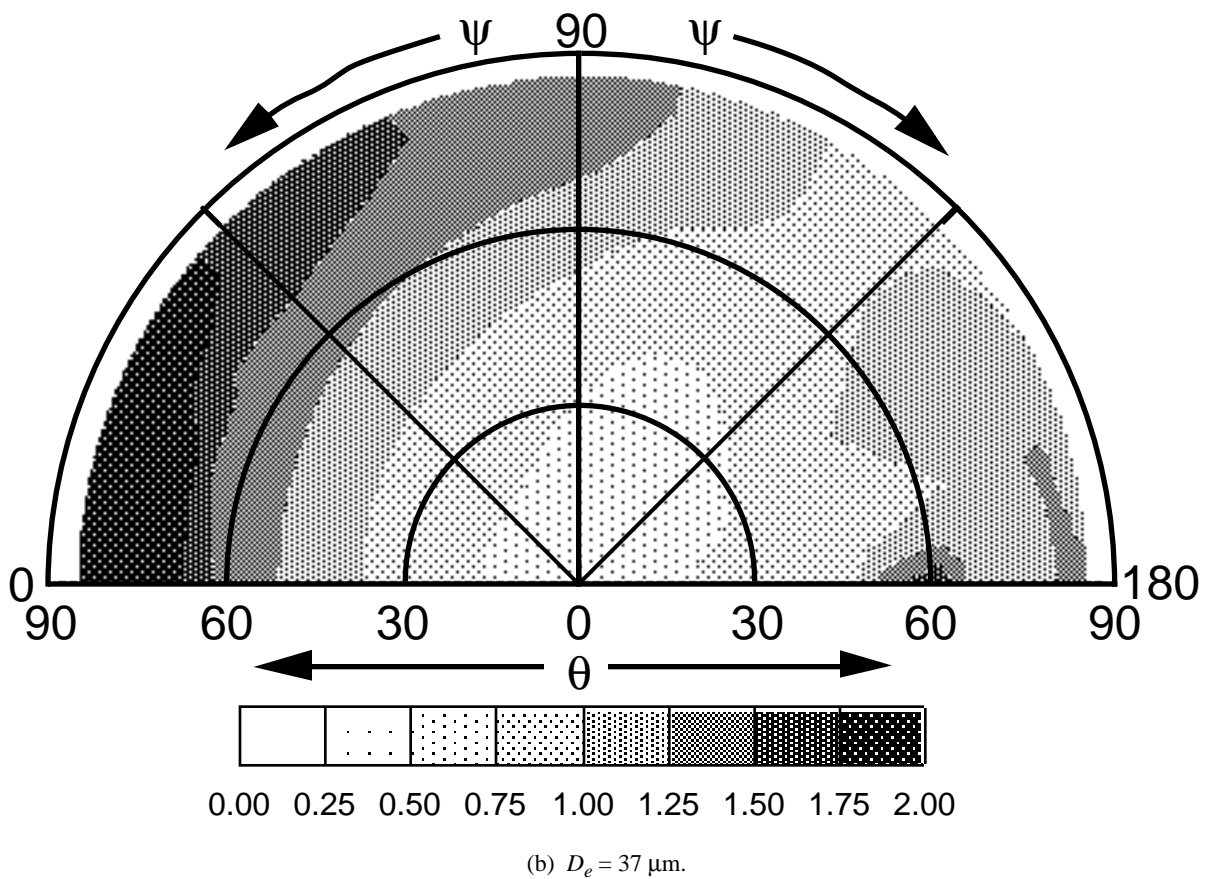
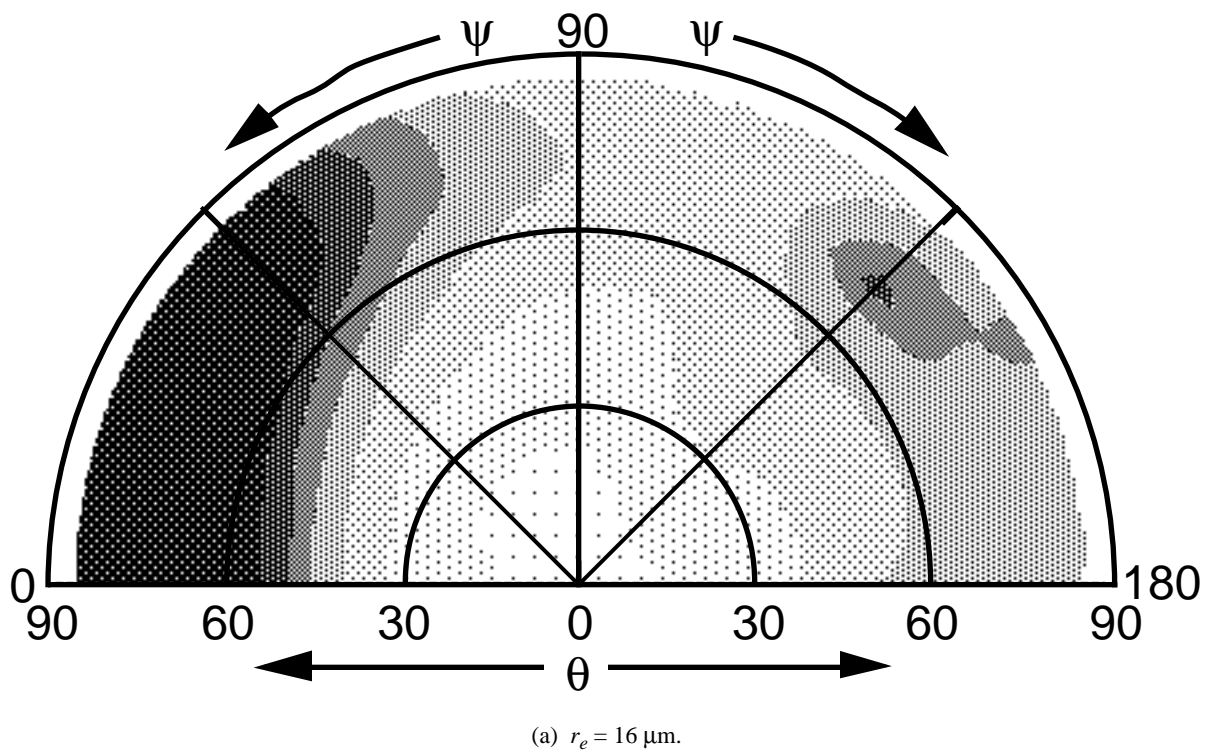
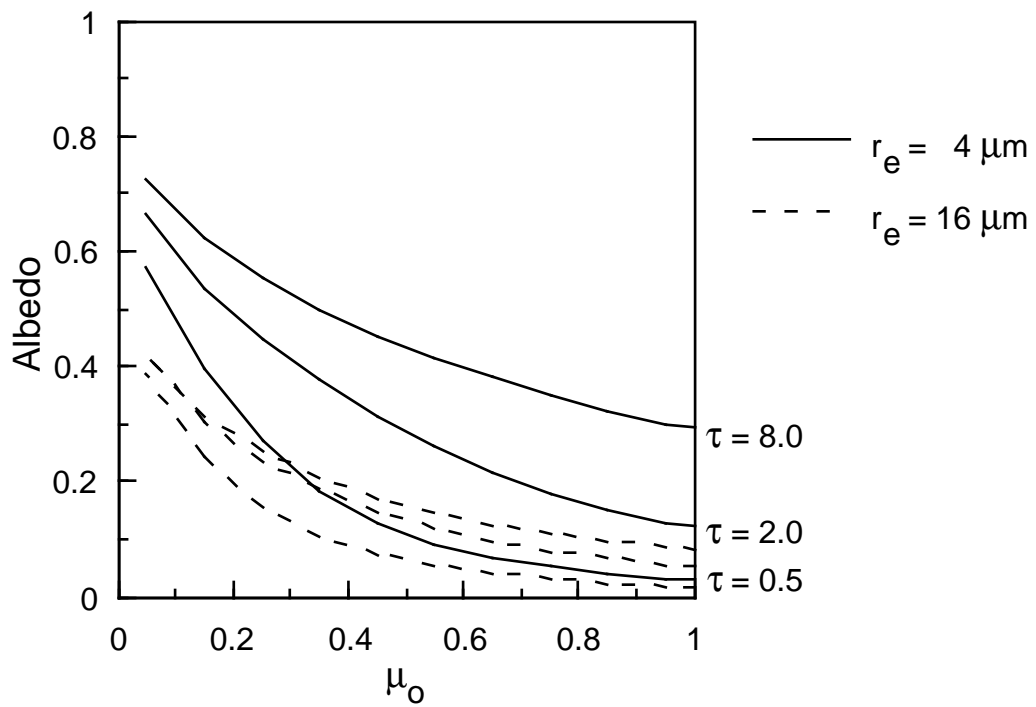
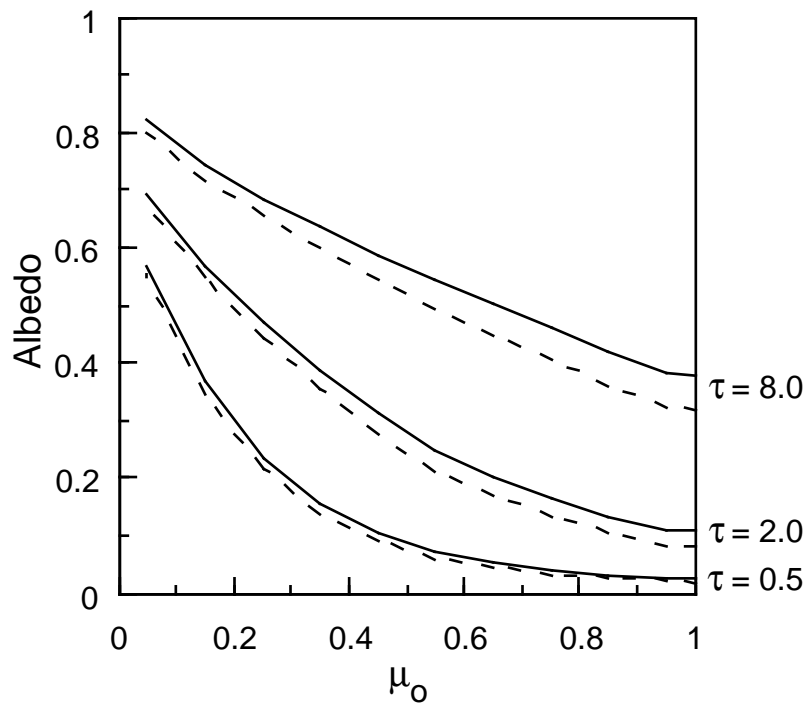


Figure 4.3-6. Normalized theoretical anisotropic reflectance values for  $\tau = 4$ ,  $\mu_o = 0.55$ , and  $\lambda = 0.65 \mu\text{m}$ .

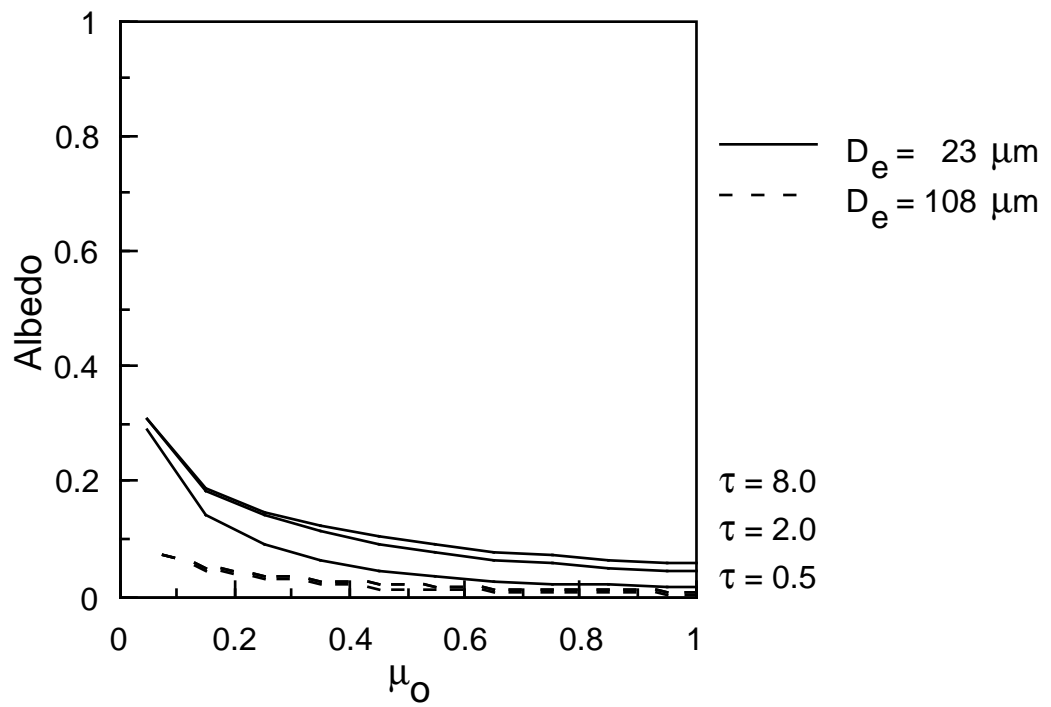


(a)  $\lambda = 3.75 \mu\text{m}$ .

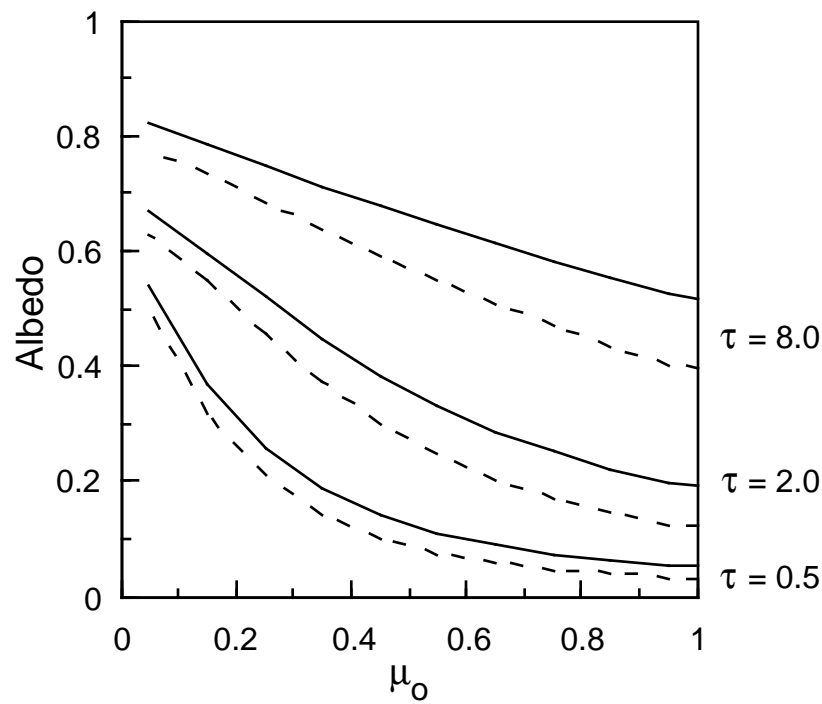


(b)  $\lambda = 0.65 \mu\text{m}$ .

Figure 4.3-7. Theoretical albedos for 4- $\mu\text{m}$  and 16- $\mu\text{m}$  water droplets.



(a)  $\lambda = 3.75 \mu\text{m}$ .



(b)  $\lambda = 0.65 \mu\text{m}$ .

Figure 4.3-8. Theoretical albedos for 23- $\mu\text{m}$  and 108- $\mu\text{m}$  ice particles.

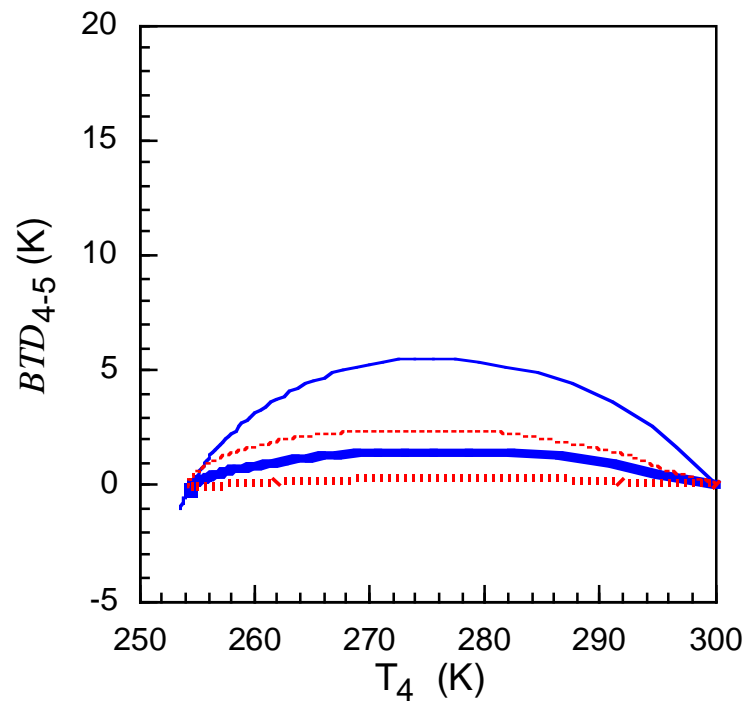
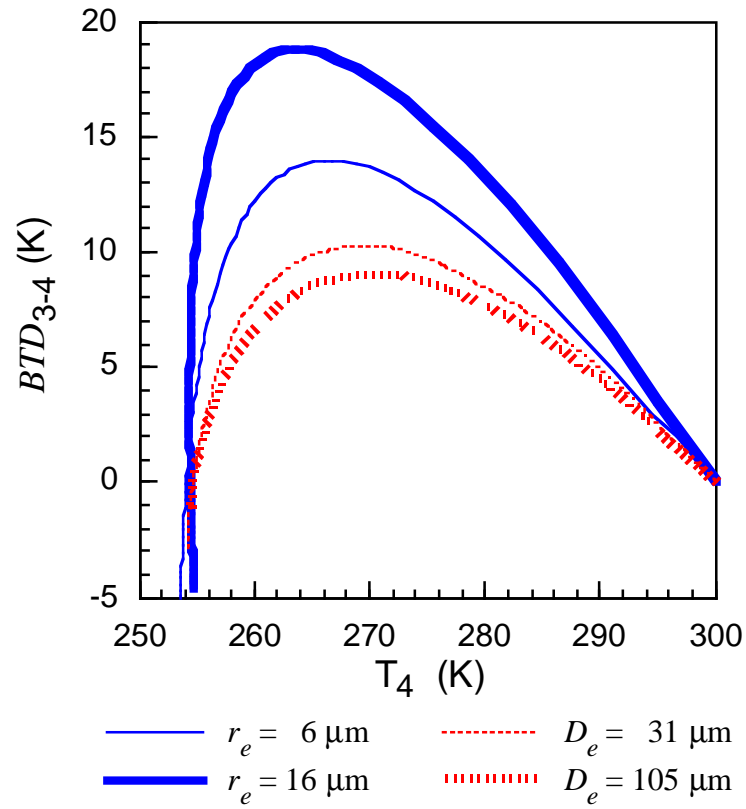


Figure 4.3-9. Theoretical brightness temperature differences for  $T_{cld} = 255$  K,  $\Theta = 45^\circ$ .

obtained by matching the observed reflectance to a parameterization of radiative transfer calculations of reflectance in terms of cloud optical depth. This model is

$$\rho_{0.65} = \sum \rho_i / (1 - \zeta), \quad i = 1, 5 \quad (4.3-10)$$

where  $\zeta$  is a regression correction parameter, and the  $\rho_i$  are parameterizations of the multiple scattering and absorption by the atmosphere, scattering by the cloud, and reflectance by the surface (Minnis et al. 1993b). The reflectance parameterization is described briefly below.

The visible-channel reflectance contributed by the cloud and the atmosphere above it is

$$\rho_1 = t_{a1} \rho_{c1} = t_{a1} \rho_{c1}(\tau, \tau_{R1}) \quad (4.3-11a)$$

where the transmittance,

$$t_{a1} = \exp[-\tau_{O_3}(1/\mu_o + 1/\mu)]$$

and the Rayleigh optical depth above the cloud is  $\tau_{R1}$ . The beam reflectance by the surface is

$$\rho_2 = t_c \downarrow t_c \uparrow \rho_s \quad (4.3-11b)$$

where the downward and upward cloud transmittances are

$$t_c \downarrow = \exp[-(1 - f_D)\tau/\mu_o]$$

and

$$t_c \uparrow = \exp[-(1 - f_D)\tau/\mu]$$

respectively, and  $f_D$  is the fraction of the beam that is forward scattered because of diffraction or direct transmission through the droplet or crystal. Its value is generally greater than or equal to 0.5 at visible wavelengths. The proportion of the radiation that is scattered out of the forward direction, reflected by the surface, and transmitted diffusely back through the cloud to space is approximated as

$$\rho_3 = \alpha_{sd}(1 - \alpha_{cd})(1 - t_c \uparrow - \alpha_c) \quad (4.3-11c)$$

The fourth term,

$$\rho_4 = \left[ \rho_{R2}(1 - \alpha_c^{0.5}) - \alpha_{R1} \alpha_c^2 \right] (1 - \alpha_{cd}) \quad (4.3-11d)$$

accounts for the relative thickness of the Rayleigh layers above and below the cloud. The effects of the two Rayleigh layers are included by using the direct Rayleigh reflectance term for the bottom layer,  $\rho_{R2}$ , and the Rayleigh albedo for the top layer,  $\alpha_{R1}$ . The fifth term,

$$\rho_5 = a_0 + a_1 \left( \frac{\tau}{1 + \tau} \right)^2 \mu_o^2 \alpha_s + a_2 \alpha_{sd} \quad (4.3-11e)$$

accounts for an overestimate in the surface contribution to the reflectance by  $\rho_2$  for small cloud optical depths. The coefficients,  $a_i$ , depend on the microphysical model. The denominator in (4.3-11) uses the parameter

$$\zeta = b_0 + b_1 \ln \tau + b_2 \alpha_{sd} \ln \tau + b_3 \alpha_{sd} \quad (4.3-12)$$

to minimize biases in the parameterization. The coefficients,  $b_i$ , also vary with the microphysical model. Details of this parameterization are given by Minnis et al. (1993b).

The model represented by (4.3-11) yields relatively accurate optical depths over dark surfaces for all optical depths (Minnis et al. 1993b). For brighter surfaces, such as deserts, clouds, and snow, the optical depth errors can be greater than 50% for relatively thin clouds. Therefore, the lookup tables for top-of-the-atmosphere reflectance are used if  $\alpha_{sd} > 0.20$  and  $\tau \leq 8$ . The lookup table values are first multiplied by  $t_{a1}$  to account for ozone variability and then interpolated to obtain the top-of-the-atmosphere reflectances corresponding to the observed or expected clear-sky albedo and the specified cloud and angular conditions. These values replace the results of (4.3-11) for the thin clouds over bright scenes.

The three equations (4.3-4), (4.3-6), and (4.3-11) are solved using the iterative process outlined in Figure 4.3-10 for each cloudy pixel. An initial guess solves (4.3-11) for  $\tau$  assuming a water-droplet model with  $r_e = 8 \mu\text{m}$ . Cloud emittance is computed for channels 3 and 4 using (4.3-9);  $T_{cld}$  is then determined from (4.3-4) at  $11 \mu\text{m}$ . If  $T_{cld} > 253 \text{ K}$ , then it is used in (4.3-6) with  $\tau$  to compute  $BTD_{3-4}(r_e)$  for the full range of particle sizes in the water droplet model. Otherwise,  $BTD_{3-4}(D_e)$  is calculated for the ice crystal models. Finally, a new estimate of particle radius,  $r_e'$ , or  $D_e'$ , is determined by matching the observed  $BTD_{3-4}$  with the model output. For the water droplet case, if  $BTD_{3-4}$  is less than the value of the greatest model radius and  $T_{cld} < 273 \text{ K}$ , the process is repeated using the ice crystal models beginning with an initial guess of  $D_e = 37 \mu\text{m}$ . Otherwise,  $r_e$  is set equal to  $r_e'$  and the process is repeated until the two values are within  $0.1 \mu\text{m}$  of each other. Likewise, in the ice crystal case, if  $T_{cld} > 233 \text{ K}$  and  $BTD_{3-4}$  is greater than that of the smallest ice crystal model, the process is repeated using the water droplet models. The test for phase is executed only after the first iteration. An additional 10 iterations are allowed before the process is ended and no solution is obtained. Most cases require fewer than six iterations. In some instances, the ice and water droplet models will produce overlapping results so that the small ice crystals may occasionally be mistakenly identified as large water droplets. Overlapped cirrus and liquid water clouds and mixed-phase clouds can produce radiances that fall between the ice and liquid models.

The three-channel approach is illustrated using 1-km AVHRR data taken near Coffeyville, Kansas during the November-December 1991 FIRE Cirrus field experiment. Figure 4.3-11(a) plots the observed  $BTD_{3-4}$  against  $T_4$  for a small area at 2054 UTC, November 26, 1991. The plotted numerals correspond to the number of pixels having the given pair of  $BTD_{3-4}$ - $T_4$  values. The curves represent the ice and water droplet model results for  $T_{cld} = 264 \text{ K}$ . Figure 4.3-11(b) is a histogram of  $r_e$  derived using the process described above for the data in Figure 4.3-11(a). In this case, the cloud is diagnosed as being a supercooled water cloud with mean  $r_e$ ,  $\tau$ , and  $T_{cld}$  values of  $9.5 \mu\text{m}$ ,  $6.5$ , and  $268 \text{ K}$ , respectively. A case where nonoverlapped high- and low-level clouds are present is shown in Figure 4.3-12 for data taken at 2042 UTC, November 28, 1991. The figure shows two-dimensional histograms of  $\rho_{vis}$  versus  $T_4$  (Fig. 4.3-12(a)) and  $BTD_{3-4}$  versus  $T_4$  (Fig. 4.3-12(b)) with a subjective estimate of the model that would best fit the histograms using the LBTM-derived (section 4.2.2.) values of  $T_{cld}$  from Figure 4.3-12(a). The full pixel-by-pixel analyses yielded the distribution of particle sizes given in Figure 4.3-13. The low-cloud top height of  $1.6 \text{ km}$  is  $0.2 \text{ km}$  higher than that derived from radar data taken at Coffeyville. The high-cloud altitude is at  $9.0 \text{ km}$ , midway between the base and top heights observed with the radar. The ice water path of the cirrus cloud is

$$W_{ice} = \delta_{ice} \sum (V_i N_{oi}) \tau / \sum Q_e A_i N_{oi} \quad (4.3-13)$$

where  $V$  and  $A$  are the volume and cross-sectional areas, respectively, of the randomly oriented hexagonal crystal  $i$  in a specified distribution defined by the normalized number of crystals  $N_o$ , and  $\delta_{ice}$  is the density of ice. The ice water path derived from the distribution in Figure 4.3-13(b) is  $132 \text{ gm}^{-2}$  a value within 5% of the  $139 \text{ gm}^{-2}$  derived from the surface radar. This result indicates the mean particle size is a reasonable estimate for the cloud. The high-cloud fraction is reduced from the LBTM analysis (Fig. 4.3-12(a)) because the cloud pixels with  $T_4 > 276 \text{ K}$  were too dim in the visible channel to solve for  $\tau$  and  $r_e$ . The mean value of  $r_e$  in Figure 4.3-13(a) yields  $W_{liq} = 47 \text{ gm}^{-2}$ , a value twice that of the

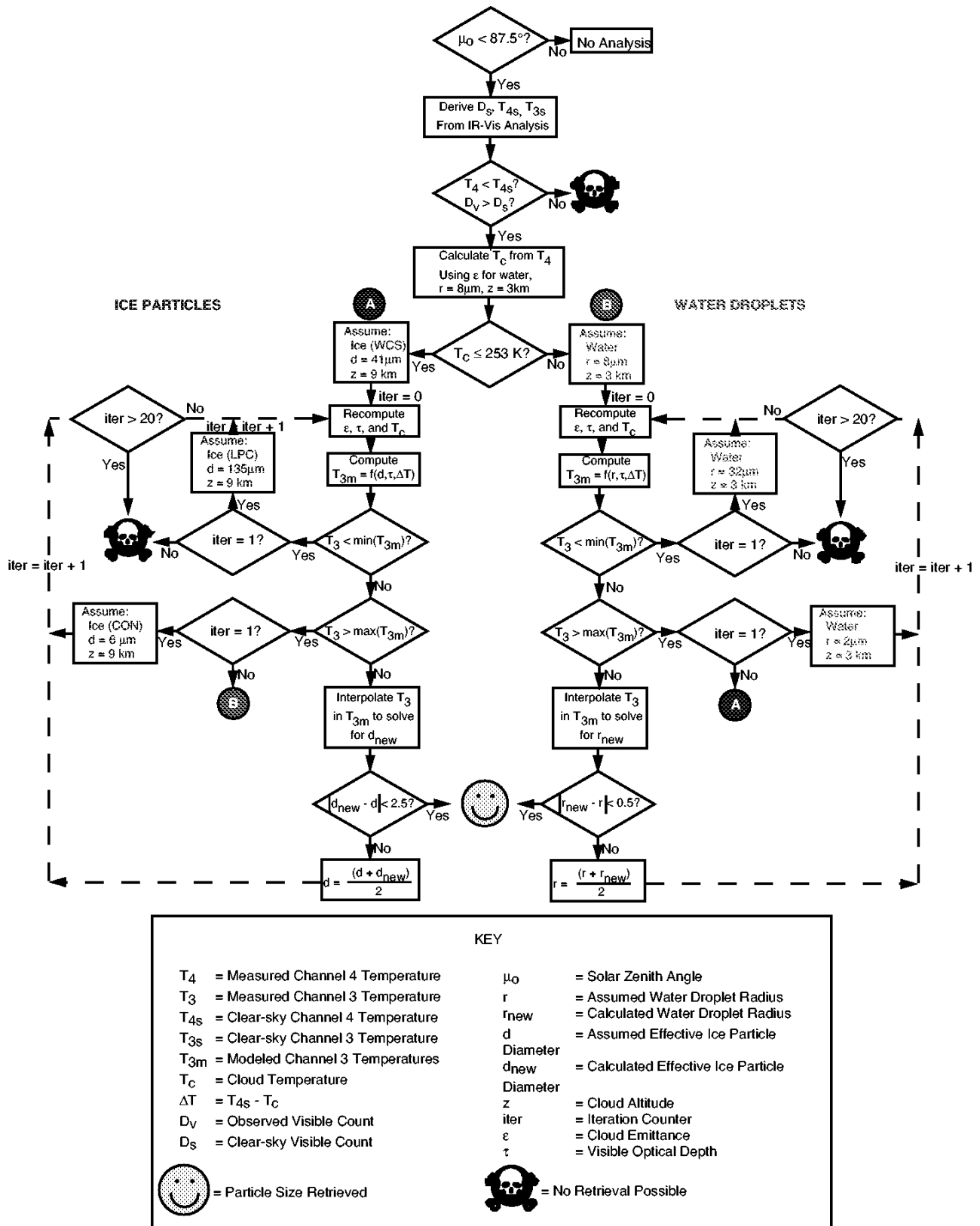
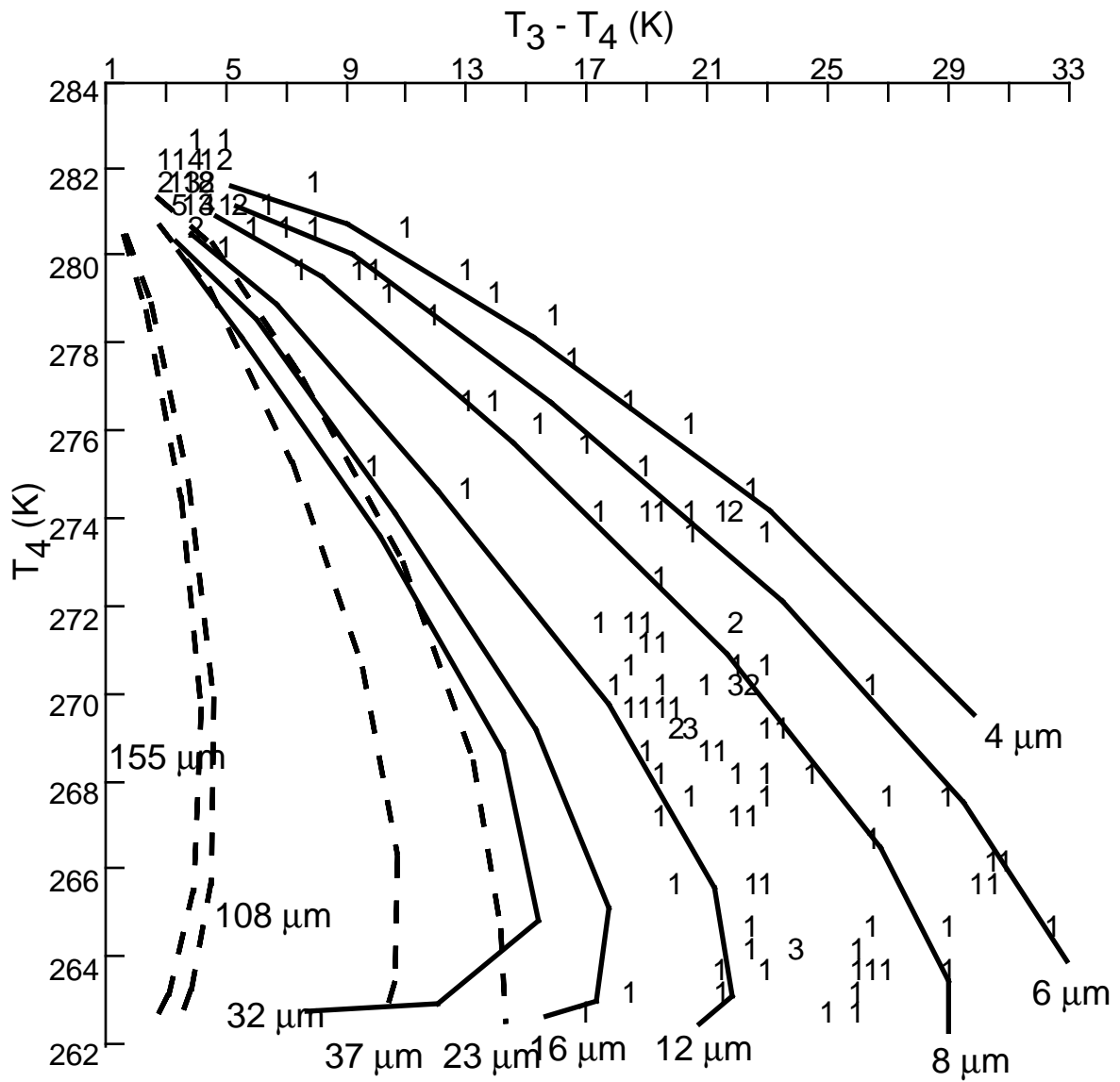
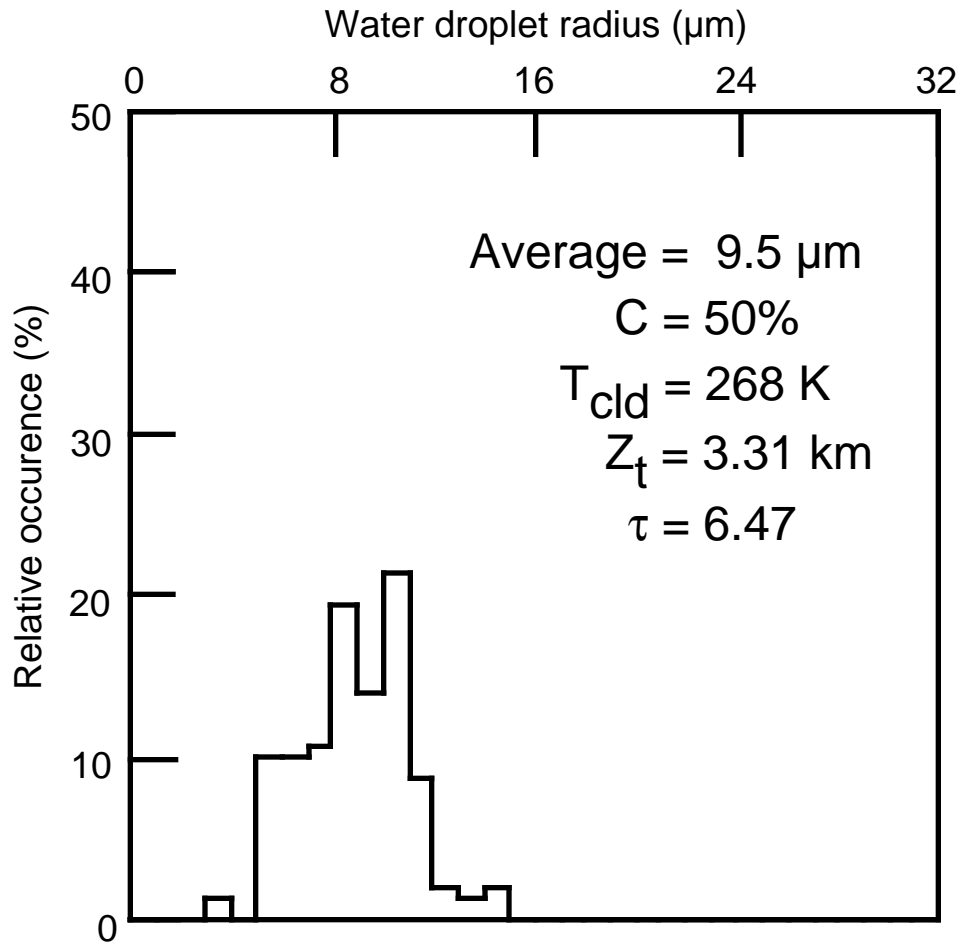


Figure 4.3-10. Flow diagram of channels 1, 3, and 4 cloud property retrieval algorithm. Effective diameter is denoted with  $d$ ; effective radius is  $r$ .



(a) Observed  $BT_{D_{3-4}}$  plotted against  $T_4$ .

Figure 4.3-11. AVHRR  $BT_{D-IR}$  histogram and water cloud retrieval in AVHRR data over 39.3°N, 98.1°W at 2054 UTC, November 26, 1991.



(b) Histogram of  $r_e$ .

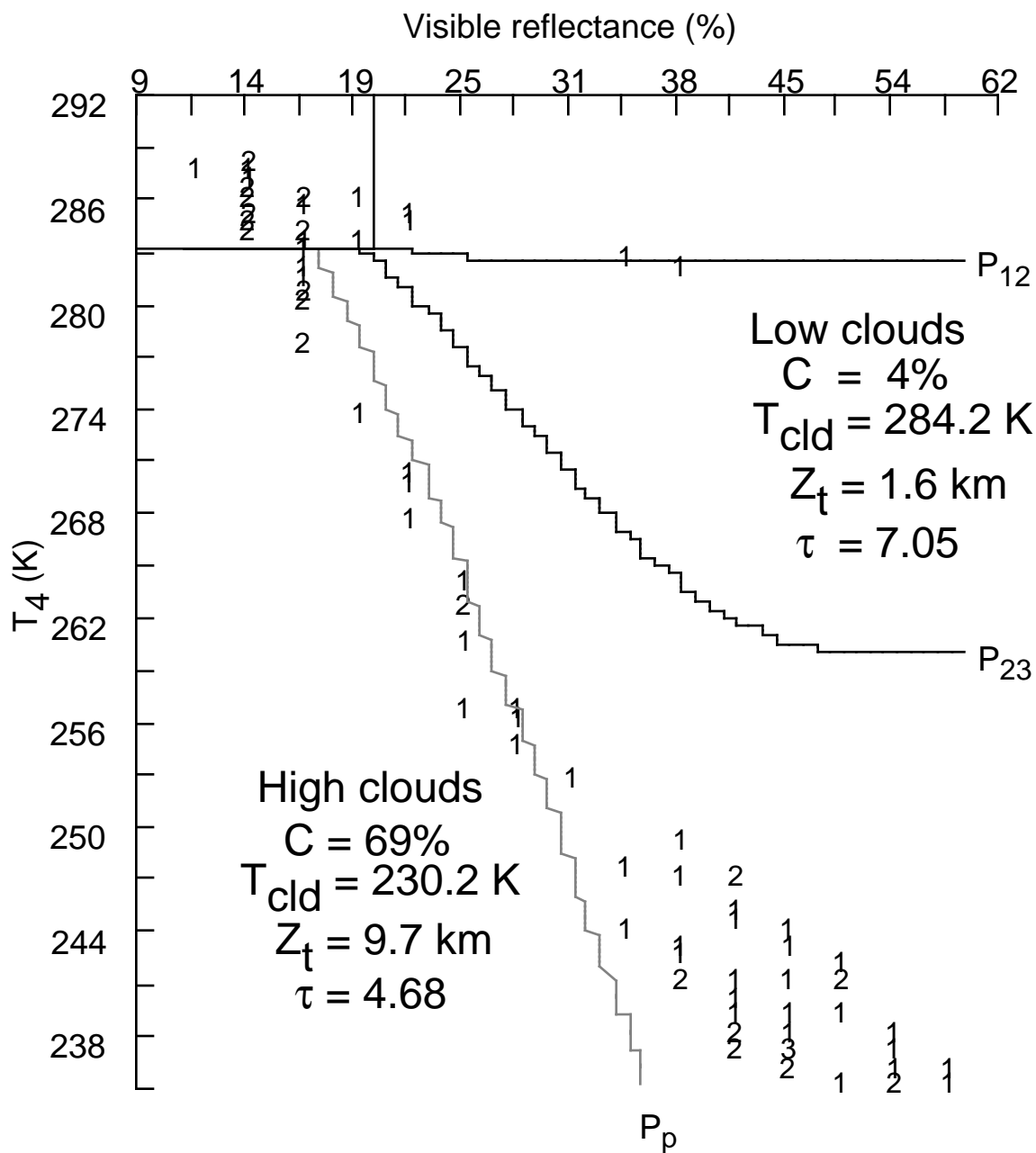
Figure 4.3-11. Concluded.

half-hour-long surface microwave measurement; but it was derived using only four pixels or ~10 minutes. Evaluation of a larger area of nearby low clouds provides a more appropriate comparison because it represents a longer time interval and the scene contains only one cloud layer. The results are  $r_e = 11.9 \mu\text{m}$  and  $W_{liq} = 30 \text{ gm}^{-2}$ . Comparisons of data taken during the FIRE II cirrus experiment found that the satellite-derived particle sizes from this method were within 15% of coincident ground-based, radar-derived ice particle sizes. These initial validations indicate that this technique can yield relatively accurate estimates of particle size and liquid water path.

Another example (Fig. 4.3-14) taken from AVHRR data near Coffeyville shows the difficulties arising from overlapped clouds. Here the retrieval for overlapped cirrus and low stratus yields large water droplets  $r_e = 15 \mu\text{m}$  and clouds at 4.0 km (Fig. 4.3-15(a)) in addition to the high clouds at 7.4 km with  $D_e = 58 \mu\text{m}$  (Fig. 4.3-15(b)). Nearby analyses of single layer stratus and cirrus yielded  $r_e = 10 \mu\text{m}$  and  $D_e = 46 \mu\text{m}$ , respectively. The surface instruments and soundings showed no indication of clouds in the middle layers but did show the two layers. Some of the clouds are apparently nonoverlapped because there are peaks in the size distributions at  $r_e = 10 \mu\text{m}$  (Fig. 4.3-15(a)) and at  $D_e = 40 \mu\text{m}$  (Fig. 4.3-15(b)). The overlapped clouds yield overestimates of particle size. This example shows that without knowledge of the overlap, the method will return errant values of  $T_{cld}$  and  $r_e$  for cases involving an optically thin cirrus over a lower cloud.

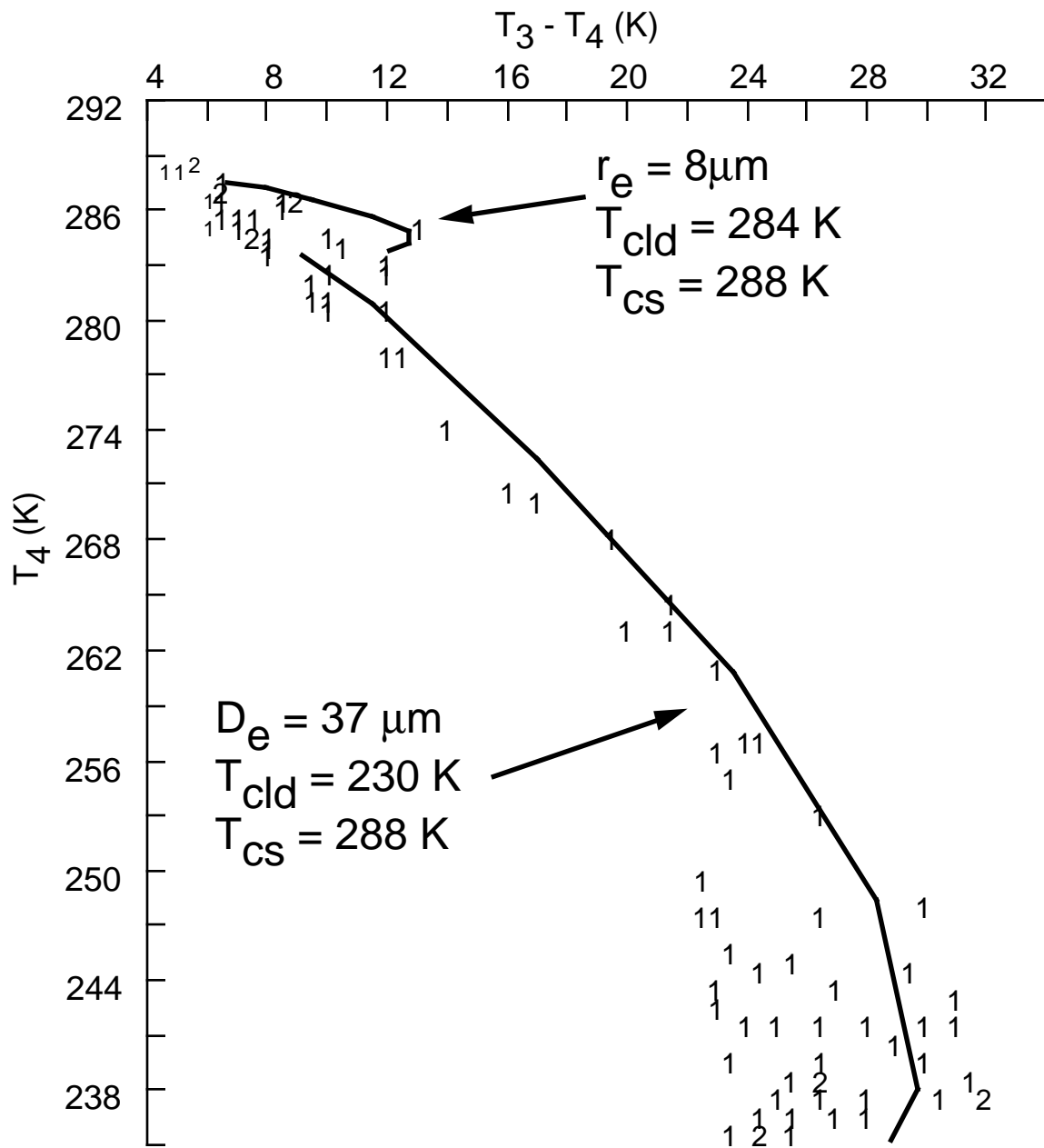
In certain angular configurations and small optical depths ( $\tau < 5$ ), nonmonotonic solutions arise so that a range of particle sizes can be selected by the retrieval depending on the starting effective radius. Figure 4.3-16 demonstrates this behavior for a cloud at 285K over an ocean surface at 290K. The near-forward scattering case (Fig. 4.3-16(a)) shows that  $T_3$  decreases monotonically with  $r_e$  for  $1 < \tau < 8$ . The change with particle size is minimal for  $r_e > 15 \mu\text{m}$  for  $\tau < 4$ . In the near-backscattering case (Fig. 4.3-16(b)),  $T_3$  first increases then decreases at  $r_e = 5 \mu\text{m}$ . For  $\tau = 1$ , two solutions can be obtained for  $r_e$  between 2 and 10  $\mu\text{m}$ . This problem is further illustrated in Figs. 4.3-17 and 4.3-18 which show the full angular range for two measures of the multiple solution problem. The droplet radius  $r_{max}$  having the maximum value of  $T_3$  is plotted for two values of  $\theta_o$  in Figs. 4.3-17(a) and 4.3-17(b) for  $\tau = 1$  and 8, respectively. If the solution is  $r_{max} < 2 \mu\text{m}$ , then no dual solutions are expected. As  $r_{max}$  increases, the range of possible solutions widens as demonstrated in Fig. 4.3-16(b). For a majority of cases,  $r_{max}$  is less than 3  $\mu\text{m}$  for  $\tau = 1$  and equal to 2  $\mu\text{m}$  for  $\tau = 8$ . Most of the larger values of  $r_{max}$  occur in the backscattering portion of the hemisphere and primarily for  $\tau < 8$ . Values of  $r_{max}$  as great as 10  $\mu\text{m}$  occur at  $\theta = 30^\circ$  for  $\theta_o = 32^\circ$  in Fig. 4.3-17(a). That angular configuration is common in the Tropics for Sun-synchronous satellites crossing the Equator during midday. At larger optical depths, the maximum values of  $r_{max}$  are confined to  $\theta > 60^\circ$ . An additional measure of the dual solution possibilities is the range in  $T_3$  for the modeled droplet sizes as shown in Figs. 4.3-18(a) and 4.3-18(b) for the same cases depicted in Fig. 4.3-17. In this situation, as the temperature range decreases, the probability for ambiguous results increases. For  $\tau = 1$  (Fig. 4.3-18(a)), the  $T_3$  range is less than 10K for  $\theta < 30^\circ$ . The minimum values occur along the backscattering direction at  $\theta = 30^\circ$  corresponding to the highest value of  $r_{max}$ . The general pattern for decreased range at smaller viewing zenith angles, however, derives from the smaller reflectances observed near nadir (e.g., Fig. 4.3-6).

One means for solving the dual solution problem for optically thin water clouds is to match the observed  $BTD_{4-5}$  data to parameterized values. This approach is tenable because, at low optical depths, there is a monotonic variation of  $BTD_{4-5}$  with  $T_4$  (e.g., Fig. 4.3-9(a)). Thus, the iteration method using channels 1, 3, and 4 (1-3-4) is repeated with channels 1, 4, and 5 (1-4-5) using the maximum and minimum values of  $T_{cld}$  derived from the initial technique as constraints. The 1-4-5 method is only applicable to optically thin clouds because the information content in  $BTD_{4-5}$  is minimal and ambiguous at larger optical depths. Fortunately, most of the ambiguous 1-3-4 results occur for  $\tau < 6$ . In practice, the 1-3-4 method is always applied. If the selected phase is liquid and  $\tau < 6$ , the final set of 1-3-4 solutions is examined to determine the occurrence of dual solutions in the results. If found, the 1-4-5 technique is



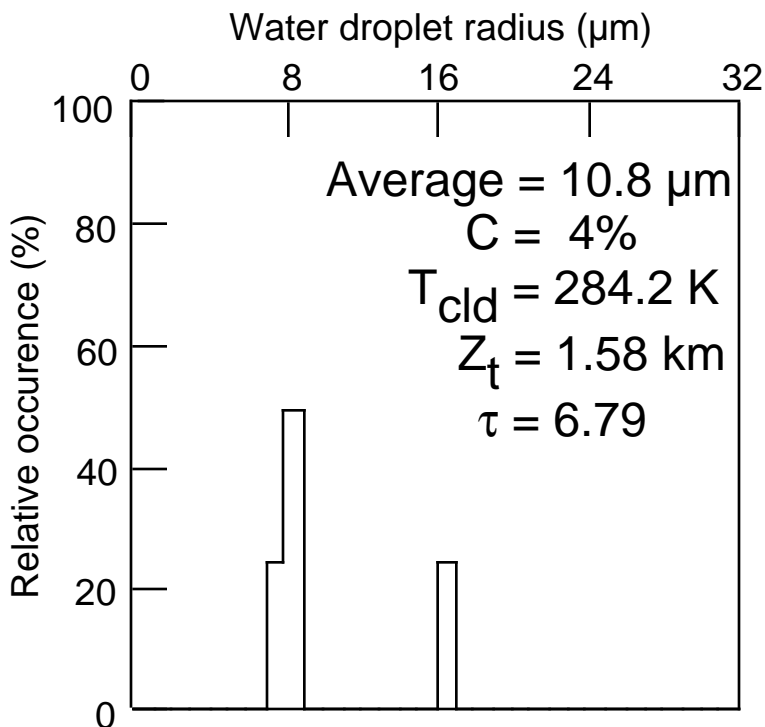
(a) VIS-IR histogram.

Figure 4.3-12. AVHRR histograms over 37.3°N, 95.1°W at 2042 UTC, November 28, 1991.

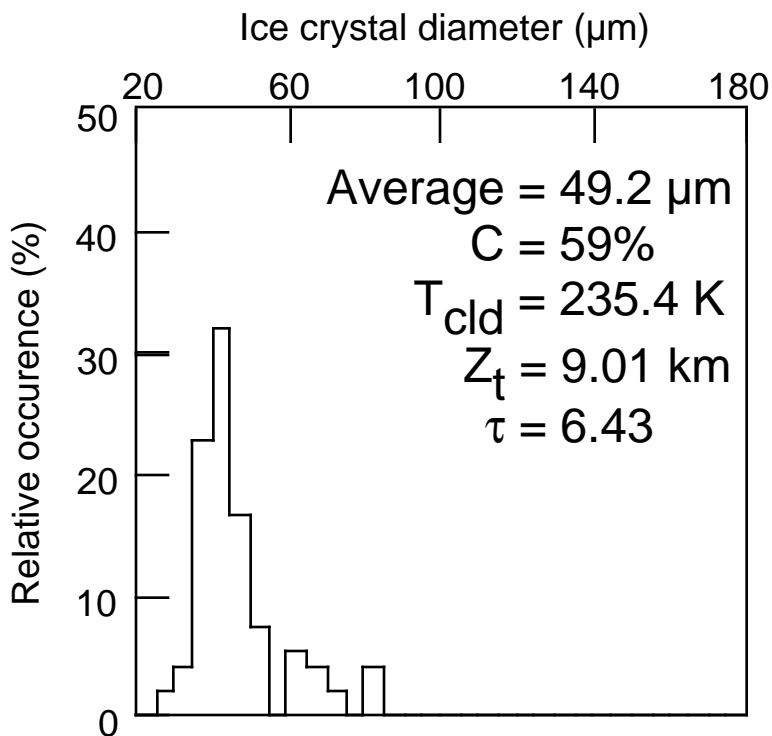


(b) BT-D-IR histogram.

Figure 4.3-12. Concluded.



(a) Water cloud retrieval.



(b) Ice cloud retrieval.

Figure 4.3-13. Retrieval in AVHRR data over 37.3°N, 95.1°W at 2042 UTC, November 28, 1991.

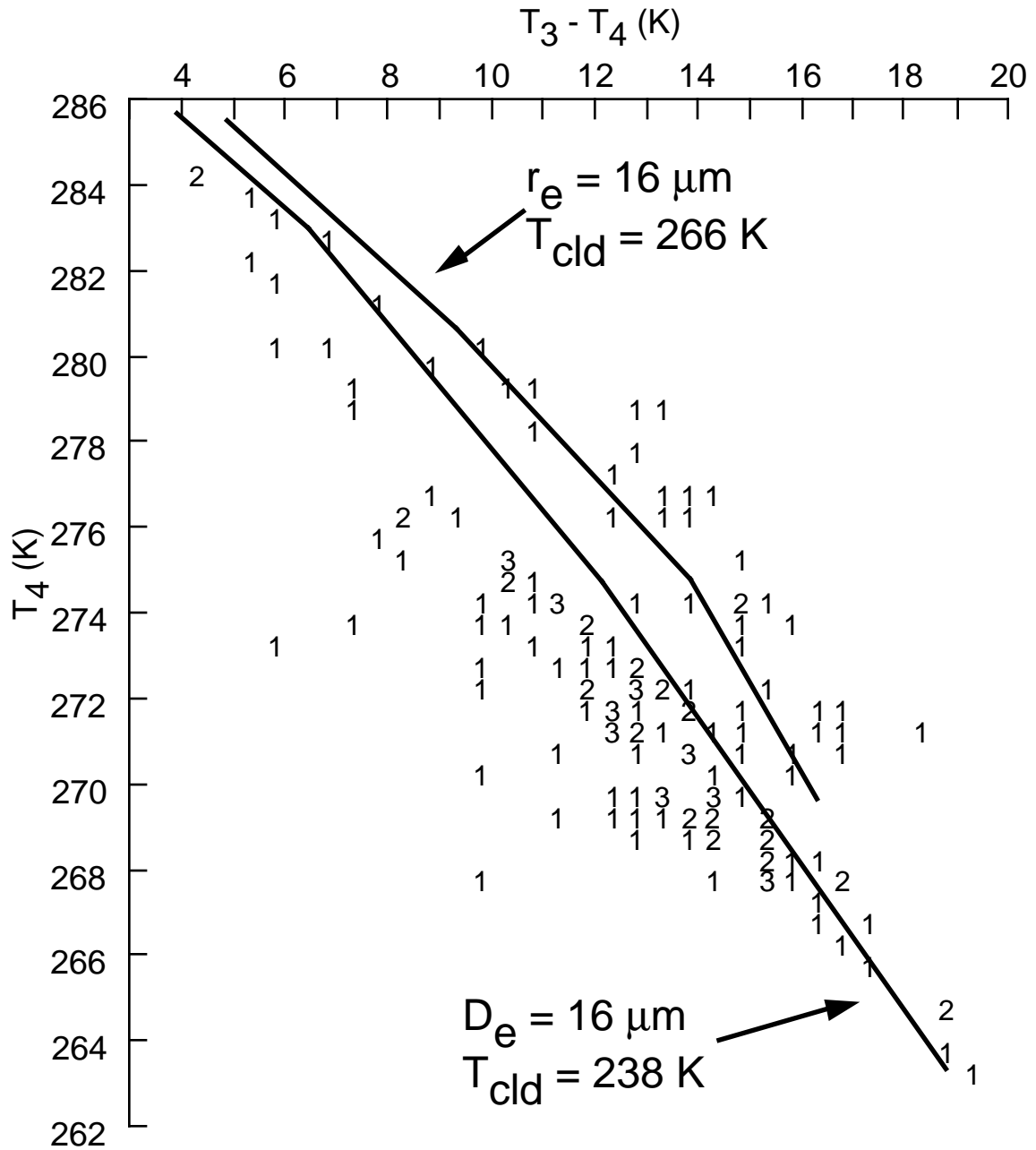
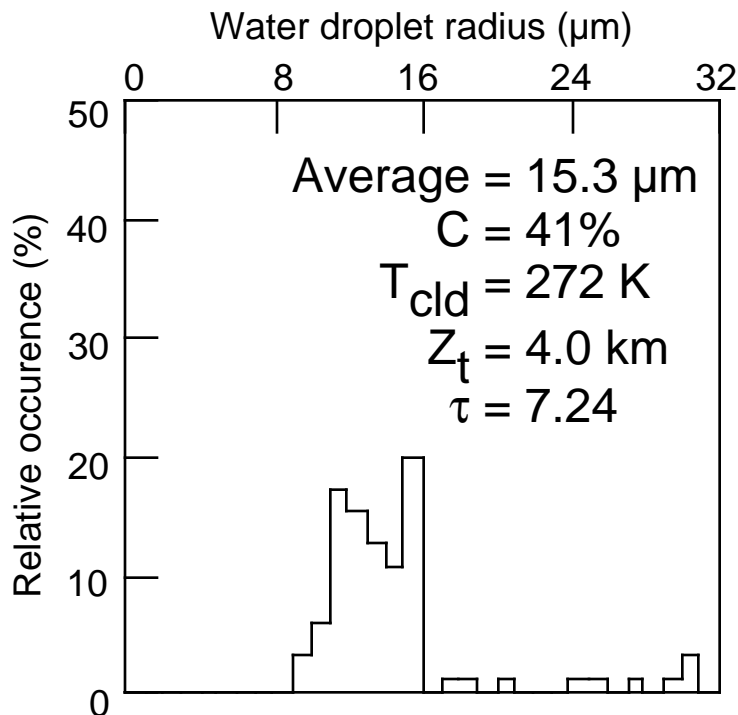
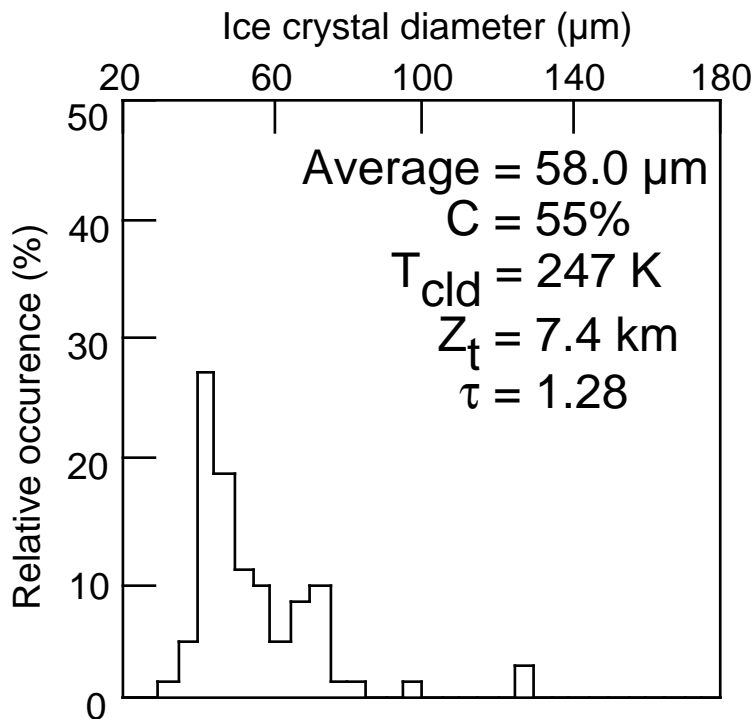


Figure 4.3-14. AVHRR BTD-IR histogram over 37.1°N, 95.6°W at 2036 UTC, November 28, 1991.

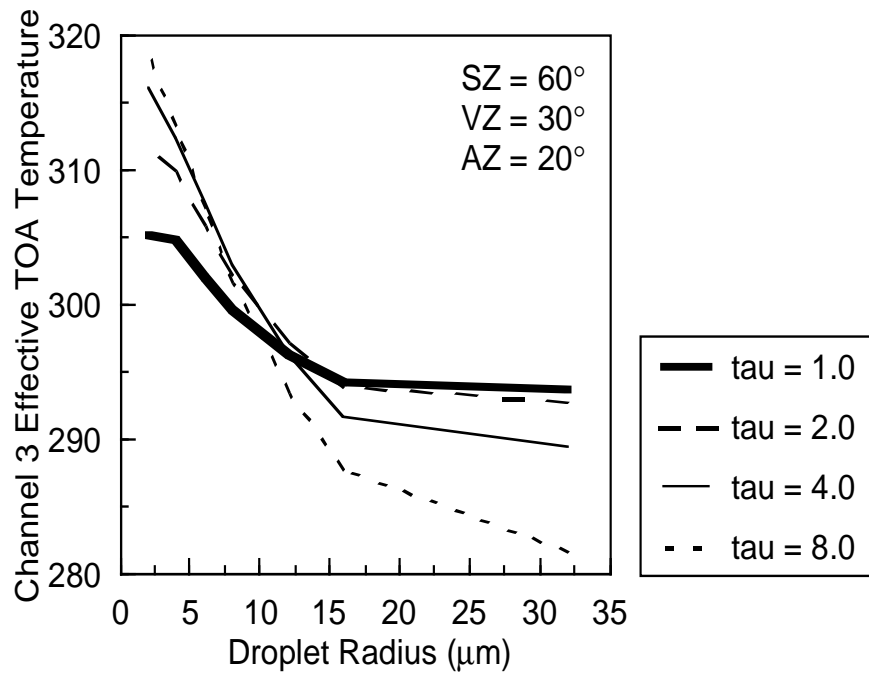


(a) Water cloud retrieval.

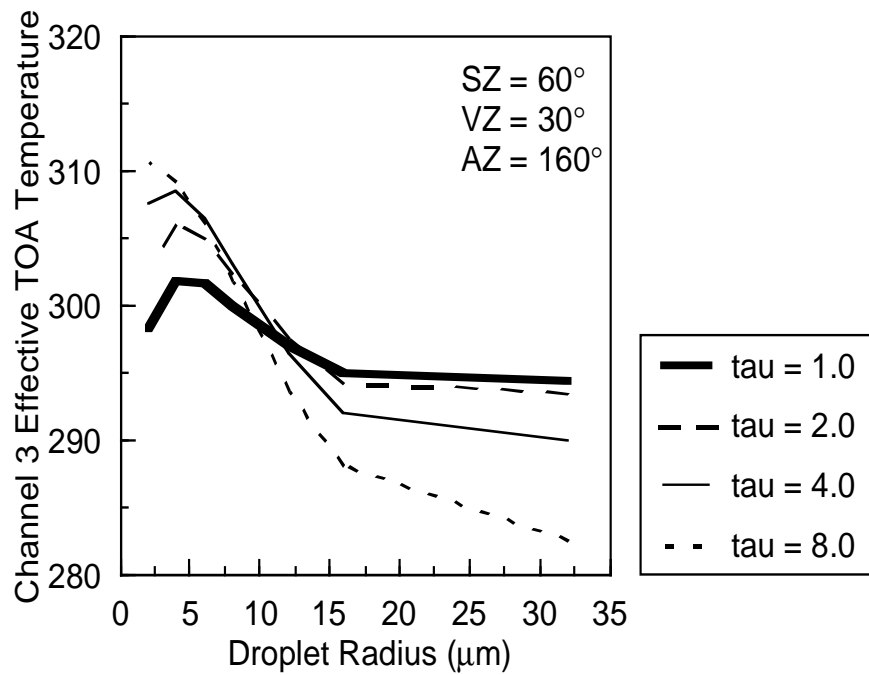


(b) Ice cloud retrieval.

Figure 4.3-15. Retrieval in AVHRR data over 37.1°N, 95.6°W at 2036 UTC, November 28, 1991.



(a) Forward scattering case



(b) Backscattering case

Figure 4.3-16. Droplet size and optical depth dependence of channel 3 effective TOA temperature.

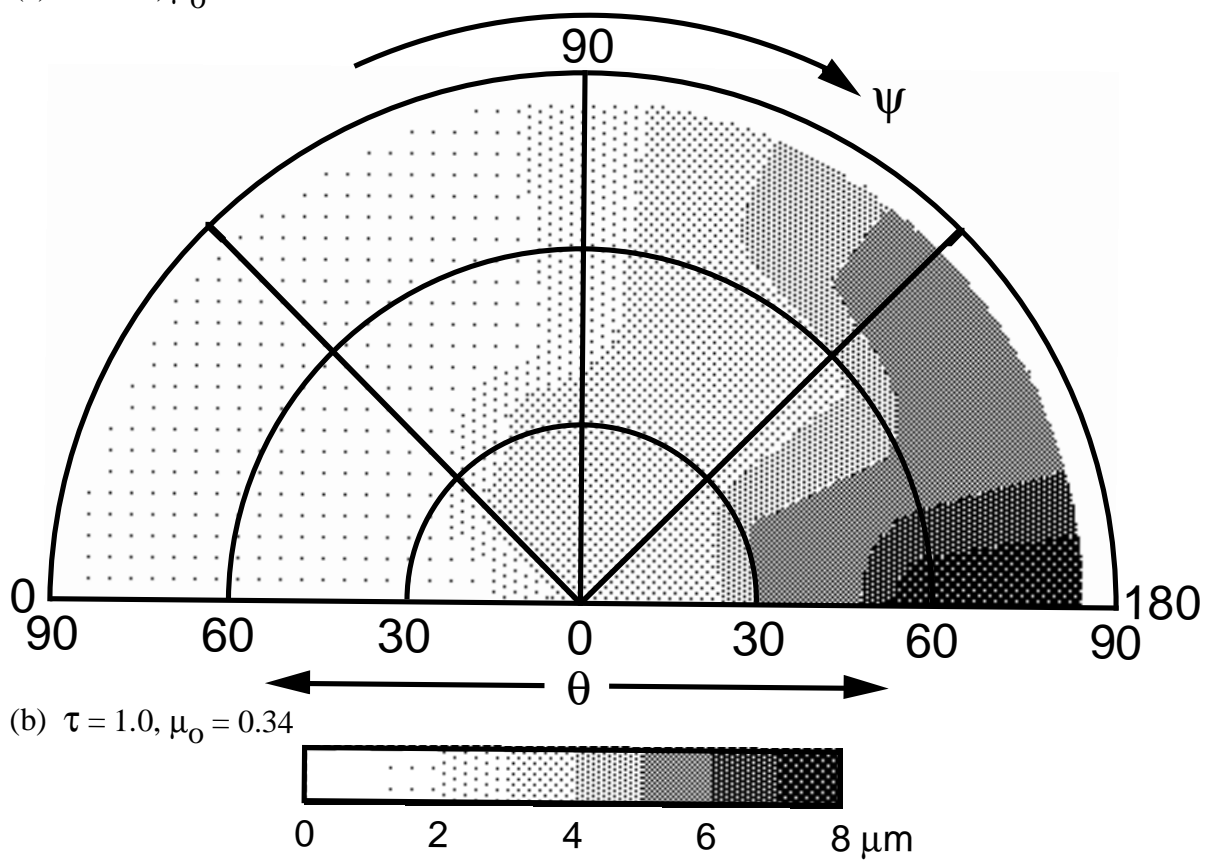
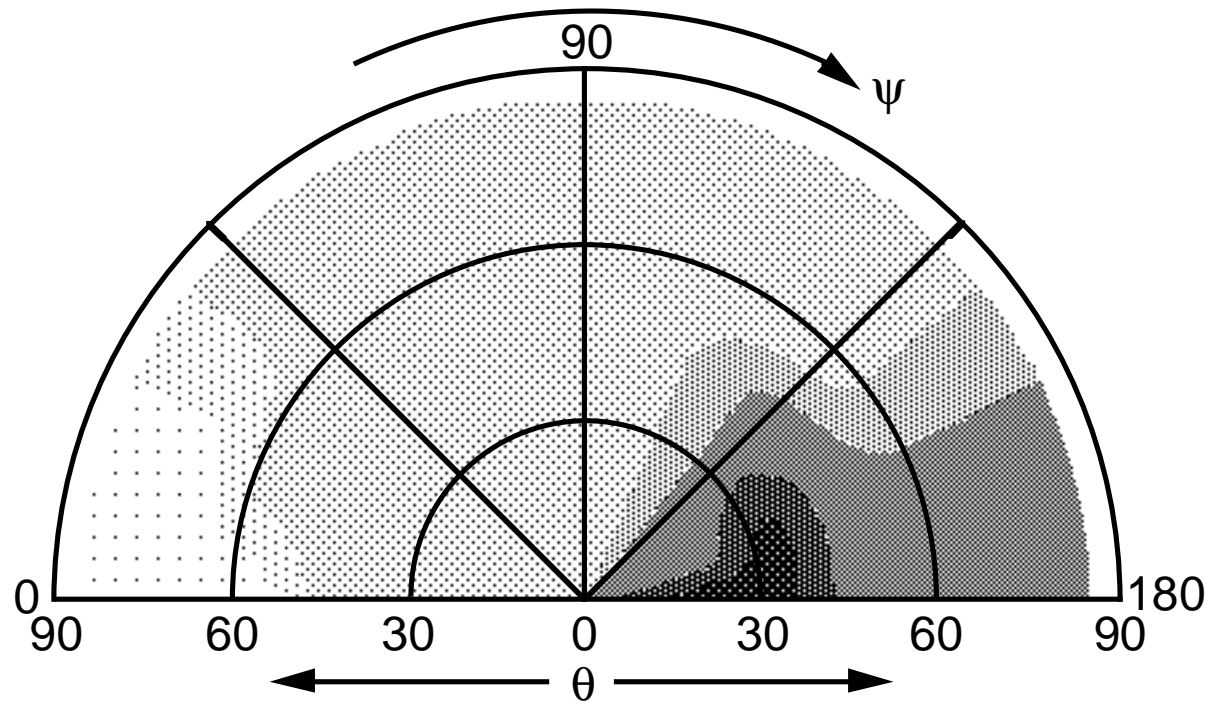


Figure 4.3-17. Angular distribution of VINT dual solutions. Droplet radius with maximum channel 3 radiance.

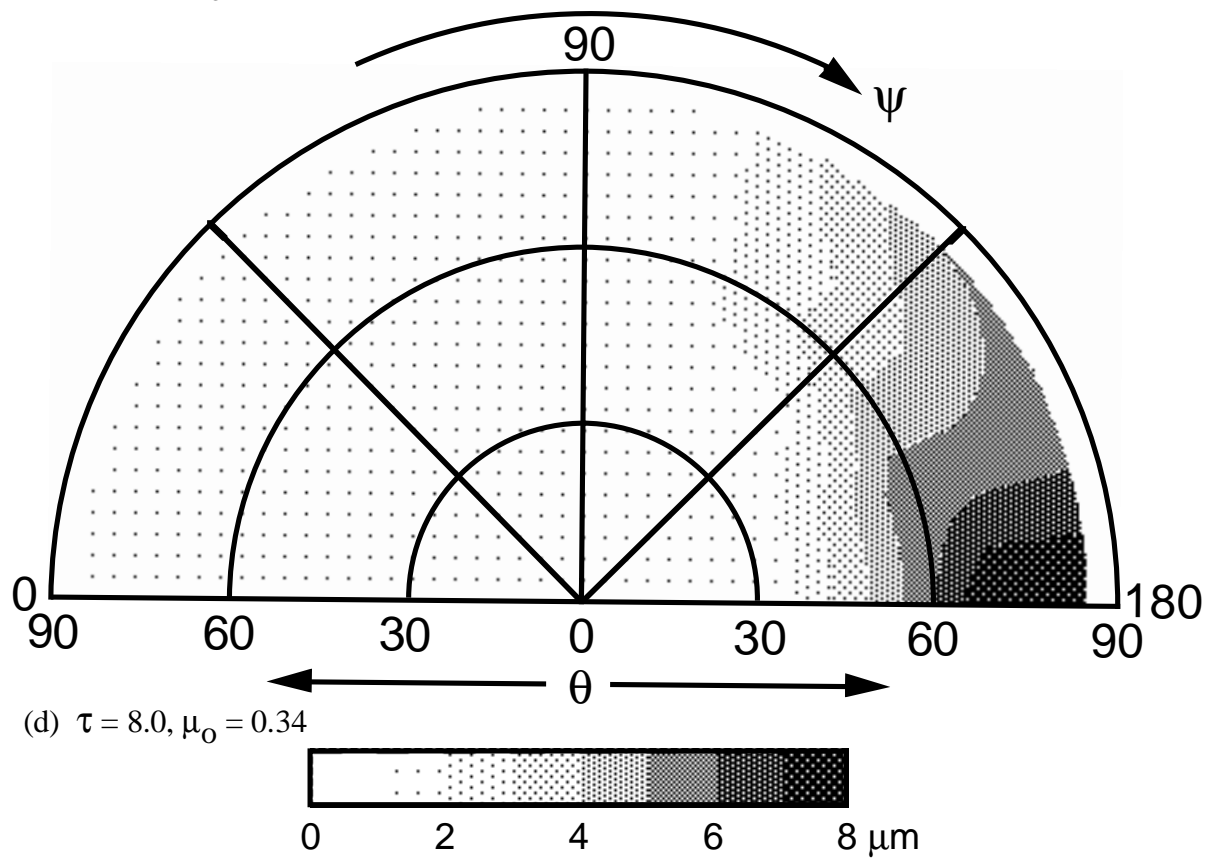
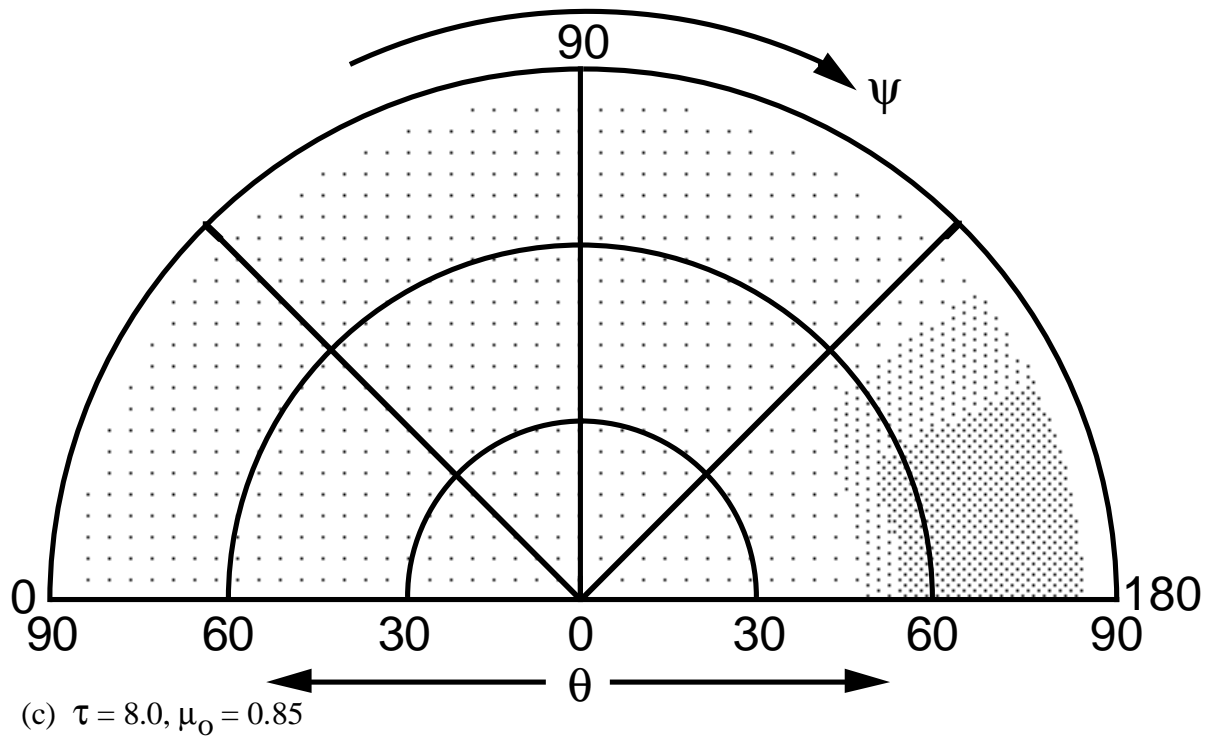


Figure 4.3-17. Concluded.

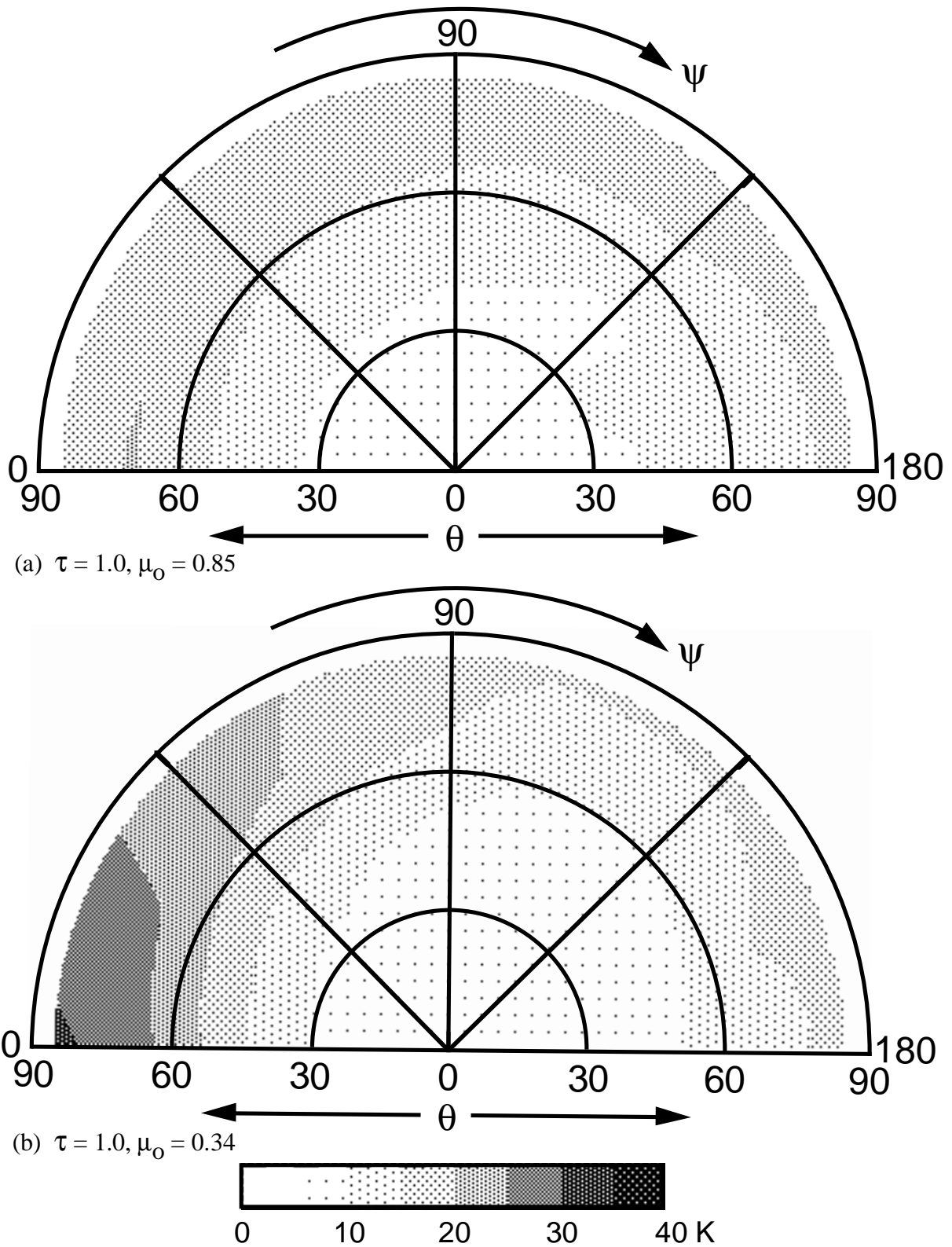


Figure 4.3-18. Angular distribution of VINT dual solutions. Range of channel 3 effective TOA temperatures.

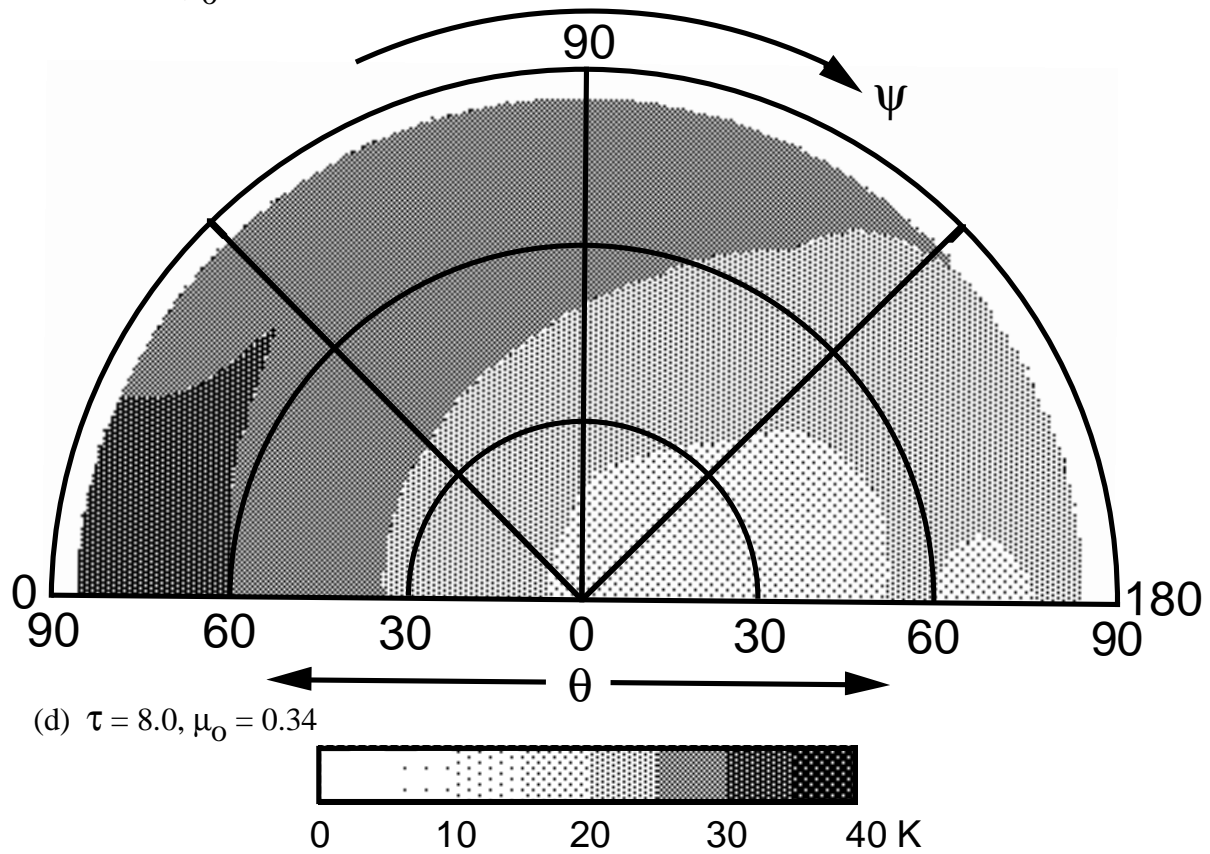
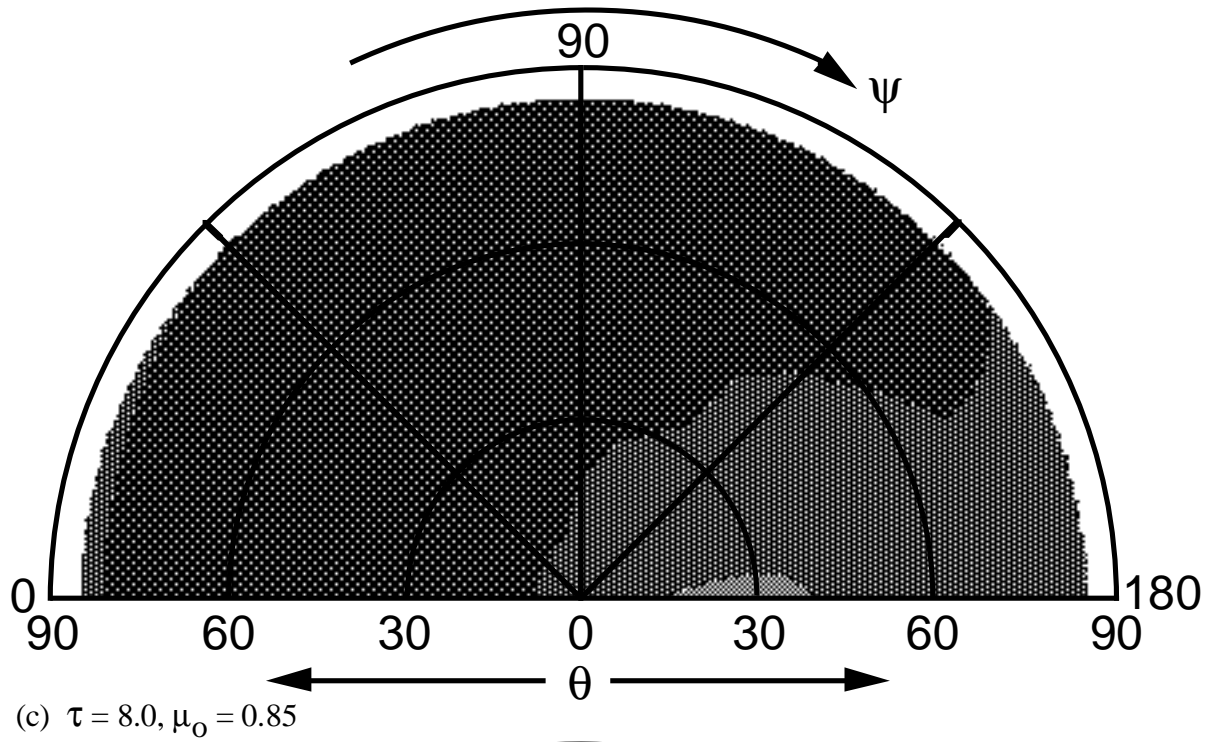


Figure 4.3-18. Concluded.

then applied to the subject pixel to determine final values of  $T_{cld}$ ,  $\tau$ , and  $r_e$  using the range in  $T_{cld}$  from the 1-3-4 results to bound the solution.

A similar approach may be used to identify and account for multilayer clouds in the scene as long as the upper and lower clouds are optically thin and thick, respectively. In such cases, the 1-3-4 method will yield a large optical depth and the derived cloud altitude and effective particle size fall between those of the upper and lower clouds. From a theoretical perspective, the  $BTD_{4.5}$  will differ from that of an optically thick cloud. The lower cloud will act as the background (clear-sky) and the upper cloud will provide the “cloud” signal. If the 1-3-4 result indicates an optically thick cloud, the results can be used to compute  $BTD_{4.5}$  for the same pixel. If the actual  $BTD_{4.5}$  differs significantly from the computed value, it is likely due to the presence of multilayer conditions, especially if previous subsystems have identified two different cloud levels in the tile. If the pixel is identified as being multilayered and a lower cloud temperature is known, the temperature, optical depth, and particle size of the upper cloud can be computed using only the  $BTD_{4.5}$  part of the nighttime method described in section 4.3.4.2.

**4.3.4.1.2. Reflectance technique.** The reflectance approach uses the ratio  $\rho_{0.65}/\rho_{1.60}$  to determine the phase of the clouds by comparing the ratio to model calculations for thick ice and water droplet clouds. For each single-layer pixel, the phase will be determined by comparing the reflectance ratio to an ice-water threshold computed for  $\mu_o$ ,  $\mu$ , and  $\phi$  using the models discussed earlier. If the ratio exceeds the greatest model ice ratio, the cloud will be designated as liquid water; otherwise, the phase is ice.

After determination of the phase, a least squares approach is applied to match the multispectral radiances to a set of model calculations simulating the reflectances for clouds having a range of particle sizes and optical depths. This approach, the models to apply it, the expected errors, and current limitations are discussed in detail by King and Tsay (1993). This technique will use the VIRS 0.65-, 3.75-, and 1.60- $\mu\text{m}$  data during CERES/TRMM. It is anticipated that CERES/EOS will use the 3-channel reflectance method employing the 2.13- $\mu\text{m}$  MODIS channel. In this Release 2 software design for the COPRS, the reflectance method serves as the secondary particle size retrieval method. The four-channel method will serve as the primary technique because of its history of global application using operational satellite data. The reflectance method will be phased in as experience with its use in satellite retrievals is gained.

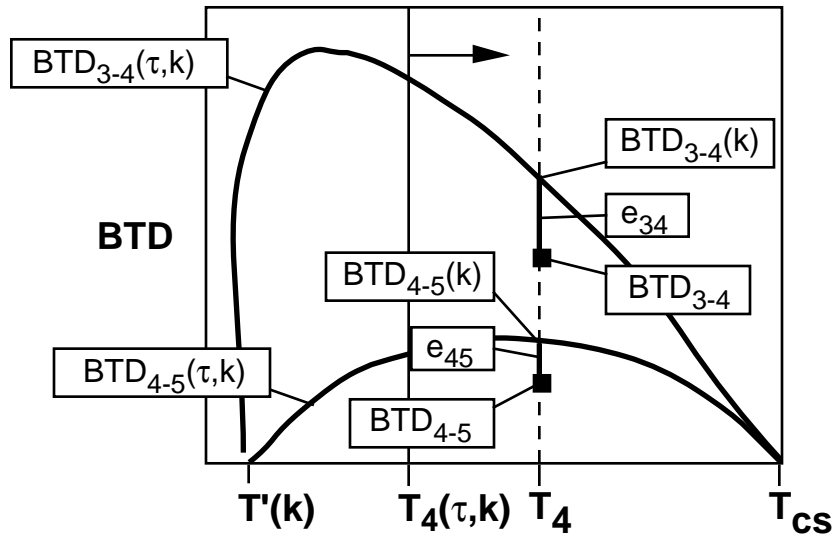
#### 4.3.4.2. Nighttime Cloud Optical Depth, Particle Size, and Cloud Temperature

The cumulative experience of remotely sensing particle size and optical depth at night is much less than that for the daytime. The available techniques are either in early development or in a conceptual stage at this time. The primary shortcoming to the nocturnal methods is the lack of a relatively independent optical depth channel. When the sun is shining, it is usually possible to obtain a close approximation of optical depth using the visible channel because of its relative insensitivity to particle size (Fig. 4.3-6) and its independence from  $T_{cld}$ . This facilitates the determination of  $T_{cld}$  and, ultimately,  $r_e$ . At night, the problem is less tractable because all three channels are highly sensitive to  $T_{cld}$  and  $\tau$  for small optical depths ( $\tau < 6$ ). Although  $T_{cld}$  is well defined for larger optical depths, there is minimal information available regarding  $\tau$  and  $r_e$ . For those clouds having small optical depths, particle size and  $\tau$  can be determined using one of the approaches described below.

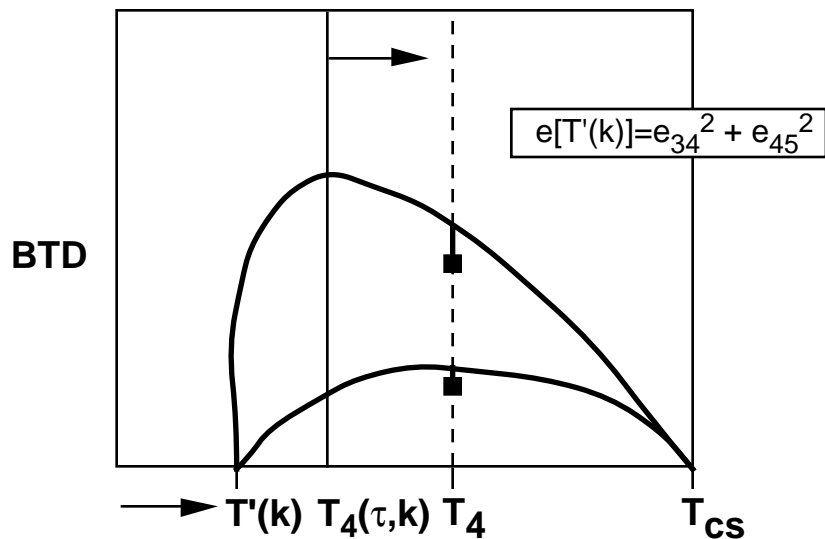
**4.3.4.2.1. Solar-infrared, infrared, split-window technique (SIST).** Given an optically thin cloud ( $\tau < 6$ ),  $\mu$ , and the background (clear-sky or cloudy) temperatures for channels 3, 4, and 5, it is assumed that a given pair of  $BTD_{3-4}$  and  $BTD_{4-5}$  at a particular value of  $T_4$  uniquely define a cloud characterized by  $T_{cld}$ ,  $r_e$  or  $D_e$ , and  $\tau$ . These parameters can be determined by matching the three measured quantities as closely as possible to the same parameters calculated using each of the microphysical models defined for the COPRS. Each observed quantity will fall between the corresponding pair of discrete theoretical calculations for a given phase. The distance in  $BTD$  from the model value to the observed value is used

to interpolate between each model for each parameter to assign a value of cloud temperature, optical depth, and particle size to the pixel for both channels 3 and 5. In the absence of temperature indications, the phase is selected based on how closely the channel 3 and 5 parameters agree with each other. The final values of  $T_{cloud}$ ,  $r_e$  or  $D_e$ , and  $\tau$  are determined by averaging the channels 3 and 5 results for the selected phase.

This technique attempts to determine  $\tau$ ,  $T_{cloud}$ , and particle size through an iterative process that minimizes the differences between model-derived and observed values of  $BTD_{3-4}$  and  $BTD_{4-5}$  for the observed  $T_4$ . This procedure, illustrated schematically in Figure 4.3-19, begins with values given for  $\mu$



(a) First step of iteration process; compute errors for model k using first guess temperature.



(b) Second step of iteration process; compute errors for second cloud-temperature guess.

Figure 4.3-19. Schematic illustration of emittance iteration process for nighttime cloud property retrievals. June 2, 1997

and  $T_{cs}$  and assumes an initial value of  $T_{cld} = T'(k)$ , where  $T'(k) < T_4$  and  $k$  is an emittance model index corresponding to a particular particle size and phase. The tropopause temperature is the initial value of  $T_{cld}$  unless the layer analysis (section 4.2.) indicates only a single layer is present or  $BTD_{3-4} < BTD_{3-4cs}$ . In the former case, the initial cloud temperature is the layer temperature minus 5 K. If  $BTD_{3-4} < BTD_{3-4cs}$ , the starting temperature is  $T_4 - 5$  K. For each of the channel-4 emittance models (4.3-8),  $\tau[T'(k), k]$  is determined using a secant iteration method to match  $T_4$ . This process is represented by the arrow in Figure 4.3-19(a). The resulting value of  $\tau$  is used to compute  $T_3$  and  $T_5$  using the channels 3 and 5 emittance models in (4.3-4). The model values of  $BTD_{3-4}[T'(k), k]$  and  $BTD_{4-5}[T'(k), k]$ , shown as the intersections of the model curves and the dashed line in Figure 4.3-15(a), are calculated from the model-derived temperatures and the observed  $T_4$ . Difference errors,  $e_{34} = BTD_{3-4} - BTD_{3-4}[T'(k), k]$  and  $e_{45} = BTD_{4-5} - BTD_{4-5}[T'(k), k]$ , are computed for each model. A composite error,

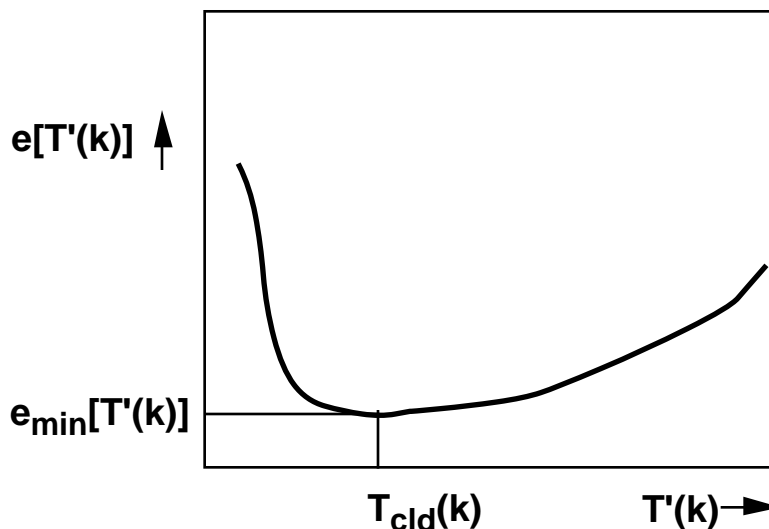
$$e[T'(k), k] = e_{34}^2 + e_{45}^2 \quad (4.3-14)$$

becomes the parameter to minimize. These operations are repeated varying  $T'(k)$  as illustrated in Figure 4.3-19(b) until  $e(T_{new}, r_e)$  is minimized yielding the best estimate of cloud temperature for model  $k$ . In the first iteration,  $T'(k)$  is increased by 10 K for each step until  $e$  begins to increase. Figure 4.3-20(a) depicts how  $e$  can vary with increasing  $T'(k)$ . Subsequent iterations repeat the error calculations using increasingly smaller temperature increments bounded by the last two temperatures used in the preceding iteration. The iterations continue until the increment is less than 0.1 K. For the case in Figure 4.3-20(a), the value of  $T_{cld}(k)$  corresponds to the minimum error. This entire procedure is repeated again for each model producing final values of  $e[T'(k), k]$  as shown in Figure 4.3-20(b). In practice, the algorithm begins with the smallest model for the phase and continues until  $e_{34}$  and  $e_{45}$  switch signs. The sign change in these error values indicates that the observation is between the last two models. One of the two models,  $k_{min1}$ , will have the smallest value of  $e$  for the particular phase, while the other model,  $k_{min2}$ , should also have a relatively low error. These two models are then selected for interpolation. If  $T_{cld} > 273$  K, only the water-droplet models are used. Conversely, if  $T_{cld} < 233$  K, only the ice-crystal models are considered further.

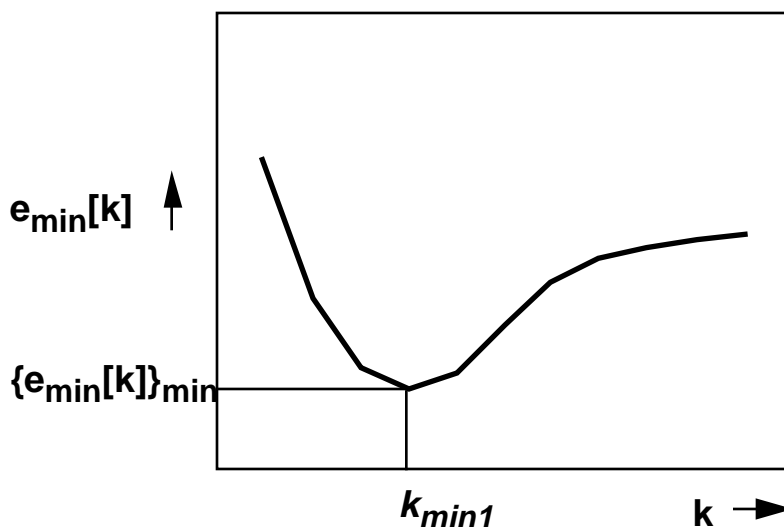
Final values of  $r_e$  or  $D_e$ ,  $T_{cld}$ , and  $\tau$  are computed for channel 3 by linearly interpolating between  $r_e(k_{min1})$  and  $r_e(k_{min2})$ ,  $T_{cld}(k_{min1})$  and  $T_{cld}(k_{min2})$ , and  $\tau(k_{min1})$  and  $\tau(k_{min2})$ , respectively, using  $e_{34}[T'(k_{min1}), k_{min1}]$  and  $e_{34}[T'(k_{min2}), k_{min2}]$  as the independent variables. The same interpolation is repeated for channel 5. The resultant values for the two channels are averaged to obtain the best estimate of each parameter. If both phases are considered, then the results for the phase having the smallest uncertainty,

$$e_{35} = \left( \frac{T_{cld3} - T_{cld5}}{T_{cld3}} \right)^2 + \left( \frac{\tau_3 - \tau_5}{\tau_3} \right)^2 + \left( \frac{r_{e3} - r_{e5}}{r_{e3}} \right)^2 \quad (4.3-15)$$

are selected for the final parameter values. The subscripts 3 and 5 refer to the parameter values derived using channel 4 with channels 3 and 5, respectively. Because of different sensitivities of the various channels to changes in  $r_e$ , it may be necessary to weight the terms in (4.3-13) by values other than unity. Additional research is needed to examine potential weighting changes. The most accurate estimates of



(a) Determination of the minimum error in a given particle size model.



(b) Determination of model having minimum error.

Figure 4.3-20. Schematic diagram of minimum error estimation to determine most appropriate particle size models.

$T_{\text{cld}}$  are obtained for the larger optical depths ( $\tau > 6$ ), while the most accurate values of  $\tau$  and  $r_e$  should occur for ( $1 < \tau < 6$ ). There is little variation in *BTD* with particle size for small and large optical depths.

The SIST was tested using a limited set of simulated data with superimposed noise. In these cases, the retrieved particle sizes were within  $0.1 \mu\text{m}$  of the simulated cloud values and the phase was chosen correctly. However, it can be sensitive to the clear-sky temperature which is not as accurately determined at night, especially over land surfaces, as during the daytime. The small variation in *BTD* at the small and large values of  $\tau$  also increases the sensitivity of the retrieval. Considering these factors and the inherent instrument noise, it is possible to obtain unrealistic results in some scenes, particularly over

land where  $T_{cs}$  can vary rapidly with geography. To minimize the occurrence of such cases, the data in a tile can be treated aggregately by assuming that they belong to the same cloud layer. Thus, the tile-mean value of  $T_{cs}$  can be used to obtain a value of  $T_{cld}$  for the tile using least squares regression. As in the single pixel approach, both ice and water models are tested and the phase is selected based on the smallest standard error of the regression estimate. Particle size is then determined for each pixel using the regression-derived value of  $T_{cld}$ .

The SIST regression technique was applied to a set of 4-km GOES-8 data taken during 1995 and 1996 covering a 30 km x 30 km box over the ARM Central Facility. GOES-8 has channels similar to the AVHRR channels 1,3, 4, and 5. A micropulse lidar (MPL) dataset (available on the Internet at <http://viri.gsfc.nasa.gov/mpl.html>) depicting cloud structure directly over the ARM facility was used as the altitude reference for the retrievals. Figure 4.3-21 shows the results for data taken at 0245 UTC April

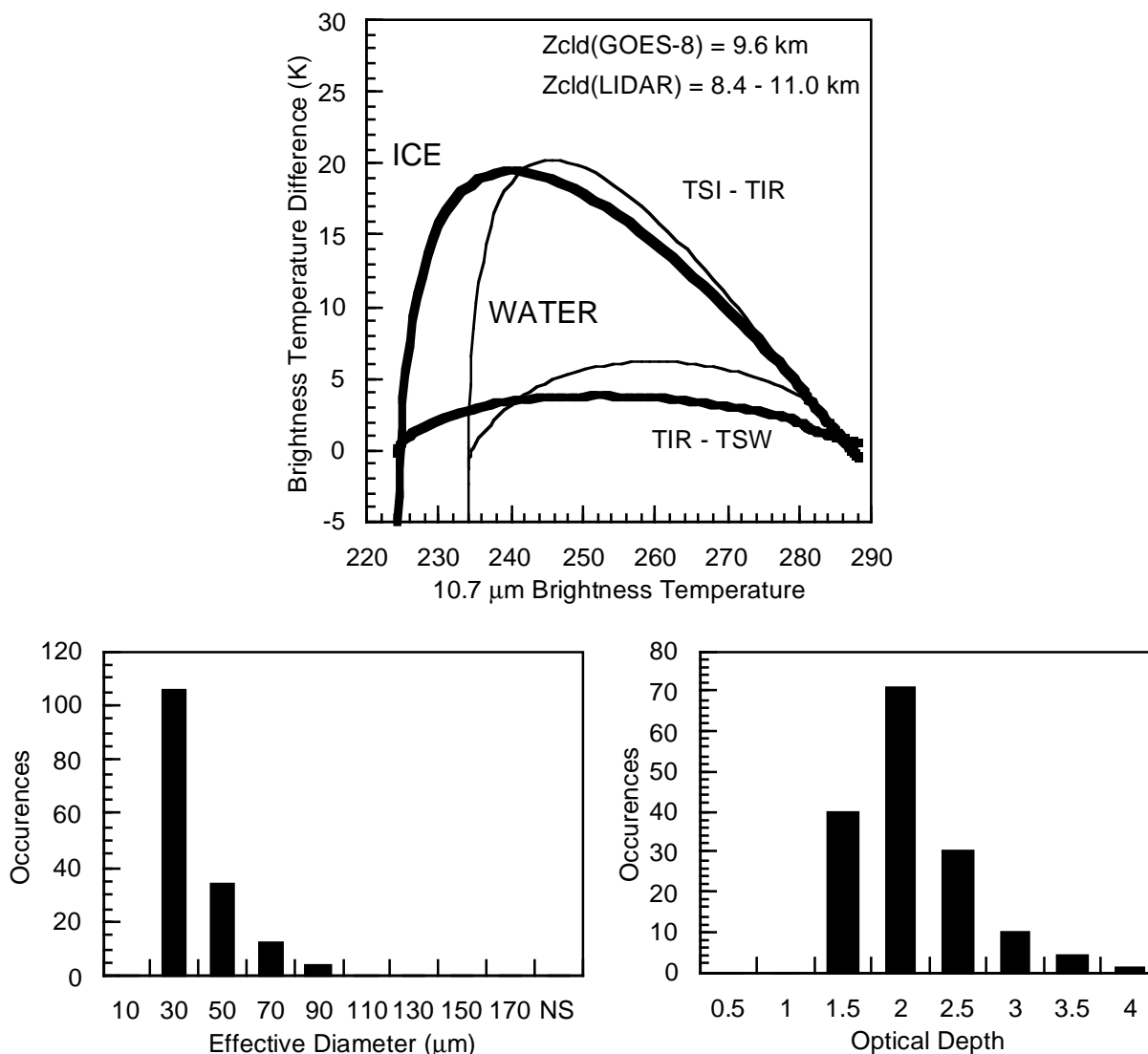


Figure 4.3-21. 3-channel night-time retrieval; 0245 UTC April 15, 1995; 36.61N 97.49W.

15, 1995 with a cirrus cloud between 8.4 and 11 km according to the MPL. In this case, the ice model provides the best fit to the data yielding  $T_{cld} = 225.3$  K which corresponds to an altitude of 9.6 km. The optical depths vary from 1.5 to 4 and mean value of  $D_e \sim 40$   $\mu\text{m}$ . Figure 4.3-22 shows the results for all

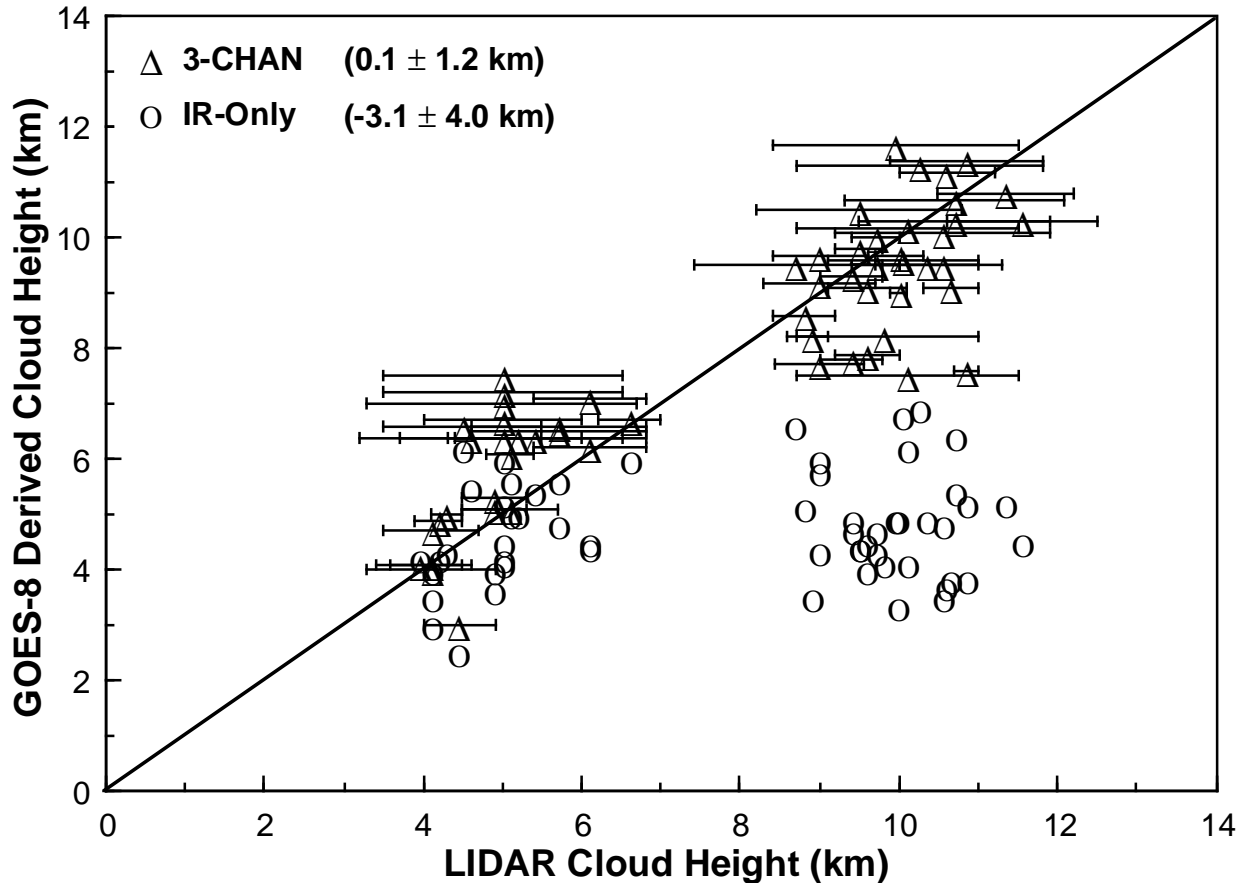


Figure 4.3-22. Satellite-derived and Lidar-derived cloud heights at night.

of the cases used in the testing of the method together with those using an IR-only technique that assumes that all of the clouds are optically thick. The mean altitude error for the 3-channel method is  $0.1 \pm 1.2$  km compared to  $-3.1 \pm 4.0$  km for the IR-only method. Thus, the SIST has significantly improved the height determination for the single layer cases.

Although the mean cloud altitudes are more accurately determined with the SIST regression analysis, it is often not possible to derive a particle size for many of the pixels. This problem most likely arises from the assumption of single values of  $T_{cs}$  and  $T_{cld}$  for the tile. While the value of  $T_{cs}$  cannot be determined for each pixel, it is possible to obtain more values of  $T_{cld}$  using the NS pixels. The initial regression and pixel analyses presumably yields values of  $D_e$  for many of the pixels actually containing a cloud near the derived value of  $T_{cld}$ . It will not be possible to determine a value of  $D_e$  if the true cloud temperature differs too much from the regression value. To account for those pixels, the regression analysis is performed at least two additional times: once using the pixels having  $BTD(T_4)$  values greater than the regression values (or  $T_4 < T_{cld}$ ) and once using the remaining NS pixels. The new value of  $T_{cld}$  for the tile is recomputed using the weighted means from all of the regressions. Similarly, the mean value of

$D_e$  is computed using all of the pixels with a valid solution. Any remaining pixels are assigned the mean particle size for the tile. Testing of the SIST is continuing.

**4.3.4.2.2. Single-layer, fixed-size technique.** An alternate method that may be included in the COPRS is the technique of Lin and Coakley (1993) that interprets the pixel radiances for a single-layer cloud deck as

$$B(T) = (1 - C)B(T_{cs}) + C(\epsilon B(T_{cl}) + tB(T_{cs})) \quad (4.3-16)$$

where wavelength is implied and  $C$  and  $\epsilon$  are the pixel-scale fractional cloud cover and cloud emittance, respectively. The cloud temperature and particle size index are determined iteratively from the group of pixels constituting the cloud deck. The emittance models described earlier will be used to determine particle size and phase. A single cloud temperature and effective radius are assumed for the entire deck. Those two parameters define a set of solutions to (4.3-16) that envelope most of the pixels representing the cloud deck. The emittance and cloud fraction for each pixel within the envelope are obtained through simultaneous solution of (4.3-16) for channels 4 and 5. Details of this method are given by Lin and Coakley (1993).

This technique is limited to those conditions where a single layer is easily discernible. It allows no variation of particle size and radiating temperature within the deck. The particle size derived for the deck tends to be the smallest observable particle size for the given set of pixels because it is defined by those pixels essentially having the greatest  $BTD_{4-5}$  for a given  $T_4$ . The cloud temperature also tends to be the coldest observed brightness temperature. This method, however, requires no iteration and is relatively simple to implement. Refinement of the technique is continuing.

#### 4.3.4.3. Multiple Cloud Layer Retrievals

The discussion above generally applies to single layer clouds or to overlapped clouds that include an optically thick upper cloud layer. In either case, the pixel index will probably denote a single layer cloud. For data blocks with multiple cloud layer pixels, a slightly different approach is taken. The first step for a given data block is to determine the particle sizes for all of the single-layer pixels. When available, the mean particle sizes and temperatures are computed for each layer. If single-layer particle size is not available, only the layer temperatures are available from the subsystem input dataset. Two approaches are taken for these cases.

When the layer temperatures and particle sizes are available, optical depth is the remaining unknown quantity if the background temperature is specified. In the case of multiple layers, the background temperature may vary with the emittance or optical depth of the lower cloud. The range of the background temperature is simply  $T_{cs} - T_{lc}$ , where  $T_{lc}$  is the lower-cloud temperature. An envelope of  $T_4$  and  $BTD_{3-4}$  can be constructed using the upper cloud temperature  $T_{uc}$  as  $T_{cl}$ , and  $T_{lc}$  and  $T_{cs}$  as the temperatures used to compute the clear radiance term in (4.3-4) and (4.3-9). Multilevel pixels falling outside this envelope will be treated as single-layer pixels and the particle size and cloud temperature retrieval will be executed in the normal fashion. Those pixels with values within the envelope will be analyzed for particle size and background or "clear-sky" temperature. The initial background temperature is found by linear interpolation between the lower and upper bounds of  $BTD_{3-4}$  at the observed  $T_4$ . The optical depth of the upper cloud is found using (4.3-4). The final values of the lower and upper cloud optical depths are found by iterating this process. The mean particle sizes and temperatures for the upper and lower clouds are assigned to all of the pixels in the envelope.

When layer temperatures are the only parameters available, it is assumed that the lower cloud is optically thick so that  $T_{lc}$  is the only value substituting for  $T_{cs}$ . The SIST is then applied to find optical depth and cloud particle size. If particle sizes can be retrieved, they are used to compute mean values for the upper layer. The first approach is then invoked for the remaining pixels if they are available. If no

particle sizes are retrieved, the particle size is specified using default values for water and ice. Optical depths are then computed using the visible reflectance. A technique for using the MODIS 1.38- $\mu\text{m}$  channel will also be explored for estimating the high cloud optical depth. The methods for processing multilayer pixels are in the development stage. The techniques currently available for deriving multilayer cloud properties are not sufficiently mature to be applied to the CERES imager data in this algorithm release. Additional research will be devoted to the developing the multilayer retrievals as operational algorithms in future releases of the COPRS software.

#### 4.3.4.4. Water Path

Rearranging (4.3-7) gives the liquid water path,

$$W_{liq} = \frac{4\delta_{liq}r_e\tau}{3Q_e} \quad (4.3-17)$$

for a given effective droplet radius and optical depth. Using the model distributions in (4.3-13) in a regression fit yields the ice water path ( $\text{gm}^{-2}$ ),

$$W_{ice} = \tau (0.259 D_e + 0.000819 D_e^2 - 0.88 \times 10^{-6} D_e^3) \quad (4.3-18)$$

for the retrieved ice-crystal size and optical depth.

#### 4.3.4.5. Cloud Top and Base Altitudes

Cloud-top height  $Z_t$  is the lowest altitude from the sounding corresponding to  $T_{cld}$ . Because the value of  $T_{cld}$  may correspond more closely to the center of the cloud in optically thin cases, it will be adjusted in some cases to account for semitransparency. The adjustment uses the approach of Minnis et al. (1990a) for cirrus clouds. The channel-4 cloud-top emittance is defined as

$$\epsilon_t = \epsilon_4(2.97 - 0.00914T_{cld}) \quad (4.3-19)$$

The cloud-top temperature  $T_t$  is computed using the observed value of  $T_4$  and  $T_{cs4}$  in (4.3-4). This approach is used only for  $T_{cld} < 253$  K. For warmer clouds,  $\epsilon_t = 0.98\epsilon_4$ . No adjustment is made for water clouds because the correction is usually less than 0.1 km, the precision of the height determination. Cloud base is given as  $Z_b = Z_t - \Delta Z$ . The cloud thickness  $\Delta Z$  is computed using empirical formulae. For clouds below 4 km,  $\Delta Z = 0.08\tau^{1/2} - 0.04$  (Minnis et al. 1992). When  $\Delta Z < 0.02$  km,  $\Delta Z$  is set to 0.02 km. For other clouds,

$$\Delta Z = 7.5 - 0.026T_c + 0.85 \ln \tau \quad (4.3-20)$$

(Smith et al. 1993). The minimum thickness for these clouds is also 0.02 km, with a maximum of 8 km. Cloud base and top pressures correspond to  $Z_b$  and  $Z_t$  in the vertical profiles of  $Z(p)$  and  $T(p)$ .

### 4.3.5. Practical Considerations

#### 4.3.5.1. Computer Requirements

**4.3.5.1.1. Model input.** The bidirectional reflectance models have been computed for 16 particle sizes. They are discretized at 12 optical depths. The last four optical depths are not included for the 3.75- $\mu\text{m}$  channel since the reflectance is essentially invariant for larger optical depths. The arrays for each particle size require 0.25, 0.25, and 0.19 megabytes of storage, respectively, for the 0.65-, 1.60-, and 3.75- $\mu\text{m}$  channels. The emittance models for each particle size have been computed for 3.75, 11, and 12  $\mu\text{m}$ . A total of 75 coefficients is used for each emittance model.

**4.3.5.1.2. Subsystem output.** The output comprises a set of 16-bit integer values that define the cloud properties for each pixel in the analysis block. The parameters are phase (dimensionless), particle size (units of  $\mu\text{m} \times 10$ ), cloud visible optical depth (dimensionless  $\times 10$ ), channel-4 zenith emittance (dimensionless  $\times 100$ ), cloud liquid or ice water path ( $\text{kg}/\text{m}^2 \times 1000$ ), cloud-top pressure (hPa), cloud effective pressure or  $p(T_{\text{cld}})$  (hPa), cloud-base pressure (hPa), cloud effective temperature ( $\text{K} \times 10$ ), cloud effective altitude ( $\text{km} \times 10$ ), and cloud effective cloud particle size ( $\mu\text{m} \times 10$ ). In addition, there will be a quality flag and methodology flag to indicate the uncertainty and source of the retrieval for each pixel.

**4.3.5.1.3. Data processing requirements.** The processing requirements for the reflectance method are given by King and Tsay (1993). The processing needs for the other algorithms are substantial and will be determined.

#### **4.3.5.2. Strategic Concerns**

There are many situations that can prevent or diminish the accuracy of a given parameter retrieval. Some situations can be handled through the application of alternative methods, others by using default options. Solutions to all of the problems noted below, as well as others that will inevitably arise in the development of this global methodology, will be examined in current and future research.

**4.3.5.2.1. Potential problems.** There are many situations that can foil the algorithms outlined above. A listing of all such conditions would be superfluous. Some of the more important potential problems confronting the COPRS are noted below.

In most daytime cases, a reliable retrieval of cloud optical depth, particle size, and temperature can be obtained for optically thick clouds. However, thick low or midlevel clouds can be shadowed by nearby high clouds voiding the plane-parallel assumption in all retrievals using solar reflectance. Shadows also can affect thin-cloud retrievals in variable thickness, single-layer fields (Minnis et al. 1990). Clouds affected by shadows frequently are darker than the clear-sky pixels so that their properties cannot be obtained with reflectance models. Even when optically thick, ice clouds may not produce reflectances that conform to the model configurations because of the wide variety and potential orientations of the particles in cirrus clouds. Particle size retrievals for clouds containing very large particles will be constrained because of the limited sensitivity of the mixed and emittance methods.

Thin-cloud properties will be severely diminished in accuracy for pixels taken over relatively bright backgrounds such as desert, snow, or other clouds. It may not be possible to obtain a solution in many of these instances. Thin-cloud retrievals near coastlines will also be subject to errors in the clear-sky radiances because of slight mislocations. All of the retrievals are based on plane-parallel radiative transfer models. Thus, for scattered or broken cloud fields or for clouds with internal variations in their optical properties, there may be significant errors in the retrieval of particle size and optical depth (e.g., Stackhouse and Stephens 1994; Duda et al. 1994). Cloud thickness estimates are based on a limited amount of empirical data so that the global applicability of these formulas is highly uncertain. As discussed earlier, nocturnal retrievals of  $\tau$  and  $r_e$  are not possible for optically thick clouds. During both day and night, retrievals for overlapped clouds will be much less certain than those for single layer clouds. Near the terminator, the geometry and the atmospheric path lengths diminish the variability in the reflected radiance fields and, essentially, negate the plane-parallel cloud assumption. Retrievals that depend on reflectances become much more uncertain. There is still some solar contamination of the channel-3 radiances at the high solar zenith angles so that an emittance-based retrieval must account for the solar reflectance component which is highly uncertain.

**4.3.5.2.2. Solutions.** Accounting for these various situations presents a challenge to the development of a comprehensive global analysis system. A first-order solution to the problem of shadowed cloud pixels is to tag them as such and assign them the mean values of the nearest cloud layer. If the shadowing is

particularly heavy, it can be assumed that the reflected portion of the channel-3 radiance is negligible. In that case, the 3-channel SIST can be implemented. At this time, there is no technique available for finding ice particle shape and orientation using passive satellite measurements. If no solution can be obtained for a single-layer cloud during the daytime using the 4-channel technique because the particles are too large, the reflectance method using the 1.60- $\mu\text{m}$  channel will be applied. If no solution is obtained, the pixel particle size will be assigned using either the closest extreme model value or the average of all the adjacent pixels. A similar approach is used for optical depth and cloud temperature.

For thin clouds over bright scenes, it may be necessary to use the SIST since the channel-3 surface albedo is relatively small compared to the visible albedo. Similarly, clouds are much more reflective at visible rather than near-infrared wavelengths. In the bright background instances, the channel-3 solar component will be calculated for each of the models and optical depths. The SIST would proceed as usual. This daytime application of the 3-channel emittance method can also be used to determine the consistency between the day and night cloud property retrievals. The use of the 3-channel emittance technique during the day needs further evaluation.

The difficulties of the near-terminator geometry are less manageable than many of the other problems. It may be possible to assume a particle size and derive the cloud temperature and optical depth using channels 4 and 5. When MODIS is operating, the problem is somewhat mitigated because three thermal window channels will be available. At night, when the optical depth and radius retrievals are limited to  $\tau \sim 10$ , a default value will be assigned.

#### **4.3.5.3. Calibration and Validation**

The derived parameters for each pixel are critically dependent on the absolute calibration of the sensors. Although comprehensive sensitivity studies have not been performed for all of the COPRS algorithm components, some estimates of the dependence of particle size on the channel-3 radiance have been made by Han (1992). For example, he found that a precision of  $0.0017 \text{ W}\cdot\text{m}^{-2}\cdot\text{sr}^{-1}$  in the channel 3 radiances translates into uncertainties as low as 2% for  $r_e < 20 \mu\text{m}$ ,  $\tau > 3$  and as great as 10% in  $r_e$  for  $\tau \leq 1$ . Similar uncertainties in the channel 3 calibration would probably produce particle size errors of the same magnitude. The filter functions of the channel-3 sensor must also be accurately known to derive an accurate value of the spectral solar constant for the calculation of the solar component of the observed radiances. Further sensitivity studies are needed to evaluate the full impact of calibration on the derived quantities.

Validation efforts before, during, and after the CERES flights are essential to understanding the accuracy of the retrieved quantities. Before the initial launches, datasets taken during FIRE, ASTEX, ARM, and TOGA/COARE will be used to verify the optical depths, particle phases and sizes, water path, and cloud temperatures using the developmental code and substitute satellite (i.e., historical AVHRR and GOES) and aircraft data. After launch, FIRE III, SHEBA, and ARM data will be used to assess the operational algorithms. in-situ measurements and active remote sensing of cloud microphysics are needed to estimate the uncertainties in phase and particle size. During TRMM, the VIRS-derived droplet radii over water may also be compared for consistency to  $r_e$  retrieved with the microwave liquid-water-path/visible reflectance approach discussed in section 4.3.2.3. Radar and lidar data from aircraft and surface sites are needed to evaluate the particle sizes, cloud-top and cloud-base temperatures, and the ice water paths. Sunphotometers, radar, and lidar data are needed to verify optical depths. Microwave radiometers are needed to assess liquid water path. Other instruments, such as nephelometers, are needed to ensure that the scattering phase functions used in the model calculations are reasonably accurate. All of these types of instruments should be available in part or in total during each of the noted experiments. High-altitude radiometric measurements using wavelengths similar to VIRS or MODIS are needed for calibration checks and for model validation. The ER-2 MODIS Airborne Simulator and the Multispectral Pushbroom Imaging Radiometer (MPIR) proposed for unmanned

aircraft by the DOE should be valuable assets for those purposes. Those data will also be useful for determining the sensitivity of the retrievals to the viewing conditions.

#### 4.3.5.4. *Quality Control and Diagnostics*

The initial quality control occurs within the basic algorithms. Constraints are also applied to ensure that no physically unreasonable values are passed to the next subsystem. Particle sizes are not allowed to fall outside of prespecified limits that depend on phase. Cloud temperatures are not allowed to exceed the warmest temperature in the sounding or at the surface, whichever is greatest. Cloud temperatures must be warmer than the tropopause temperature minus 5 K. As a consistency check, the cloud temperatures will also be compared to the values derived for the layer clouds. Liquid water path and optical depths will be capped to prevent unrealistic values. In all cases, a new value, from adjacent pixels or the nearest cloud layer or from a default value set, will replace the suspect pixel value. A quality flag will be set to indicate what bound was violated. A flag will also be set to denote which methodology or replacement technique produced the final cloud property values. Other diagnostics and quality checks will be implemented as needed.

#### 4.3.5.5. *Numerical Computation Considerations*

The code as currently developed processes up to 275 pixels per second on a 300 *Mflop* CPU. While the speed is less than real time, the operational algorithms will perform at higher rates as a result of code optimization.

### 4.3.6. References

- Ackerman, Steven A.; and Stephens, Graeme L. 1987: The Absorption of Solar Radiation by Cloud Droplets—An Application of Anomalous Diffraction Theory. *J. Atmos. Sci.*, vol. 44, pp. 1574–1588.
- Ackerman, Steven A.; Smith, W. L.; Revercomb, H. E.; and Spinhirne, J. D. 1990: The 27–28 October 1986 FIRE IFO Cirrus Case Study—Spectral Properties of Cirrus Clouds in the 8–12 Micron Window. *Mon. Weather Rev.*, vol. 118, pp. 2377–2388.
- Arking, A.; and Childs, J. D. 1985: Retrieval of Cloud Cover Parameters From Multispectral Satellite Images. *J. Climat. & Appl. Meteorol.*, vol. 24, pp. 322–333.
- Baum, Bryan A.; Arduini, Robert F.; Wielicki, Bruce A.; Minnis, Patrick; and Si-Chee, Tsay 1994: Multilevel Cloud Retrieval Using Multispectral HIRS and AVHRR Data: Nighttime Oceanic Analysis. *J. Geophys. Res.*, vol. 99, no. D3, pp. 5499–5514.
- Baum, Bryan A.; Wielicki, Bruce A.; Minnis, Patrick; and Parker, Lindsay 1992: Cloud-Property Retrieval Using Merged HIRS and AVHRR Data. *J. Appl. Meteorol.*, vol. 31, pp. 351–369.
- Blau, H. H., Jr.; Espinola, R. P.; and Reifenshtein, E. C., III 1966: Near Infrared Scattering by Sunlit Terrestrial Clouds. *Appl. Opt.*, vol. 5, pp. 555–564.
- Charlson, Robert J.; Warren, Stephen G.; Lovelock, James E.; and Andreae, Meinrat O. 1987: Oceanic Phytoplankton, Atmospheric Sulphur, Cloud Albedo and Climate. *Nature*, vol. 326, pp. 655–661.
- Coakley, James A., Jr.; Bernstein, Robert L.; and Durkee, Philip A. 1987: Effect of Ship-Stack Effluents on Cloud Reflectivity. *Science*, vol. 237, pp. 1020–1022.
- Curran, R. J.; and Wu, M.-L. C. 1982: Skylab Near-Infrared Observations of Clouds Indicating Supercooled Liquid Water Droplets. *J. Atmos. Sci.*, vol. 39, pp. 635–647.
- d'Entremont, Robert P. 1986: Low- and Mid-Level Cloud Analysis Using Nighttime Multispectral Imagery. *J. Climat. & Appl. Meteorol.*, vol. 25, pp. 1853–1869.
- Duda, D. P.; Stephens, G. L.; and Cotton, W. R. 1994: Impact of Enhanced CCN Concentrations on the Radiative Properties of a 3D Marine Stratocumulus Cloud. *Eighth Conference on Atmospheric Radiation*, AMS, pp. 262–264.

- Fu, Qiang; and Liou, K. N. 1992: On the Correlated  $k$ -Distribution Method for Radiative Transfer in Nonhomogeneous Atmospheres. *J. Atmos. Sci.* vol. 49, no. 22, pp. 2139–2156.
- Hale, G. M.; and Query, M. R. 1973: Optical Constants of Water in the 200-nm to 200-Micron Wavelength Region. *Appl. Opt.*, vol. 12, pp. 555–563.
- Han, Q. 1992: Global Survey of Effective Particle Size in Liquid Water Clouds. Ph.D. Diss., Columbia University, New York.
- Hansen, J. E.; and Travis, L. D. 1974: Light Scattering in Planetary Atmospheres. *Space Sci. Rev.*, vol. 16, pp. 527–610.
- Hansen, J. E.; and Pollack, J. B. 1970: Near-Infrared Light Scattering by Terrestrial Clouds. *J. Atmos. Sci.*, vol. 27, pp. 265–281.
- Heymsfield, A. J.; and Platt, C. M. R. 1984: A Parameterization of the Particle Size Spectrum of Ice Clouds in Terms of the Ambient Temperature and the Ice Water Content. *J. Atmos. Sci.*, vol. 41, pp. 846–855.
- Hunt, G. E. 1973: Radiative Properties of Terrestrial Clouds at Visible and Infra-Red Thermal Window Wavelengths. *Q. J. R. Meteorol. Soc.*, vol. 99, pp. 346–369.
- Inoue, T. 1985: On the Temperature and Effective Emissivity Determination of Semi-Transparent Cirrus Clouds by Bi-Spectral Measurements in the 10 Micron Window Region. *Meteorol. Soc. Japan*, vol. 63, pp. 88–99.
- King, Michael D.; Kaufman, Yoram J.; Menzel, W. Paul; and Tanre, Didier D. 1992: Remote Sensing of Cloud, Aerosol, and Water Vapor Properties From the Moderate Resolution Imaging Spectrometer (MODIS). *IEEE Trans. Geosci. & Remote Sens.*, vol. 30, pp. 2–27.
- King, M. D.; and Tsay, S. C. 1993: Theoretical Basis of Cloud Retrieval Algorithms for MODIS: Cloud Cover, Thermodynamic Phase, Optical Thickness and Effective Particle Radius. *MODIS Algorithm Theoretical Basis Document*, p. 32.
- Kratz, D. P. 1995: The Correlated  $k$ -Distribution Technique as Applied to the AVHRR Channels. *J. Quant. Spectrosc. Radiat. Transfer*, vol. 53, pp. 501–507.
- Lin, Xijian; and Coakley, James A., Jr. 1993: Retrieval of Properties for Semitransparent Clouds From Multispectral Infrared Imagery Data. *J. Geophys. Res.*, vol. 98, no. 10, pp. 18,501–18,514.
- Liou, K. 1974: On the Radiative Properties of Cirrus in the Window Region and Their Influence on Remote Sensing of the Atmosphere. *J. Atmos. Sci.*, vol. 31, pp. 522–532.
- Liou, K. N.; Ou, S. C.; Takano, Y.; Valero, F. P. J.; and Ackerman, T. P. 1990a: Remote Sounding of the Tropical Cirrus Cloud Temperature and Optical Depth Using 6.5 and 10.5-Micron Radiometers During STEP. *J. Appl. Meteorol.*, vol. 29, pp. 716–726.
- Liou, K. N.; Takano, Y.; Ou, S. C.; Heymsfield, A.; and Kreiss, W. 1990b: Infrared Transmission through Cirrus Clouds—A Radiative Model for Target Detection. *Appl. Opt.*, vol. 29, pp. 1886–1896.
- Macke, A.; Mueller, J.; and Raschke, E. 1996: Single Scattering Properties of Atmospheric Ice Crystals. *J. Atmos. Sci.* vol. 53, pp. 2813–2825.
- Masuda, Kazuhiko; and Takashima, Tsutomu 1990: Deriving Cirrus Information Using the Visible and Near-IR Channels of the Future NOAA-AVHRR Radiometer. *Remote Sens. Environ.*, vol. 31, pp. 65–81.
- Minnis, P.; Garber, D. P.; Young, D. F.; Arduini, R. F.; and Takano, Y. 1997: Parameterizations of Reflectance and Emittance for Satellite Remote Sensing of Cloud Properties. Submitted to *J. Atmos. Sci.*
- Minnis, Patrick; Heck, Patrick W.; and Young, David F. 1993a: Inference of Cirrus Cloud Properties Using Satellite-Observed Visible and Infrared Radiances. II—Verification of Theoretical Cirrus Radiative Properties, *J. Atmos. Sci.*, vol. 50, no. 9, pp. 1305–1322.
- Minnis, Patrick; Heck, Patrick W.; Young, David F.; Fairall, C. W.; and Snider, J. B. 1992: Stratocumulus Cloud Properties Derived From Simultaneous Satellite and Island-Based Instrumentation During FIRE. *J. Appl. Meteorol.*, vol. 31, pp. 317–339.
- Minnis, Patrick; Kratz, David P.; Coakley, James A., Jr.; King, Michael D.; Garber, Donald; Heck, Patrick; Mayor, Shalini; Smith, W. L., Jr.; Young, David F.; and Arduini, Robert 1995: Cloud Optical Property Retrieval. Clouds and the Earth's Radiant Energy System (CERES) Algorithm Theoretical Basic Document, Volume III--Cloud Analyses and Determination of Improved Top of Atmosphere Fluxes, NASA RP-1376, pp. 135-176.
- Minnis, Patrick; Liou, Kuo-Nan; and Takano, Yoshihide 1993b: Inference of Cirrus Cloud Properties Using Satellite-Observed Visible and Infrared Radiances. I—Parameterization of Radiance Fields. *J. Atmos. Sci.*, vol. 50, no. 9, pp. 1279–1304.

- Minnis, Patrick; Young, David F.; Sassen, Kenneth; Alvarez, Joseph M.; and Grund, Christian J. 1990: The 27–28 October 1986 FIRE IFO Cirrus Case Study—Cirrus Parameter Relationships Derived from Satellite and Lidar Data. *Mon. Weather Rev.*, vol. 118, pp. 2402–2425.
- Minnis, P.; Young, D. F.; Garber, D. P.; Takano, Y.; and Liou, K. N. 1994: Effects of Cloud Particle Size and Shape on Satellite Remote Sensing of Cloud Properties. *Eighth Conference on Atmospheric Radiation*, AMS, pp. 418–420.
- Nakajima, Teruyuki; and King, Michael D. 1990: Determination of the Optical Thickness and Effective Particle Radius of Clouds From Reflected Solar Radiation Measurements. I—Theory. *J. Atmos. Sci.*, vol. 47, pp. 1878–1893.
- Nakajima, Teruyuki; King, Michael D.; Spinhirne, James D.; and Radke, Lawrence F. 1991: Determination of the Optical Thickness and Effective Particle Radius of Clouds From Reflected Solar Radiation Measurements. II—Marine Stratocumulus Observations. *J. Atmos. Sci.*, vol. 48, pp. 728–750.
- Ou, S. C.; Liou, K. N.; Gooch, W. M.; and Takano, Y. 1993: Remote Sensing of Cirrus Cloud Parameters Using Advanced Very-High-Resolution Radiometer 3.7- and 10.9- $\mu\text{m}$  Channels. *Appl. Opt.*, vol. 32, no. 12, pp. 2171–2180.
- Parol, F.; Buriez, J. C.; Brogniez, G.; and Fouquart, Y. 1991: Information Content of AVHRR Channels 4 and 5 With Respect to the Effective Radius of Cirrus Cloud Particles. *J. Appl. Meteorol.*, vol. 30, pp. 973–984.
- Platnick, S.; and Twomey, S. 1994: Determining the Susceptibility of Cloud Albedo to Changes in Droplet Concentration with the Advanced Very High resolution Radiometer. *J. Appl. Meteorol.* vol. 33, pp. 334–346.
- Platnick, S.; and Valero, F. P. J. 1995: A Validation of Cloud Retrieval during ASTEX. *J. Atmos. Sci.*, vol. 52, pp. 2985–3001.
- Prabhakara, C.; Fraser, R. S.; Dalu, G.; Wu, Man-Li C.; and Curran, R. J. 1988: Thin Cirrus Clouds—Seasonal Distribution Over Oceans Deduced From Nimbus-4 IRIS. *J. Appl. Meteorol.*, vol. 27, pp. 379–399.
- Radke, Lawrence F.; Coakley, James A., Jr.; and King, Michael D. 1989: Direct and Remote Sensing Observations of the Effects of Ships on Clouds. *Science*, vol. 246, pp. 1146–1149.
- Rawlins, F.; and Foot J. S. 1990: Remotely Sensed Measurements of Stratocumulus Properties During FIRE Using the C130 Aircraft Multi-Channel Radiometer. *J. Atmos. Sci.*, vol. 47, pp. 2488–2503.
- Reynolds, D. W.; and Vonder Haar, T. H. 1977: A Bispectral Method for Cloud Parameter Determination. *Mon. Weather Rev.*, vol. 105, pp. 446–457.
- Rossow, William B.; and Lacis, Andrew A. 1990: Global, Seasonal Cloud Variation From Satellite Radiance Measurements. II—Cloud Properties and Radiative Effects. *J. Climat.*, vol. 3, pp. 1204–1253.
- Rossow, William B.; Garder, Leonid, C.; Lu, Pei-Jane; and Walker, Alison 1992: *International Satellite Cloud Climatology Project (ISCCP): Documentation of Cloud Data*. Centel Federal Services Corp., New York.
- Rossow, W. B.; Mosher, F.; Kinsella, E.; Arking, A.; and Harrison, E. 1985: ISCCP Cloud Algorithm Intercomparison. *J. Climat. & Appl. Meteorol.*, vol. 24, Sept. 1985, pp. 877–903.
- Slingo, A. 1989: A GCM Parameterization for the Shortwave Radiative Properties of Water Clouds. *J. Atmos. Sci.*, vol. 46, pp. 1419–1427.
- Smith, William L., Jr.; Minnis, Patrick; Alvarez, Joseph M.; Uttal, Taneil; Intrieri, Janet M.; Ackerman, Thomas P; and Clothiaux, Eugene 1993: Development of Methods for Inferring Cloud Thickness and Cloud Thickness and Cloud-Base Height From Satellite Radiance Data. *The FIRE Cirrus Science Results 1993*, David S. McDougal, ed., NASA CP-3238, pp. 32–35.
- Stackhouse, Paul W., Jr.; and Stephens, Graeme L. 1994: Investigation of the Effects of the Macrophysical and Microphysical Properties of Cirrus Clouds on the Retrieval of Optical Properties—Results for FIRE 2. *The FIRE Cirrus Science Results 1993*, David S. McDougal, ed., NASA CP-3238, pp. 189–192.
- Stephens, G. L. 1978: Radiation Profiles in Extended Water Clouds. Part I—Theory. Part II: Parameterization Schemes. *J. Atmos. Sci.*, vol. 35, pp. 2111–2132.
- Stone, Robert S.; Stephens, Graeme, L.; Platt, C. M. R.; and Banks, S. 1990: The Remote Sensing of Thin Cirrus Cloud Using Satellites, Lidar and Radiative Transfer Theory. *J. Appl. Meteorol.*, vol. 29, pp. 353–366.
- Takano, Yoshihide; and Liou, Kuo-Nan 1989: Solar Radiative Transfer in Cirrus Clouds. I—Single-Scattering and Optical Properties of Hexagonal Ice Crystals. *J. Atmos. Sci.*, vol. 46, pp. 3–36.
- Takano, Y.; Liou, K. N.; and Minnis, P. 1992: The Effects of Small Ice Crystals on Cirrus Infrared Radiative Properties. *J. Atmos. Sci.*, vol. 49, no. 16, pp. 1487–1493.

- Twomey, S. 1977: The Influence of Pollution on the Shortwave Albedo of Clouds. *J. Atmos. Sci.*, vol. 34, pp. 1149–1152.
- Twomey, S.; and Cocks, T. 1982: Spectral Reflectance of Clouds in the Near-Infrared—Comparison of Measurements and Calculations. *J. Meteorol. Soc. Japan*, vol. 60, pp. 583–592.
- Twomey, S.; and Cocks, T. 1989: Remote Sensing of Cloud Parameters From Spectral Reflectance in the Near-Infrared. *Beitr. Phys. Atmos.*, vol. 62, no. 3, pp. 172–179.
- Twomey, S.; and Seton, K. J. 1980: Inferences of Gross Microphysical Properties of Clouds From Spectral Reflectance Measurements. *J. Atmos. Sci.*, vol. 37, pp. 1065–1069.
- Van De Hulst, Hendrik Christoffel 1957: *Light Scattering by Small Particles*. John Wiley & Sons, 1957.
- Wielicki, Bruce A.; Suttles, J. T.; Heymsfield, Andrew J.; Welch, Ronald M.; Spinhirne, James D.; Wu, Man-Li C.; and Starr, David O'C. 1990: The 27-28 October 1986 FIRE IFO Cirrus Case Study—Comparison of Radiative Transfer Theory With Observations by Satellite and Aircraft. *Mon. Weather Rev.*, vol. 118, pp. 2356–2376.
- Wigley T. M. L. 1989: Possible Climate Change Due to SO<sub>2</sub>-Derived Cloud Condensation Nuclei. *Nature*, vol. 339, pp. 365–367.
- Wu, Man-Li C. 1987: A Method for Remote Sensing the Emissivity, Fractional Cloud Cover and Cloud Top Temperature of High-Level, Thin Clouds. *J. Climat. & Appl. Meteorol.*, vol. 26, pp. 225–233.
- Young, D. F.; Mayor, S.; Minnis, P.; Intrieri, J. M.; Matrosov, S.; and Snider, J. 1994: Comparison of Satellite and Surface-Based Remote Sensing of Cloud Microphysical Properties During FIRE Cirrus Phase II. *Eighth Conference on Atmospheric Radiation*, AMS, pp. 231–233.
- Young, D. F.; Minnis, P.; Katsaros, K.; Dybbroe, A.; and Mileta, J. 1992: Comparison of Techniques for Deriving Water-Cloud Microphysical Properties From Multiple Satellite Data. *Proceedings of the 11th International Conference Clouds and Precipitation*, pp. 1053–1056.
- Young, D. F.; Minnis, P.; Snider, J. B.; Uttal, T.; Intrieri, J. M.; and Matrosov, S. 1993: Comparison of Cloud Microphysical Parameters Derived From Surface and Satellite Measurements During FIRE Phase II. *Proceedings of the FIRE Cirrus Science Conference*, pp. 52–55.

## Appendix A

### Correction for Gaseous Absorption

Numerous cloud property retrieval techniques require knowledge of the absorption properties of the atmosphere as an integral part of the analysis. Complementary analysis of satellite data with radiative transfer theory improves not only our ability to analyze and understand the data, but our understanding of the physics of the processes modeled. To this end, the absorption by molecular species in the clear-sky pixels is accomplished by means of the correlated  $k$ -distribution technique.

#### *Correlated $k$ -Distribution Technique*

Various modeling techniques are available to account for the observed absorption of electromagnetic radiation by the molecules which are present in planetary atmospheres. The line-by-line, or monochromatic, procedure is very precise and has an accuracy that is limited only by the extent of our knowledge of the interactions of matter with energy. Such precision, however, is only obtained at the cost of very intensive routines which are not practical in production calculations. To overcome the computational burden of the line-by-line procedure, narrowband and broadband techniques have been devised. While these band models can be made arbitrarily accurate for a homogeneous (constant temperature, pressure, etc.) atmosphere, they require a scaling procedure to account for the inhomogeneity found in realistic atmospheres. In essence, the scaling procedure transforms the inhomogeneous pathlength found in a realistic atmosphere into an equivalent homogeneous pathlength. While entirely satisfactory for the case where only absorption is present, such a transformation is not acceptable for cases where scattering is involved. Nevertheless, a technique, known as the correlated  $k$ -distribution, has been devised to accurately and efficiently calculate molecular absorption for a inhomogeneous path without a scaling approximation.

Taking for a moment any arbitrary spectral interval, if the absorption coefficient ( $k$ ) is plotted against wavenumber  $\omega$ , a highly nonmonotonic plot will be obtained. The line-by-line procedure resorts to retracing this plot with sufficient spectral resolution so as to accurately reproduce the spectrum of absorption coefficients. An examination of this plot of  $k$  versus  $\omega$  will reveal that similar values of  $k$  occur many times. Thus arises the concept of the  $k$  distribution. If a transformation of coordinates is made from wavenumber space to cumulative probability space  $g(k)$ , it will be observed that the highly nonmonotonic plot of  $k$  versus  $\omega$  will become a monotonic plot of  $k$  versus  $g(k)$ . To this point, the only information which has been discarded is the precise spectral location of a particular  $k$ ; however, no gain in speed has been obtained. Recall that only the terms of the integration have been reordered. It is noted, however, that the monotonic distribution of  $k$  versus  $g(k)$  can have far fewer (often 3 to 5 orders of magnitude) terms, yet retain very high accuracy for the calculation of the absorption for the specified spectral interval. This reduction in the number  $k$  values needed leads to the increased efficiency necessary for any production calculations. To account for a inhomogeneous path, an additional assumption is required. Given any pressure or temperature encountered in the atmosphere, it is assumed that any particular absorption coefficient will always have the same cumulative probability. Thus, the location in cumulative probability space of any absorption coefficient at any given pressure or temperature will be correlated with that of the absorption coefficient at a specified reference pressure and temperature. This leads to the concept of the correlated  $k$ -distribution. Fu and Liou (1992) have demonstrated conclusively that the assumption of correlation is sufficiently accurate for most purposes. Since the  $k$ 's are assumed to be correlated for any pressure and temperature, the correlated  $k$ -distribution procedure can be calculated through an inhomogeneous atmosphere in the same manner as a monochromatic calculation. Thus, the correlated  $k$ -distribution allows for an efficient and accurate calculation which is compatible with most scattering routines.

**Appendix B****Nomenclature****Acronyms**

ADEOS	Advanced Earth Observing System
ADM	Angular Distribution Model
AIRS	Atmospheric Infrared Sounder (EOS-AM)
AMSU	Advanced Microwave Sounding Unit (EOS-PM)
APD	Aerosol Profile Data
APID	Application Identifier
ARESE	ARM Enhanced Shortwave Experiment
ARM	Atmospheric Radiation Measurement
ASOS	Automated Surface Observing Sites
ASTER	Advanced Spaceborne Thermal Emission and Reflection Radiometer
ASTEX	Atlantic Stratocumulus Transition Experiment
ASTR	Atmospheric Structures
ATBD	Algorithm Theoretical Basis Document
AVG	Monthly Regional, Average Radiative Fluxes and Clouds (CERES Archival Data Product)
AVHRR	Advanced Very High Resolution Radiometer
BDS	Bidirectional Scan (CERES Archival Data Product)
BRIE	Best Regional Integral Estimate
BSRN	Baseline Surface Radiation Network
BTD	Brightness Temperature Difference(s)
CCD	Charge Coupled Device
CCSDS	Consultative Committee for Space Data Systems
CEPEX	Central Equatorial Pacific Experiment
CERES	Clouds and the Earth's Radiant Energy System
CID	Cloud Imager Data
CLAVR	Clouds from AVHRR
CLS	Constrained Least Squares
COPRS	Cloud Optical Property Retrieval System
CPR	Cloud Profiling Radar
CRH	Clear Reflectance, Temperature History (CERES Archival Data Product)
CRS	Single Satellite CERES Footprint, Radiative Fluxes and Clouds (CERES Archival Data Product)
DAAC	Distributed Active Archive Center
DAC	Digital-Analog Converter
DAO	Data Assimilation Office

DB	Database
DFD	Data Flow Diagram
DLF	Downward Longwave Flux
DMSP	Defense Meteorological Satellite Program
EADM	ERBE-Like Albedo Directional Model (CERES Input Data Product)
ECA	Earth Central Angle
ECLIPS	Experimental Cloud Lidar Pilot Study
ECMWF	European Centre for Medium-Range Weather Forecasts
EDDB	ERBE-Like Daily Data Base (CERES Archival Data Product)
EID9	ERBE-Like Internal Data Product 9 (CERES Internal Data Product)
EOS	Earth Observing System
EOSDIS	Earth Observing System Data Information System
EOS-AM	EOS Morning Crossing Mission
EOS-PM	EOS Afternoon Crossing Mission
ENSO	El Niño/Southern Oscillation
ENVISAT	Environmental Satellite
EPHANC	Ephemeris and Ancillary (CERES Input Data Product)
ERB	Earth Radiation Budget
ERBE	Earth Radiation Budget Experiment
ERBS	Earth Radiation Budget Satellite
ESA	European Space Agency
ES4	ERBE-Like S4 Data Product (CERES Archival Data Product)
ES4G	ERBE-Like S4G Data Product (CERES Archival Data Product)
ES8	ERBE-Like S8 Data Product (CERES Archival Data Product)
ES9	ERBE-Like S9 Data Product (CERES Archival Data Product)
FLOP	Floating Point Operation
FIRE	First ISCCP Regional Experiment
FIRE II IFO	First ISCCP Regional Experiment II Intensive Field Observations
FOV	Field of View
FSW	Hourly Gridded Single Satellite Fluxes and Clouds (CERES Archival Data Product)
FTM	Functional Test Model
GAC	Global Area Coverage (AVHRR data mode)
GAP	Gridded Atmospheric Product (CERES Input Data Product)
GCIP	GEWEX Continental-Phase International Project
GCM	General Circulation Model
GEBA	Global Energy Balance Archive
GEO	ISCCP Radiances (CERES Input Data Product)
GEWEX	Global Energy and Water Cycle Experiment
GLAS	Geoscience Laser Altimetry System

GMS	Geostationary Meteorological Satellite
GOES	Geostationary Operational Environmental Satellite
HBTM	Hybrid Bispectral Threshold Method
HIRS	High-Resolution Infrared Radiation Sounder
HIS	High-Resolution Interferometer Sounder
ICM	Internal Calibration Module
ICRCCM	Intercomparison of Radiation Codes in Climate Models
ID	Identification
IEEE	Institute of Electrical and Electronics Engineers
IES	Instrument Earth Scans (CERES Internal Data Product)
IFO	Intensive Field Observation
INSAT	Indian Satellite
IOP	Intensive Observing Period
IR	Infrared
IRIS	Infrared Interferometer Spectrometer
ISCCP	International Satellite Cloud Climatology Project
ISS	Integrated Sounding System
IWP	Ice Water Path
LAC	Local Area Coverage (AVHRR data mode)
LaRC	Langley Research Center
LBC	Laser Beam Ceilometer
LBTM	Layer Bispectral Threshold Method
Lidar	Light Detection and Ranging
LITE	Lidar In-Space Technology Experiment
Lowtran 7	Low-Resolution Transmittance (Radiative Transfer Code)
LW	Longwave
LWP	Liquid Water Path
MAM	Mirror Attenuator Mosaic
MC	Mostly Cloudy
MCR	Microwave Cloud Radiometer
METEOSAT	Meteorological Operational Satellite (European)
METSAT	Meteorological Satellite
MFLOP	Million FLOP
MIMR	Multifrequency Imaging Microwave Radiometer
MISR	Multiangle Imaging Spectroradiometer
MLE	Maximum Likelihood Estimate
MOA	Meteorology Ozone and Aerosol
MODIS	Moderate-Resolution Imaging Spectroradiometer
MSMR	Multispectral, multiresolution

MTSA	Monthly Time and Space Averaging
MWH	Microwave Humidity
MWP	Microwave Water Path
NASA	National Aeronautics and Space Administration
NCAR	National Center for Atmospheric Research
NCEP	National Centers for Environmental Prediction
NESDIS	National Environmental Satellite, Data, and Information Service
NIR	Near Infrared
NMC	National Meteorological Center
NOAA	National Oceanic and Atmospheric Administration
NWP	Numerical Weather Prediction
OLR	Outgoing Longwave Radiation
OPD	Ozone Profile Data (CERES Input Data Product)
OV	Overcast
PC	Partly Cloudy
POLDER	Polarization of Directionality of Earth's Reflectances
PRT	Platinum Resistance Thermometer
PSF	Point Spread Function
PW	Precipitable Water
RAPS	Rotating Azimuth Plane Scan
RPM	Radiance Pairs Method
RTM	Radiometer Test Model
SAB	Sorting by Angular Bins
SAGE	Stratospheric Aerosol and Gas Experiment
SARB	Surface and Atmospheric Radiation Budget Working Group
SDCD	Solar Distance Correction and Declination
SFC	Hourly Gridded Single Satellite TOA and Surface Fluxes (CERES Archival Data Product)
SHEBA	Surface Heat Budget in the Arctic
SPECTRE	Spectral Radiance Experiment
SRB	Surface Radiation Budget
SRBAVG	Surface Radiation Budget Average (CERES Archival Data Product)
SSF	Single Satellite CERES Footprint TOA and Surface Fluxes, Clouds
SSMI	Special Sensor Microwave Imager
SST	Sea Surface Temperature
SURFMAP	Surface Properties and Maps (CERES Input Product)
SW	Shortwave
SWICS	Shortwave Internal Calibration Source
SYN	Synoptic Radiative Fluxes and Clouds (CERES Archival Data Product)

SZA	Solar Zenith Angle
THIR	Temperature/Humidity Infrared Radiometer (Nimbus)
TIROS	Television Infrared Observation Satellite
TISA	Time Interpolation and Spatial Averaging Working Group
TMI	TRMM Microwave Imager
TOA	Top of the Atmosphere
TOGA	Tropical Ocean Global Atmosphere
TOMS	Total Ozone Mapping Spectrometer
TOVS	TIROS Operational Vertical Sounder
TRMM	Tropical Rainfall Measuring Mission
TSA	Time-Space Averaging
UAV	Unmanned Aerospace Vehicle
UT	Universal Time
UTC	Universal Time Code
VAS	VISSR Atmospheric Sounder (GOES)
VIRS	Visible Infrared Scanner
VISSR	Visible and Infrared Spin Scan Radiometer
WCRP	World Climate Research Program
WG	Working Group
Win	Window
WN	Window
WMO	World Meteorological Organization
ZAVG	Monthly Zonal and Global Average Radiative Fluxes and Clouds (CERES Archival Data Product)

### **Symbols**

$A$	atmospheric absorptance
$B_{\lambda}(T)$	Planck function
$C$	cloud fractional area coverage
$CF_2Cl_2$	dichlorofluorocarbon
$CFCl_3$	trichlorofluorocarbon
$CH_4$	methane
$CO_2$	carbon dioxide
$D$	total number of days in the month
$D_e$	cloud particle equivalent diameter (for ice clouds)
$E_o$	solar constant or solar irradiance
$F$	flux
$f$	fraction
$G_a$	atmospheric greenhouse effect

$g$	cloud asymmetry parameter
$H_2O$	water vapor
$I$	radiance
$i$	scene type
$m_i$	imaginary refractive index
$\hat{N}$	angular momentum vector
$N_2O$	nitrous oxide
$O_3$	ozone
$P$	point spread function
$p$	pressure
$Q_a$	absorption efficiency
$Q_e$	extinction efficiency
$Q_s$	scattering efficiency
$R$	anisotropic reflectance factor
$r_E$	radius of the Earth
$r_e$	effective cloud droplet radius (for water clouds)
$r_h$	column-averaged relative humidity
$S_o$	summed solar incident SW flux
$S'_o$	integrated solar incident SW flux
$T$	temperature
$T_B$	blackbody temperature
$t$	time or transmittance
$W_{liq}$	liquid water path
$w$	precipitable water
$\hat{x}_o$	satellite position at $t_o$
$x, y, z$	satellite position vector components
$\dot{x}, \dot{y}, \dot{z}$	satellite velocity vector components
$z$	altitude
$z_{top}$	altitude at top of atmosphere
$\alpha$	albedo or cone angle
$\beta$	cross-scan angle
$\gamma$	Earth central angle
$\gamma_{at}$	along-track angle
$\gamma_{ct}$	cross-track angle
$\delta$	along-scan angle
$\varepsilon$	emittance
$\Theta$	colatitude of satellite
$\theta$	viewing zenith angle
$\theta_o$	solar zenith angle

$\lambda$	wavelength
$\mu$	viewing zenith angle cosine
$\mu_o$	solar zenith angle cosine
$\nu$	wave number
$\rho$	bidirectional reflectance
$\tau$	optical depth
$\tau_{aer}(p)$	spectral optical depth profiles of aerosols
$\tau_{H_2O\lambda}(p)$	spectral optical depth profiles of water vapor
$\tau_{O_3}(p)$	spectral optical depth profiles of ozone
$\Phi$	longitude of satellite
$\phi$	azimuth angle
$\tilde{\omega}_o$	single-scattering albedo

## Subscripts:

$c$	cloud
$cb$	cloud base
$ce$	cloud effective
$cld$	cloud
$cs$	clear sky
$ct$	cloud top
$ice$	ice water
$lc$	lower cloud
$liq$	liquid water
$s$	surface
$uc$	upper cloud
$\lambda$	spectral wavelength

**Units**

AU	astronomical unit
cm	centimeter
cm-sec <sup>-1</sup>	centimeter per second
count	count
day	day, Julian date
deg	degree
deg-sec <sup>-1</sup>	degree per second
DU	Dobson unit
erg-sec <sup>-1</sup>	erg per second
fraction	fraction (range of 0–1)
g	gram
g-cm <sup>-2</sup>	gram per square centimeter

$g-g^{-1}$	gram per gram
$g-m^{-2}$	gram per square meter
h	hour
hPa	hectopascal
K	Kelvin
kg	kilogram
$kg-m^{-2}$	kilogram per square meter
km	kilometer
$km-sec^{-1}$	kilometer per second
m	meter
mm	millimeter
$\mu m$	micrometer, micron
N/A	not applicable, none, unitless, dimensionless
$ohm-cm^{-1}$	ohm per centimeter
percent	percent (range of 0–100)
rad	radian
$rad-sec^{-1}$	radian per second
sec	second
$sr^{-1}$	per steradian
W	watt
$W-m^{-2}$	watt per square meter
$W-m^{-2}sr^{-1}$	watt per square meter per steradian
$W-m^{-2}sr^{-1}\mu m^{-1}$	watt per square meter per steradian per micrometer